

**UCLA**

**UCLA Electronic Theses and Dissertations**

**Title**

Production of positron emission tomography (PET) radiotracers with electrowetting-on-dielectric (EWOD) digital microfluidics

**Permalink**

<https://escholarship.org/uc/item/1zz6h16w>

**Author**

Chen, Supin

**Publication Date**

2014

Peer reviewed|Thesis/dissertation

UNIVERSITY OF CALIFORNIA

Los Angeles

Production of positron emission tomography (PET) radiotracers with electrowetting-on-dielectric (EWOD) digital microfluidics

A dissertation submitted in partial satisfaction of the  
requirements for the degree Doctor of Philosophy  
in Bioengineering

by

Supin Chen

2014

© Copyright by

Supin Chen

2014

## ABSTRACT OF THE DISSERTATION

Production of positron emission tomography (PET) radiotracers with electrowetting-on-dielectric (EWOD) digital microfluidics

by

Supin Chen

Doctor of Philosophy in Biongeering

University of California, Los Angeles, 2014

Professor Chang-Jin Kim, Chair

There is currently a need to improve production of radiotracers for positron emission tomography (PET) imaging because although thousands of radiotracers have been developed in research settings, only a few are readily available, severely limiting the biological problems that can be studied *in vivo* via PET. An electrowetting-on-dielectric (EWOD) digital microfluidic chip was designed with multifunctional electrodes (for heating, temperature sensing, and EWOD driving) to synthesize a variety of  $^{18}\text{F}$ -labeled tracers targeting a range of biological processes. A single EWOD radiosynthesizer device design was used for complete synthesis of four radiotracers (a sugar, a DNA nucleoside, a protein-labelling compound, and a neurotransmitter). All of the key synthesis steps for radiochemistry have been demonstrated on chip: concentration of fluoride ion, solvent exchange, chemical reaction, and purification. A mirrored configuration of valve metal oxide was also investigated for use as a cost effective and high electrical performance dielectric in EWOD.

The dissertation of Supin Chen is approved.

R. Michael van Dam

Anna M. Wu

Andrea Kasko

Dean Ho

Chang-Jin Kim, Committee Chair

University of California, Los Angeles

2014

# TABLE OF CONTENTS

ABSTRACT OF THE DISSERTATION.....	iv
TABLE OF CONTENTS .....	iv
LIST OF FIGURES .....	viii
LIST OF TABLES .....	xi
ACKNOWLEDGEMENTS.....	xii
VITA .....	xiv
CHAPTER 1: Introduction .....	1
1.1 Production of radiotracers for positron emission tomography (PET) .....	1
1.1.1 Positron emission tomography (PET) and radiotracers .....	1
1.1.2 Need for improved radiotracer availability .....	3
1.1.3 Automated radiosynthesizers .....	4
1.1.4 Microfluidic radiosynthesizers .....	6
1.2 Electrowetting-on-dielectric (EWOD) .....	8
1.3 EWOD for radiotracer production.....	10
1.4 Summary.....	12
CHAPTER 2: EWOD device with integrated heaters for radiochemistry .....	14
2.1 Overview.....	14
2.2 Multifunctional EWOD electrode for radiochemistry.....	16
2.2.1 Self-centering EWOD heaters .....	16
2.2.2 Concentric heater rings .....	19
2.3 Fabrication of radiochemistry EWOD device.....	21
2.4 EWOD control system.....	24
2.5 Movement of liquids and droplet splitting.....	26
2.6 Droplet heating .....	27

2.6.1 Heating on multifunctional electrodes .....	27
2.6.2 Droplet temperature .....	30
2.7 Summary .....	31
CHAPTER 3: Radiolabelling chemistry on EWOD .....	32
3.1 Overview .....	32
3.2 Radiotracers produced by EWOD radiosynthesizer .....	34
3.2.1 [ <sup>18</sup> F]FDG .....	34
3.2.2 [ <sup>18</sup> F]FLT .....	35
3.2.3 [ <sup>18</sup> F]SFB .....	36
3.2.4 [ <sup>18</sup> F]fallypride .....	37
3.3 Radiolabelling chemistry steps on EWOD device .....	38
3.3.1 Reagents, materials, and analytical methods.....	38
3.3.2 Fluoride concentration .....	40
3.3.3 Solvent exchange and azeotropic drying .....	43
3.3.4 Fluorination and other reactions .....	45
3.4 Off chip purification and evaluation.....	46
3.4.1 Extraction .....	46
3.4.2 Purification and analysis .....	47
3.5 Radiotracer synthesis yield .....	49
3.6. Quality control and use of radiotracers.....	52
3.6.1 Quality control and imaging of [ <sup>18</sup> F]FDG.....	52
3.6.2 Quality control and imaging of [ <sup>18</sup> F]FLT .....	56
3.6.3 Quality control and conjugation of [ <sup>18</sup> F]SFB.....	60

3.6.4 Quality control and imaging of [ <sup>18</sup> F]fallypride .....	61
3.7 Summary .....	64
CHAPTER 4: On chip solid-phase extraction for radioisotope removal .....	66
4.1 Overview .....	66
4.2 Conventional radiochemistry purification .....	68
4.3 Microfluidic solid-phase extraction.....	70
4.4 Exposed alumina for on chip removal of fluoride.....	72
4.4.1 Alumina as dielectric and SPE surface .....	72
4.4.2 Fluoride adsorption on alumina cover plate.....	74
4.4.3 Fluoride removal after radiolabelling .....	75
4.5 On chip filtration of SPE particles .....	77
4.5.1 Device design .....	77
4.5.2 Fluoride removal after radiolabelling .....	79
4.5.3 Reaction-yield measurement .....	82
4.6 Summary .....	83
CHAPTER 5: Mirrored configuration of anodized dielectrics for electrowetting .....	86
5.1 Overview .....	86
5.2 Anodized dielectrics for EWOD .....	88
5.3 Mirrored configuration of anodized dielectrics for EWOD.....	89
5.4 Anodization.....	90
5.5 Testing the mirrored configuration of anodized dielectrics for EWOD .....	91
5.5.1 Sample fabrication .....	91
5.5.2 Experimental setup .....	94



5.5.3 Results for parallel-plate EWOD.....	95
5.5.4 Results for coplanar EWOD.....	100
5.6 Summary.....	102
CHAPTER 6: Summary and Conclusions.....	104
REFERENCES .....	107

## LIST OF FIGURES

Figure 1.1: Schematic of preclinical PET imaging .....	2
Figure 1.2: EWOD contact angle change .....	9
Figure 1.3: Diagram of row of electrodes for moving a droplet with EWOD. ....	10
Figure 1.4: Schematic of EWOD radiosynthesizer .....	12
Figure 2.1: Multifunctional EWOD electrode .....	16
Figure 2.2: EWOD device with self-centering heater electrode .....	18
Figure 2.3: Loading and heating on self-centering heater .....	18
Figure 2.4: EWOD device with 4 concentric multifunctional electrodes .....	20
Figure 2.5: Loading and heating on 4 concentric multifunctional electrodes .....	21
Figure 2.6: Process flow to fabricate EWOD radiosynthesizer .....	24
Figure 2.7: Electronic control scheme to operate EWOD radiosynthesizer .....	25
Figure 2.8: Linear increase of resistance change with temperature .....	28
Figure 2.9: Heating of a 15 $\mu$ L DMSO droplet from room temperature to 100°C .....	29
Figure 2.10: Passive cooling from 100°C to room temperature .....	29
Figure 3.1: Synthesis schemes for four radiotracers produced on EWOD chip .....	32
Figure 3.2: Cerenkov imaging setup .....	40
Figure 3.3: Images of Cerenkov radiation emitted during fluoride concentration .....	42
Figure 3.4: Solvent exchange of fluoride with phase transfer catalyst .....	44
Figure 3.5: Radio-TLC and radio-HPLC chromatograms of [ $^{18}$ F]FDG .....	53
Figure 3.6: Small animal PET/CT image of mouse with [ $^{18}$ F]FDG .....	54
Figure 3.7: Radio-TLC and radio-HPLC chromatograms of [ $^{18}$ F]FLT .....	58

Figure 3.8: Biodistribution of EWOD synthesized [ <sup>18</sup> F]FLT in mouse.....	59
Figure 3.9: Radio-TLC and radio-HPLC chromatograms of [ <sup>18</sup> F]SFB .....	61
Figure 3.10: Radio-TLC and radio-HPLC chromatograms of [ <sup>18</sup> F]fallypride .....	62
Figure 3.11: PET image of [ <sup>18</sup> F]fallypride in striatum of mouse brain.....	64
Figure 4.1: Two methods of on-chip purification.....	67
Figure 4.2: Diagram of custom made cartridge for purification.....	69
Figure 4.3: Scheme of droplet being drawn across photoresist filter structures.....	71
Figure 4.4: Cross-section schematic of exposed alumina on EWOD cover plate for SPE of fluoride .....	72
Figure 4.5: Cover plate with a window to expose alumina under Teflon® .....	73
Figure 4.6: Radio-TLC analysis of fluoride removal on alumina exposed cover plate ....	76
Figure 4.7: Device for on chip SPE by mechanical filtration.....	78
Figure 4.8: Filtration across line of pillars using electrowetting .....	80
Figure 4.9: Radio-TLC analysis of fluoride removal with alumina particles.....	82
Figure 4.10: Cerenkov image reaction-yield measurent .....	83
Figure 5.1: Diagram of mirrored configuration for valve metal oxide .....	87
Figure 5.2: Anodization setup.....	90
Figure 5.3: Fabrication process flow for samples to test mirrored configuration .....	92
Figure 5.4: Coplanar EWOD devices with anodized tantalum pentoxide .....	93
Figure 5.5: Current leakage and electrowetting effect on tanatalum pentoxide, silicon nitride, and silicon oxide dielectrics .....	95
Figure 5.6: Current leakage vs electric field for typical and mirrored EWOD devices....	97

Figure 5.7: Current leakage under cycles of voltage pulse .....	98
Figure 5.8: Current leakage under cycles of AC voltage pulse .....	99
Figure 5.9: Current leakage and electrowetting effect on Ta <sub>2</sub> O <sub>5</sub> coplanar EWOD .....	101
Figure 5.10: Transportation of droplet on Ta <sub>2</sub> O <sub>5</sub> coplanar EWOD device .....	102

## LIST OF TABLES

Table 2.1: EWOD actuation of typical radiochemistry solvents and solutions .....	27
Table 3.1: Four diverse radiotracers synthesized using the same EWOD chip design.....	50
Table 3.2: Biodistribution of [ <sup>18</sup> F]FDG in mouse.....	56
Table 4.1: Adsorption of fluoride ion on various cover-plate surfaces.....	74

## ACKNOWLEDGEMENTS

I am very grateful to my Ph.D. advisor, Prof. CJ Kim, for his support and encouragement. I will always appreciate the lessons I've learned not just from his direct mentorship on research, but also by the openness and clarity with which he expresses his approach and reasoning for all matters.

I've been fortunate to be colleagues with many labmates to whom I have had fun getting to know, work with, and learn from. I have been touched by the ways they have found to help each other. In particular, I would like to thank Jian Gong and Gaurav Shah for their thoughtful guidance, Wyatt Nelson for his zen, Choongyeop Lee for his deep appreciation of graduate life, Leo Liu for his inquisitiveness, Muchen Xu for being an ideal friend, Wook Choi and James Jenkins for their humor, Janet Hur for her boisterous laugh, Prosenjit Sen for making improvements to the lab that are still being used years later, Coco Huang for her diligence, Guangyi Sun for his candor, Ryan Freeman for his kindness, Zhiyu Chen for his smile, and Jia Li for his enthusiasm. They taught me how simple things can make the workplace even more enjoyable.

For my main graduate project, I have been lucky to have wonderful collaborators in Prof. Michael van Dam and Prof. Pei Yui Keng, who truly welcomed me into their labs. I am thankful to have been partnered with many patient chemists, Huijiang Ding, Rashed Javed, Jeff Collins, Hee-kwon Kim, and Jack Lei. I am very grateful to Mark Lazari, who in addition to his own research takes on many tasks in support of others. I would like to thank Prof. Sam Sadeghi and Bob Silverman for developing the multi-channel temperature controller, Prof. Arion Chatziioannou and Alex Dooraghi for developing the Cerenkov setup, Prof. Anna Wu and

Kirstin Zettlitz for antibody labelling, the UCLA Ahmanson Biomedical Cyclotron Facility for providing [ $^{18}\text{F}$ ]fluoride, Prof. David Stout for use of radiolabelling facilities, and Darin Williams, Waldemar Ladno, and Nam Vu for mice imaging. This work would not have been possible without the help of the UCLA Nanoelectronics Research Facility and its staff who keep complex machines operating, share their expertise, and have been very accommodating. I would also like to thank Prof. Nagichettiar Satyamurthy who provided critical advice when we first started our EWOD radiochemistry project and whose passion for teaching and discussing research has inspired me greatly.

I am grateful to Prof. Andrea Kasko, Prof. Dan Kamei, Prof. Dino Di Carlo, and Prof. Pei-Yu Eric Chiou for giving me the opportunity to TA. Their trust and encouragement gave me a confidence to teach that I will always cherish. I am also indebted to Prof. Liwei Lin and Prof. Bill Moses for giving me a chance to participate in research early on and guiding me to graduate school.

I am most thankful to my parents who made sure I really wanted to go to graduate school and have supported me throughout, and Sutin and Roo who shared the wise advice of older siblings. I also wish to thank Amber and the Markleys for welcoming me into their family and the friends who helped me grow here.

The majority of Chapter 3 is a combination of materials from the manuscript and supplementary information from a journal article: S. Chen, M. R. Javed, H.-K. Kim, J. Lei, M. Lazari, G. J. Shah, R. M. van Dam, P.-Y. Keng, and C.-J. Kim, “Radiolabelling diverse positron emission tomography (PET) tracers using a single digital microfluidic reactor chip,” *Lab on a Chip*, vol. 14, 902-910 (2014).

## VITA

2005	B. S., Biongeering University of California, Berkeley
2005-2006	Research & Development Engineer Intern Boston Scientific Fremont, California
2006-2014	Graduate Student Researcher Teaching Assistant Bioengineering Department University of California, Los Angeles

## JOURNAL PUBLICATIONS

**S. Chen** and C.-J. Kim, "Reliable electrowetting-on-dielectric with valve metal oxide in mirror-image configuration," in preparation.

**S. Chen**, M. R. Javed, H.-K. Kim, J. Lei, M. Lazari, G. J. Shah, R. M. van Dam, P.-Y. Keng, and C.-J. Kim, "Radiolabelling diverse positron emission tomography (PET) tracers using a single digital microfluidic reactor chip," *Lab on a Chip*, vol. 14, 902-910 (2014).

M.R. Javed, **S. Chen**, H.-K. Kim, L. Wei, J. Czernin, C.-J. Kim, R. M. van Dam, and P.-Y. Keng, "Efficient radiosynthesis of 3'-deoxy-3'-<sup>18</sup>F-fluorothymidine using electrowetting-on-dielectric digital microfluidic chip," *Journal of Nuclear Medicine*, vol. 55, 321-328 (2013).

M. R. Javed, **S. Chen**, J. Lei, J. Collins, M. Sergeev, H.-K. Kim, C.-J. Kim, R. M. van Dam, and P.-Y. Keng, "High yield and high specific activity synthesis of [<sup>18</sup>F]fallypride in a batch microfluidic reactor for micro-PET imaging," *Chemical Communications*, vol. 50, 1192-1194 (2014).

A. A. Dooraghi, P.-Y. Keng, **S. Chen**, M. R. Javed, C.-J. Kim, A. F. Chatziioannou, and R. M. van Dam, "Optimization of microfluidic PET tracer synthesis with Cerenkov imaging," *Analyst*, vol. 138, 5654-5664 (2013).

G. J. Shah, H. Ding, S. Sadeghi, **S. Chen**, C.-J. Kim, and R. M. van Dam, "On-demand droplet loading for automated chemistry on digital microfluidics," *Lab on a Chip*, vol. 13, 2785-2795 (2013).



H. Ding, S. Sadeghi, G.J. Shah, **S. Chen**, P.-Y. Keng, C.-J. Kim, and R.M. van Dam, “Accurate dispensing of volatile reagents on demand for chemical reactions in EWOD chips,” *Lab on a Chip*, vol. 12, 3331-3340 (2012).

P.Y. Keng, **S. Chen**, H. Ding, S. Sadeghi, G. J. Shah, A. Dooraghi, M. E. Phelps, N. Satyamurthy, A. F. Chatziioannou, C.-J. Kim, and R. M. van Dam, “Micro-chemical synthesis of molecular probes on an electronic microfluidic device, *Proceedings of the National Academy of Sciences*, vol. 109, 690-695 (2012).

S. Sadeghi, H. Ding, G. J. Shah, **S. Chen**, P.-Y. Keng, C.-J. Kim, and R. M. van Dam, “On chip droplet characterization: A practical, high-sensitivity measurement of droplet impedance in digital microfluidics,” *Analytical Chemistry*, vol. 84, 1915-1923 (2012).

T. Kawano, D. Christensen, **S. Chen**, C. Y. Cho, and L. Lin, “Formation and characterization of silicon/carbon nanotube/silicon heterojunctions by local synthesis and assembly”, *Applied Physics Letters*, vol. 89, 163510 (2006).

#### CONFERENCE PRESENTATIONS

**S. Chen** and C.-J. Kim, “Mirrored anodized dielectric for reliable electrowetting,” in *Proc. IEEE Int. Conf. MEMS*, San Francisco, CA, U.S.A., pp. 1011-1014 (2014).

**S. Chen**, A. A. Dooraghi, M. Lazari, R. M. van Dam, A. F. Chatziioannou, and C.-J. Kim, “On-chip product purification for complete microfluidic radiotracer synthesis,” in *Proc. IEEE Int. Conf. MEMS*, San Francisco, CA, U.S.A., pp. 284-287 (2014).

**S. Chen**, J. Lei, R. M. van Dam, P.-Y. Keng, C.-J. Kim, “Planar alumina purification of  $^{18}\text{F}$ -labeled radiotracer synthesis on EWOD chip for positron emission tomography (PET), in *Proc. Int. Conf. Miniaturized Systems for Chemistry and Life Sciences*, Okinawa, Japan, pp. 1771-1773 (2012).

**S. Chen**, M. R. Javed, J. Lei, H.-K. Kim, G. Flores, R. M. van Dam, P.-Y. Keng, and C.-J. Kim, “Synthesis of diverse tracers on EWOD microdevice for positron emission tomography (PET),” in *Technical Digest of Solid-State Sensor and Actuator Workshop*, Hilton Head Island, SC, U.S.A., pp. 189-192 (2012).

**S. Chen**, P.-Y. Keng, R. M. van Dam, and C.-J. Kim, “Synthesis of  $^{18}\text{F}$ -labeled probes on EWOD platform for positron emission tomography (PET) preclinical imaging,” in *Proc. Int. Conf. MEMS*, Cancun, Mexico, pp. 980-983 (2011).

**S. Chen**, H. Ding, G. J. Shah, R. M. van Dam, and C.-J. Kim, “EWOD microdevices for synthesis of  $^{18}\text{F}$ -labeled tracers for positron emission tomography (PET),” in *Technical Digest of Solid-State Sensor and Actuator Workshop*, Hilton Head Island, SC, U.S.A., pp. 37-40 (2010) (Oral presentation).

# **CHAPTER 1: INTRODUCTION**

## **1.1 Production of radiotracers for positron emission tomography (PET)**

### **1.1.1 Positron emission tomography (PET) and radiotracers**

Positron emission tomography (PET) is a non-invasive imaging technique for quantification of biomolecular processes through detection of gamma rays (Fig. 1.1) [1]. The detected gamma rays are produced by annihilation of a positron (emanated from a radiotracer) and an electron. A radiotracer is a biochemical compound tagged with a short-lived radionuclide, and the type of radiotracer determines the specific biological function that can be quantified via PET: sugars for monitoring carbohydrate metabolism, nucleic acids for examining cell replication, and neurotransmitters for studying brain activity or structure. The ability to capture these molecular functions make PET a powerful medical tool used for diagnosing disease (like cancer and Alzheimer's disease), monitoring treatment, and developing pharmaceuticals [2, 3].

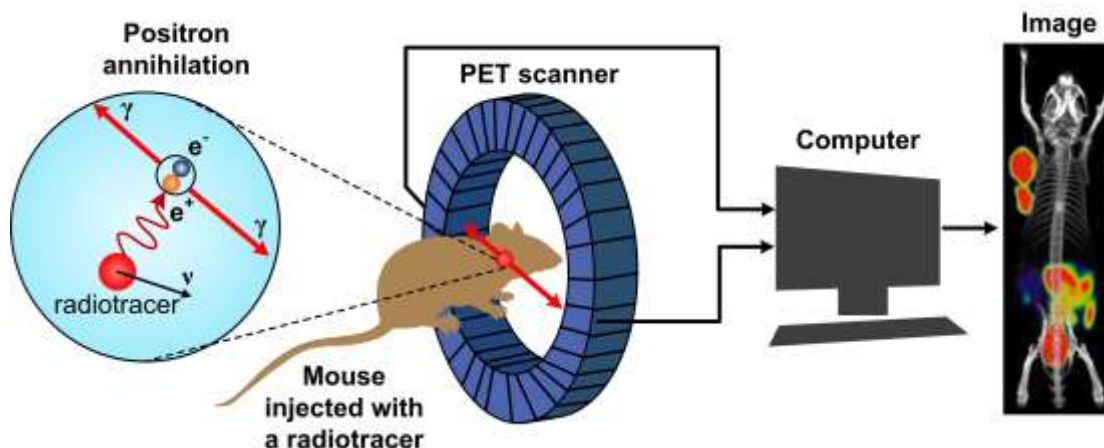


Figure 1.1: Schematic of preclinical PET imaging. A mouse is injected with a radiotracer before placement in a PET scanner. The radiotracer emits a positron which annihilates with an electron in the surrounding tissue, generating two 511 keV gamma rays. The gamma rays are detected by the PET scanner, and the data is converted into an image by a computer. The PET/CT image shown was taken from a mouse injected with an EWOD produced radiotracer [4].

Fluorine-18 is an ideal radioisotope for PET imaging because it emits a low energy positron compared to other positron-emitters and therefore has a relatively short positron linear range in tissue (maximum of 2.3 mm in water), thus allowing higher resolution images. Fluorine-18 also decays to an innocuous  $^{18}\text{O}$ , and has a moderate half-life that is long enough for multi-step chemical synthesis, transportation to PET imaging clinic, and imaging molecules *in vivo* [5]. Its 109.8 minute half-life is longer compared to carbon-11 (20.3 minutes), nitrogen-13 (10.0 minutes), and oxygen-15 (2.0 minutes) [6]. It can be produced by the cyclotron in large amounts (>10 curie) and in high specific activity [7]. The fluorine atom can also be labeled onto many

biomolecules because it is bioisostere to oxygen and can often substitute for a hydroxyl group or replace a hydrogen atom bound to a carbon atom [8]. Furthermore, the labelling yields in synthesis of fluorine-18 are considered relatively high for PET radiotracers at 20-40% [7].

However, fluorine-18 chemistry often faces several problems. [ $^{18}\text{F}$ ]fluoride is obtained from a cyclotron in [ $^{18}\text{O}$ ]water, but the bulk water must be removed for the fluoride to have adequate nucleophilicity for most radiolabelling reactions. Also, because only a low mass of fluoride is used, its loss due to adsorption can be significant, especially on the Pyrex vials traditionally used [9].

### **1.1.2 Need for improved radiotracer availability**

Over the last three decades, more than 1,400 fluorine-18 radiotracers have been developed in research settings for imaging biological processes, but only a handful are commercially available [10]. Although the most commonly used radiotracer, [ $^{18}\text{F}$ ]fluoro-2-deoxy-D-glucose ([ $^{18}\text{F}$ ]FDG) has had success as a general PET radiotracer in cancer and brain studies, there are cases where it has been proven suboptimal (such as in prostate cancer and well-differentiated tumors) and imaging studies could be improved with other more specific radiotracers [11].

Production of radiotracers is limited by large capital investment in equipment and infrastructure, high operating costs, and short tracer lifetime [12]. In the current centralized production system, fluorine-18 radiotracers can be prepared at one main facility and then distributed over a relatively large geographical area to PET imaging centers [13]. However, centralized production limits the variety of radiotracers available to respond to acute clinical

demand or explore the use of radiopharmaceuticals for therapeutic applications [14]. In order to improve access to different radiotracers, there has recently been a movement towards development of technologies for decentralizing PET radiotracer production, in which imaging centers synthesize their own radiotracers onsite after receiving radioisotopes from radiopharmacies.

There are many challenges in producing radiotracers that are not usually encountered with standard nonradioactive chemistry processes. First, there are unavoidable time constraints due to the short half-lives of positron emitting radioisotopes used (as the radiation is intended to decay before causing a cumulative harmful effect within the body). As a general rule, preparation of PET tracers should be completed within two to three-half-lives of the radionuclide, and this time constraint has driven development of rapid chemical methods [6]. Second, there are safety issues in dealing with ionizing radiation. Chemists need to be protected by heavy lead shielding and process automation.

### **1.1.3 Automated radiosynthesizers**

Because of the unique safety requirements for PET radiotracer synthesis, it has been important to develop automated systems. Automated radiosynthesizers can speed up synthesis time, increase reproducibility and efficiency of radiochemistry, and reduce radiation exposure to chemists [15, 16]. For these reasons, the use of automated radiochemical synthesis apparatus was recommended by a FDA guidance document on synthesis of radiotracers for preclinical and clinical use, “PET Drug Products—Current Good Manufacturing Practice (cGMP)”.

Automated synthesizers were pioneered for solid-phase peptide synthesis by Merrifield et al. [17] and have also been developed for DNA synthesizers used in mapping the human genome [18]. However, automated benchtop synthesis systems intended for peptide synthesis and DNA synthesis applications were designed for only a narrow range of chemistries and could not be used to automate radiosynthesis, which in general requires a broader range of synthetic organic chemistry to perform chemical transformations with multistep labelling procedures [19, 20].

Early radiosynthesis used manipulator arms, electric switches, regulated pressure sources, and temperature controllers and were controlled remotely by a human operator, who remained safe from positron emitting nuclides (often curie levels) through shielding and distance [21, 22]. The systems transferred reagents, evaporated solvents, and heated to controlled temperatures. Automated systems were then developed using hardwired timers, limit switches, and photodetectors for production of [<sup>18</sup>F]FDG, carbon-11 glucose, and several other radiopharmaceuticals [23, 24]. Automation of radiosynthesizers developed with technology using microprocessors, microcomputers, and programmable logic controllers, and is now currently performed through personal computers [19, 25].

The majority of commercial automated radiosynthesizers had been developed specifically for [<sup>18</sup>F]FDG synthesis (achieving 55-60% radiochemical yields) [20], but many (*e.g.*, GE TracerLab, Eckert & Ziegler Modular Lab Standard, and Synthra RNplus) are now being developed for flexible synthesis of various PET radiotracers using one machine [26, 16]. However, these systems may require manual reconfiguration to synthesize different radiotracers [20] and must be operated within expensive and bulky hot cells (special chemical fume hoods that are surrounded by lead to provide radiation shielding). Other systems (*e.g.*, Siemens

Explora® One, GE FASTlab, and IBA Synthera®) use disposable cassettes with stored reagents and defined fluidic paths to enable synthesis of different radiotracers without requiring the end-user to reconfigure the system. The typical automated synthesizers are 2-3 feet in width without shielding and purification equipment [16], but can be as small as 8 inches in width in the case of IBA Synthera® modular synthesizer. Connections to high-performance liquid chromatography (HPLC) for purification add to the shielded volume, but automated synthesizers can also use solid-phase extraction (SPE) cartridges as a faster and more space-conservative purification method for a small number of well-developed radiotracers [20].

#### **1.1.4 Microfluidic radiosynthesizers**

Because radiotracer synthesis is typically carried out in volumes of 5  $\mu\text{L}$  to 5 mL [19], it is a natural fit for microfluidic systems. Special miniature scaled equipment is already used in radiochemistry because of the minimal mass of reactants, which are often less than 1 mg [27, 28]. Miniaturization by microfluidic systems is of direct interest for radiotracer development because of the substantial savings from both using less lead shielding and reducing use of expensive reagents. Reaction efficiency can also be improved with reduced volumes because of increased concentration of the radioisotope, expedited heat transfer, and quicker mass transport [5, 29]. This is important for radiosynthesis reactions that sometimes involve low-yields and short half-life isotopes [8]. While the small amount of product limits the utility of microfluidic chemical synthesis in some cases, it is not an issue for PET imaging, which requires product in only nanogram quantities [2].

Several microfluidic systems have been developed for radiotracer synthesis, including flow-through systems and elastomer batch-flow reactors [28, 30]. In a European Union collaborative project, a modular system for radiochemistry on chip (ROC) was developed as a flexible dose-on-demand synthesizer for different radiotracers [31]. The main modules were glass chips with etched fluidic channels that functioned to concentrate fluoride, mix, heat (for dehydration, solvent exchange, and reactions), and purify. Continuous flow was provided by syringe pumps and controlled with rotary valves. When the modules were connected to perform radiosynthesis of [ $^{18}\text{F}$ ]FDG, it produced crude yields of 60% with 86% radiochemical purity after purification, and could produce 10 mCi (the typically injected radioactivity of [ $^{18}\text{F}$ ]FDG in human studies) in 19 minutes.

Microfluidic production of a PET radiotracer for human use was recently reported by Lebedev et al. [32]. The system used a 5  $\mu\text{L}$  ion-exchange column for [ $^{18}\text{F}$ ]fluoride concentration, a 50  $\mu\text{L}$  injection molded microreactor chip, and HPLC-based purification to produce [ $^{18}\text{F}$ ]fallypride, a neuroimaging radiotracer, with decay-corrected yields of 37% in 45 minutes (from cyclotron unloading to reformulation). All doses passed quality control and were used in twelve patients for clinical brain imaging.

Commercial microfluidic radiosynthesizers such as the Advion NanoTek® [33], Scintomics  $\mu$ -ICR [34], and FutureChemistry *FlowSafe* have also been used for radiotracer synthesis [35]. Advion NanoTek® has been the most reported commercial microfluidic radiosynthesizer in scientific publications. It incorporates distribution valves, syringe pumps, sensors (pressure, temperature, radioactivity), and heated vials to store and deliver reagents, concentrate radioisotopes, and control reactions [36]. It is a modular system with a concentrator



module, pump module, and reactor module that can all be controlled by computer [33]. The NanoTek® can transfer liquid volumes as small as 10 µL through a 15.6 µL capillary reactor and has been used to synthesize [<sup>18</sup>F]FDG in 3 minutes with 62% yield [37]. Despite its ability to handle microfluidic volumes, the current Advion system is still sizable and expensive and does not reduce the required space or infrastructure compared to conventional systems.

## 1.2 Electrowetting-on-dielectric (EWOD)

A new and promising microfluidic approach of digital microfluidics [38, 39, 40] does not require mechanical valves, pumps, or channels, but instead uses electric potentials to manipulate liquids through the mechanism of electrowetting-on-dielectric (EWOD) [41]. In electrowetting, liquid droplets are manipulated by electrostatic actuation from an external electric field. To prevent electrochemical reactions between the liquid and the electrode surface when higher electric fields were applied, dielectrics were incorporated into conventional electrowetting [42].

Electrowetting can be described by a combination of Young's observation that droplet shape depends on interfacial tension and Lippmann's findings that an external electric field affects interfacial energy. Young described a trigonometric relationship between droplet contact angle and a balance of the interfacial tensions at the three-phase contact line (between liquid and surface ( $\gamma_{sl}$ ), between surface and gas ( $\gamma_{sv}$ ), and between liquid and gas ( $\gamma_{lv}$ )) (Fig. 1.2A).

$$\text{Young's equation: } \cos(\theta) = \frac{\gamma_{sv} - \gamma_{sl}}{\gamma_{lv}}$$

$$\text{Lippmann's equation: } \gamma = \gamma_0 - \frac{1}{2} CV^2 = \gamma_0 - \frac{1}{2} \frac{\epsilon_0 \epsilon_r}{d} V^2$$

where  $\gamma$  is the interfacial tension when an electric field is applied,  $\gamma_0$  is the solid-liquid interfacial tension when no electric field is applied,  $C$  is the capacitance per unit area,  $V$  is the applied potential,  $\epsilon_0$  is the dielectric constant of air,  $\epsilon_r$  is the dielectric constant of the insulating layer, and  $d$  is the thickness of the insulating layer.

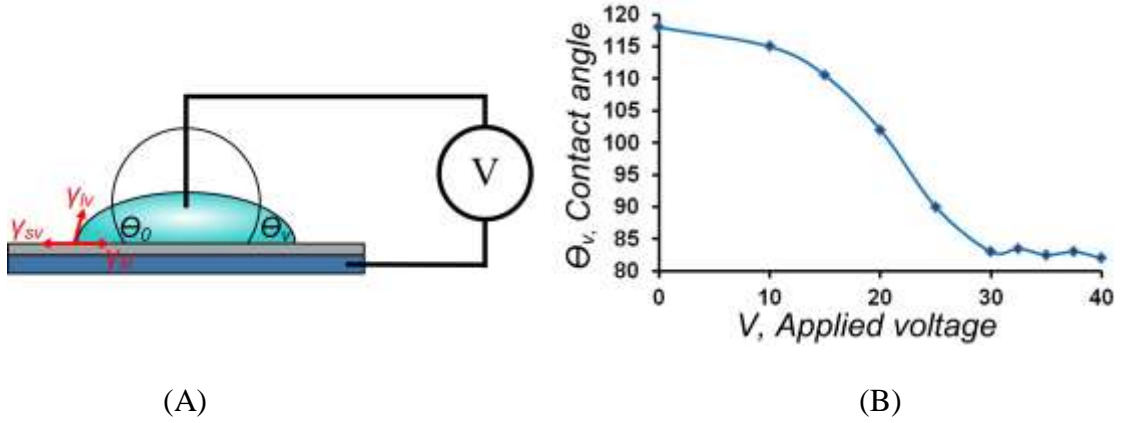


Figure 1.2: (A) EWOD contact angle change. A droplet in contact with a hydrophobic surface has a contact angle  $\Theta_0 > 90^\circ$ . When a voltage is applied, electrostatic between the droplet and the substrate causes an observed decrease in contact angle,  $\Theta_v$ . (B) Measured contact angle for a series of applied voltage (experimental data).

Together the two equations form the electrowetting equation:

$$\cos(\theta_v) - \cos(\theta_0) = \frac{\epsilon_0 \epsilon_r V^2}{2\gamma_{lv}d}$$

where  $\theta_v$  is the contact angle at applied potential  $V$  and  $\theta_0$  is the contact angle when no potential is applied. The electrowetting equation describes an apparent decrease in the liquid contact angle when an applied voltage is increased (Fig. 1.2B).

When voltage is applied for a sessile droplet on a single electrode, the droplet spreads in order to maximize its area over the electrode and dielectric. If multiple electrodes are arranged side-by-side, electrowetting can be used to move droplets from one electrode to the next (Fig. 1.3). Because it enables control over fluid shape and flow through electrical signals, EWOD actuation has found many applications including low-power displays [43], variable-focus lenses [44, 45], thermal switches [46], electrical switches [47], energy harvesting [48], and rheometers [49, 50]. As a lab on a chip platform [40], EWOD has been widely used for applications as diverse as combinatorial synthesis [51], sample processing [52, 53], enzyme-linked immunosorbent assay (ELISA) [54], and cell manipulation [55].

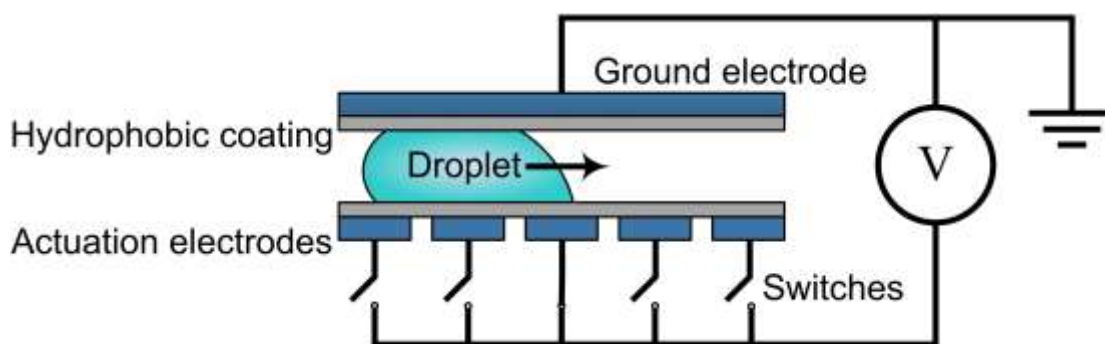


Figure 1.3: Diagram of a row of electrodes for moving a droplet with EWOD.

### 1.3 EWOD for radiotracer production

The EWOD-driven digital microfluidics has key advantages for radiotracer synthesis. Because droplet movement is electronically controlled without valves, pumps or tubes, liquid pathways can be defined in software, enabling diverse chemical synthesis procedures to be carried out with just one type of EWOD chip. Since the sidewalls of channels are not necessary,

an EWOD chip can be open to air, as first demonstrated by Lee *et al* [56]. The open-to-air configuration enables rapid drying for evaporation and solvent exchange; these are critical steps for no-carrier-added fluorination reactions, which are water-sensitive but begin with [ $^{18}\text{F}$ ]fluoride ion obtained in [ $^{18}\text{O}$ ]-enriched water from a cyclotron [8]. The low volumes (2-12  $\mu\text{L}$ ) used on the EWOD chip are conducive to simplifying the purification process and increasing specific activity (radioactivity per mass of tracer) due to the minute amount of reagents used in a single batch of synthesis [36, 57, 58].

Another potential advantage yet to be confirmed experimentally is reduced radiolysis, which is damage to the reagents due to formation of radicals by energy that is mainly deposited from positron emission. Because the EWOD droplets are squeezed within a gap that is smaller than the positron range, it is expected that a significant portion of positrons will be absorbed in the chip substrate rather than the solvent, which would significantly reduce the formation of radicals and radiolysis, in comparison with a macroscale geometry [59].

To avoid different chip designs for different tracers, in this report we explore and confirm a single EWOD chip design that could produce a variety of radiotracers (Fig. 1.4). Four exemplary radiotracers currently used in clinical and preclinical research are demonstrated: (1) [ $^{18}\text{F}$ ]FDG (a sugar analogue), (2), 3'-deoxy-3'-[ $^{18}\text{F}$ ]fluorothymidine ([ $^{18}\text{F}$ ]FLT, a DNA nucleoside analogue), (3) *N*-succinimidyl 4-[ $^{18}\text{F}$ ]fluorobenzoate ([ $^{18}\text{F}$ ]SFB, a prosthetic group for protein labelling), and (4) [ $^{18}\text{F}$ ]fallypride (a neurotransmitter analogue) [4, 58, 60, 61]. The EWOD platform, as an affordable and flexible synthesizer, has the potential to empower final users to produce tracers of their choice locally on demand and eliminate bottlenecks due to centralized production.

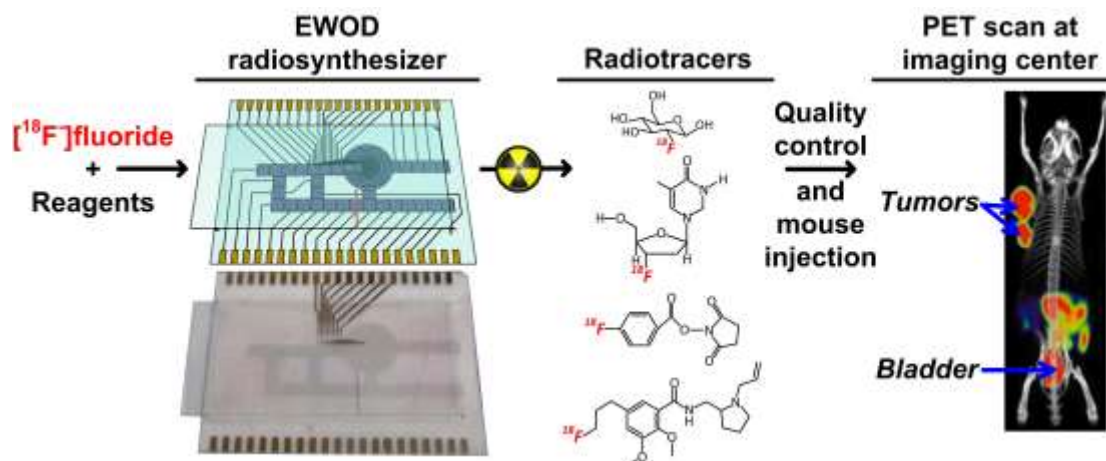


Figure 1.4: A single EWOD design is intended to produce a variety of radiotracers once [<sup>18</sup>F]fluoride and other reagents are added. After radiotracers are produced, quality control and injection must be performed before PET imaging.

#### 1.4 Summary of the chapter

The need for diverse synthesis of radiotracers for PET imaging has been presented in this chapter. Although recent developments in adding flexible functionality to automated benchtop synthesizers have been made to address this issue, there are still significant advantages to using microfluidic synthesizers instead. Of the microfluidic devices that have been developed for radiosynthesis, the EWOD radiosynthesizer is unique as the only batch reactor using droplets in air or an inert gas, which provides unique advantages in its flexibility for radiosynthesis and facilitates evaporation steps.

The next chapter discusses an EWOD device for radiosynthesis, its fabrication, and device testing. Multifunctional electrodes were designed for heating and temperature sensing, as well as EWOD actuation. EWOD actuation was tested for droplets of solutions relevant to radiochemistry. Temperature was measured on both heating plate and cover plate of the device in order to determine a temperature range for the droplet during heating.

Chapter 3 presents data from the synthesis of four different radiotracers using the same EWOD radiosynthesizer device design. Multifunctional electrodes on EWOD devices are used to perform concentration, solvent exchange, and chemical reaction steps for radiochemistry on chip.

Chapter 4 describes two methods for integrating purification steps on chip. One method involves modifying the EWOD plate surface to adsorb reagents. The second method adds filtering structures to the EWOD gap so that conventional solid-phase extraction particles can be used for purification and then filtered from the droplet.

Chapter 5 evaluates the use of anodized dielectrics for EWOD in a mirrored configuration, where the ground electrode is also covered by dielectric. This configuration addresses an issue with anodized dielectrics in that their insulating properties depend on the direction of the applied bias. Both lifetime tests and breakdown tests were used to confirm that in this mirrored configuration one side of the dielectric is always under the reverse bias to limit current leakage.

Chapter 6 summarizes this dissertation.

## CHAPTER 2: EWOD DEVICE WITH INTEGRATED HEATERS FOR RADIOCHEMISTRY

### 2.1 Overview

Heating is important in radiolabelling procedures, which use organic chemistry to label a radioactive nuclide onto a biomolecule. Temperature control in radiochemistry is critical, particularly for solvent exchange and reactions [62]. For example, in production of the most commonly used PET radiotracer, [ $^{18}\text{F}$ ]FDG, Arima et al. found improved fluorination yields with increasing temperatures up to 125°C, but lower yields at even higher temperatures because of decomposition of the precursor reagent and intermediate product [31].

Heating is also important for many lab-on-a-chip applications, such as polymerase chain reaction, cell culture, and protein crystallization. For that reason, there have been several reported approaches to control temperature in microfluidics. In some approaches, heat was applied to a microfluidic device or its fluids from an external source, such as Peltier devices [63], hot plates [64], incubators [65], or lasers [66]. Other approaches integrated heating into a microfluidic device using micro-Peltier components [67], resistive heaters [68], microwaves [69], or exothermal chemical reactions [70].

Because EWOD devices already require patterning of metal layers into electrodes for droplet movement, it is sensible to take an integrated approach and pattern the same metal for heating. With typical EWOD electrodes in a parallel plate configuration, it is possible to heat using dielectrophoresis or microwaves. Joule heating can occur during dielectrophoresis when high frequencies and high electric fields allow current to pass through the droplet [71]. In

microwave dielectric heating, high frequency electric fields can cause rapid alignment of both induced and intrinsic dipole moments and the associated energy may dissipate as heat [72]. However, both dielectrophoresis Joule heating and microwave heating processes are dependent on the liquid properties involved, such as solution conductivity for Joule heating and dielectric loss for microwave heating [69]. The power output required to heat a solution to a set temperature could vary significantly with the chemical composition of the solution. Although no changes to the typical EWOD electrode shape would be required for heating with dielectrophoresis or microwaves, such a method would also not easily integrate temperature measurement and feedback control over heating.

A simpler method for temperature control on an EWOD device is to Joule heat through an electrical resistor patterned from the metal layer with the same overall EWOD electrode shape, but two connection lines (instead of the single connection line to a typical EWOD electrode) (Fig. 2.1). Such electrodes were first demonstrated by Wei et al. [73]. When a current is applied through the resistor with a voltage difference along the two connection lines, on chip localized heating can be accomplished. In contrast, when the same voltage is applied to both connection lines, the electrode can be used for EWOD droplet movement. Wei et al. measured temperature with a thermocouple and showed that the droplet temperature was linearly proportional to the supplied power. Further work by Nelson et al. [74] showed that the same electrical resistor for heating can also be used as a thermistor for integrated temperature measurement and feedback control. During heating, resistance can be determined through sensing both the current and voltage supplied, and the changes in temperature can be calculated from the corresponding change in resistance.



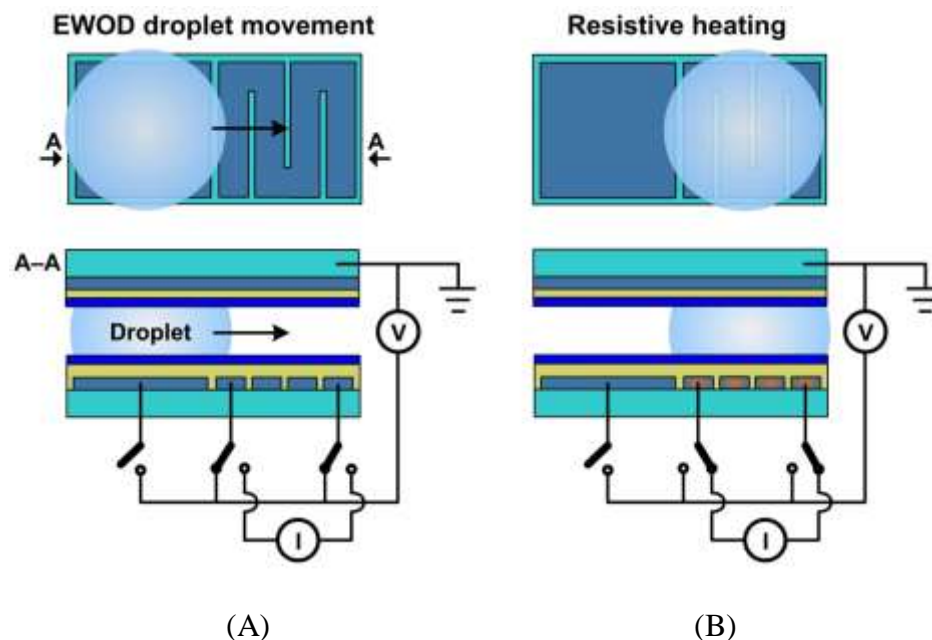


Figure 2.1: Multifunctional EWOD electrode for droplet movement, heating, and temperature sensing. (A) The droplet moves when a potential is applied to the heater. (B) The droplet is heated when current is passed through the heater. Adapted from [73, 74].

## 2.2 Multifunctional EWOD electrode for radiochemistry

### 2.2.1 Self-centering EWOD heaters

Nelson et al. [75] used an EWOD device with localized droplet heating to perform sample preparation for matrix-assisted laser desorption/ionization mass spectroscopy (MALDI-MS). Droplet heating accelerated trypsin digestion reaction rates, sample drying, and matrix crystallization. However, in order to control the location of the droplet as it evaporated with heat, the authors incorporated a hydrophilic pattern over the multifunctional electrodes by selective

plasma etching of the hydrophobic surface coating. Without the hydrophilic pattern, the droplet center of mass migrated because the liquid nearest to the center of the heater (the hottest point as long as there were no irregularities in the resistive heater) evaporated faster than liquid further from the center of the heater. The hydrophilic pattern did not interfere with MALDI-MS, because residue could remain on the EWOD device as the sample for spectrum measurement. However, for radiochemistry applications, it is important to move the droplet after reactions are completed so the product can undergo quality control procedures and be used as a radiopharmaceutical.

Instead of incorporating a hydrophilic pattern, initial EWOD devices designed for radiochemistry used a circular resistor pattern enclosed by the EWOD electrode for centering residue from evaporating droplets (Fig. 2.2). Each EWOD heating electrode had two connection lines and required a voltage difference applied to the lines to drive current for heating. Because one of the lines led to the center region and the opposite line led to the outer region of the electrode, voltages applied for heating simultaneously created an electric field for EWOD actuation. By supplying a higher EWOD voltage to the middle of the multifunctional electrodes, droplets could be centered by EWOD during heating without removing any of the hydrophobic topcoat (Fig. 2.3).

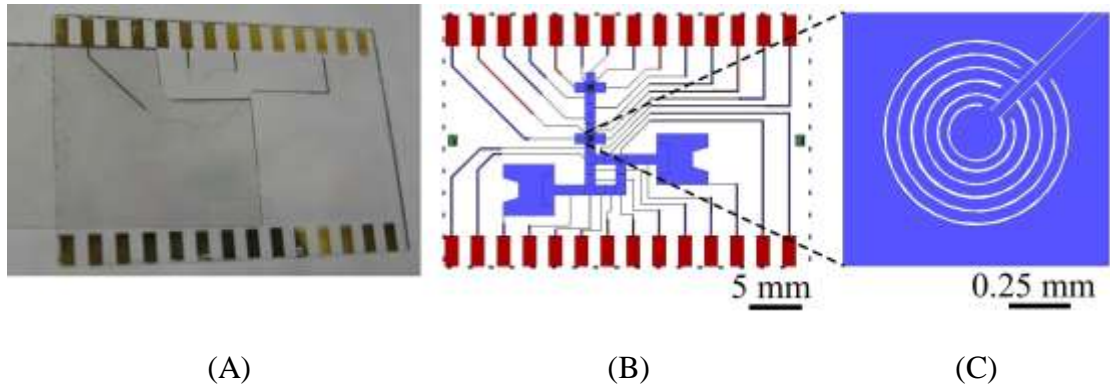


Figure 2.2: EWOD device with self-centering heater electrode. (A) Device with cover plate. (B) Device layout. (C) Zoomed in on heater layout.

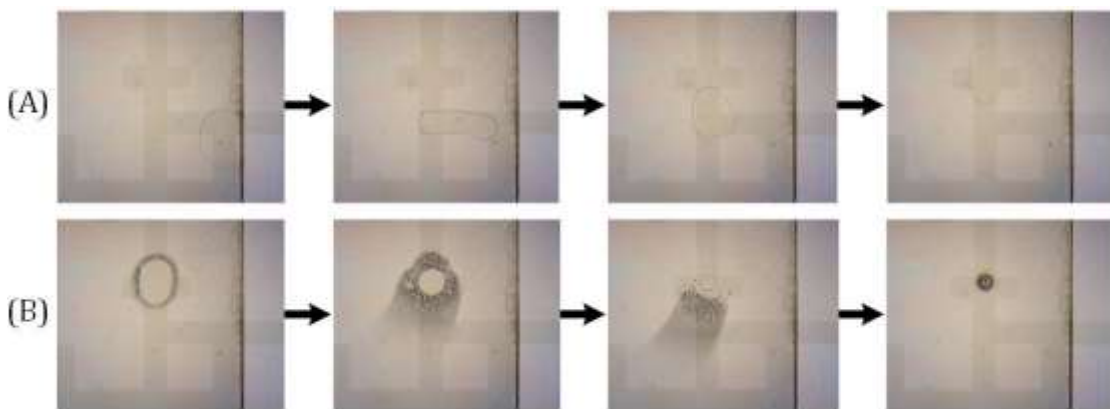


Figure 2.3: Droplet loading and heating on EWOD device with self-centering heater electrode. (A) Droplet movement by electrowetting. (B) Resistive heating of droplet with multifunctional electrode.

### 2.2.2 Concentric heater rings

Initial multifunctional electrodes had a footprint less than 4 mm<sup>2</sup> and could only fit droplet volumes less than 2 μL. In later designs, larger heating areas were desired to load larger volumes of cyclotron-produced [<sup>18</sup>F]fluoride in water for concentration. However, larger area presented an issue for thermistor temperature sensing over the electrode, because only the average temperature over the entire resistive heater was measured and used for feedback control. Temperature irregularities over the heater area (*e.g.* due to the droplet covering part of the heater) were not accounted for, but were assumed to have minimal impact for the initial multifunctional heating electrodes with small footprints. Over larger heater areas, significant temperature variations from the measured average were expected to be significant and were of particular concern for the squeezed droplets in parallel-plate EWOD devices, which require more surface area for a given volume.

A similar temperature control issue was addressed in the long tubular furnaces used by semiconductor processes for crystal growth and dielectric deposition [76]. It is difficult to control temperature along the entire furnace length if only a single heating element is used. However, with a segmented design of separate heating elements (instead of one continuous element) monitored by several thermocouples, temperature could be feedback controlled over the entire length of the furnace.

The segmented approach was used in later designs of the multifunctional electrodes for the radiochemistry EWOD device (Fig. 2.4). Instead of a single element, the larger reactor site (~110 mm<sup>2</sup>) consisted of four concentric circular multifunctional electrodes, each with its own feedback control over temperature.

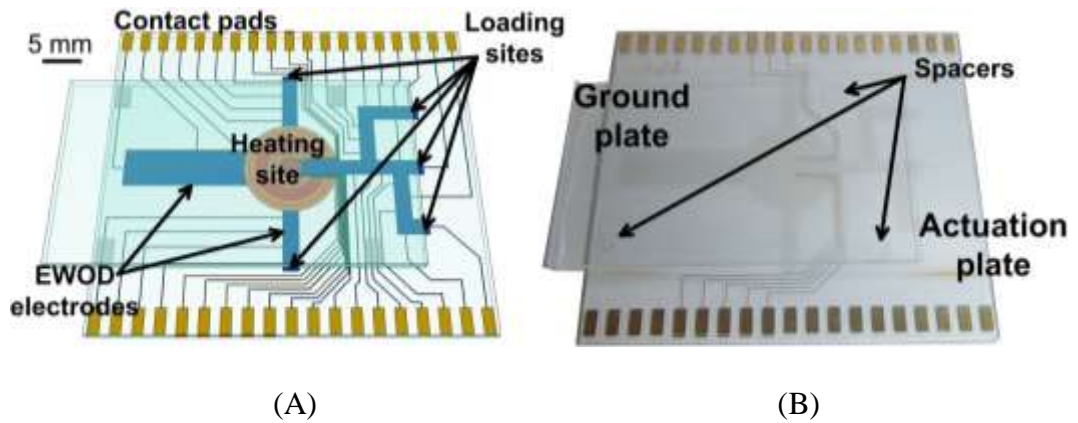


Figure 2.4: EWOD device with 4 concentric multifunctional electrodes. (A) Device layout with regular EWOD electrodes (blue) and multifunctional electrodes (orange and red). (B) Fabricated device with gold contact pads and gold connection lines to the multifunctional electrodes.

Compared to a simple heater, this multi-element heater could center the droplet and also maintain its temperature more uniformly as the droplet shrank during evaporation steps (Fig. 2.5). More specifically, power to the outer heating rings was lowered or cut off successively as each ring sensed its surface being dried (through reduced heat loss). If not divided into multiple heating rings, a single circular heater would sense one average temperature over its entire area. As the liquid droplet shrank, the heater surface outside the liquid would be overheated while the liquid would be under heated.

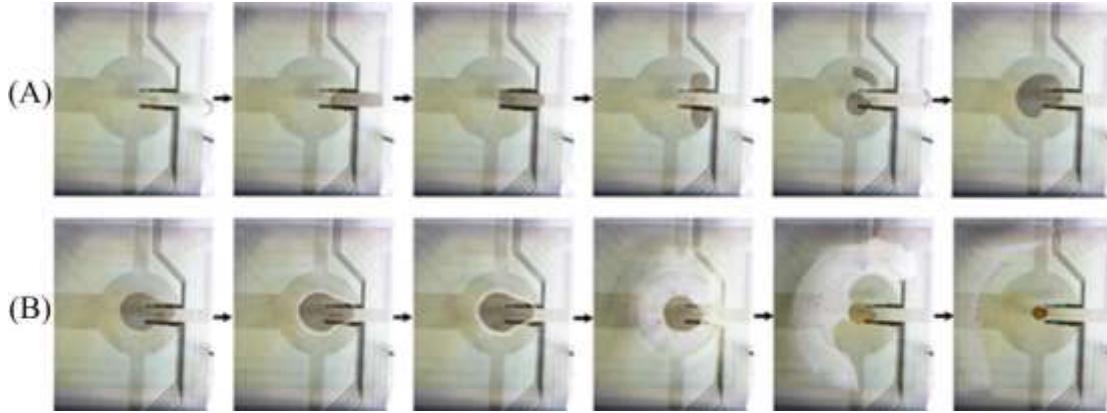


Figure 2.5: Droplet loading and heating on EWOD device with 4 concentric multifunctional electrodes. (A) Droplet movement by electrowetting. (B) Resistive heating of droplet with multifunctional electrode.

### 2.3 Fabrication of radiochemistry EWOD devices

The EWOD device in this dissertation has a configuration of two parallel plates with a gap space, in which droplets are sandwiched to a disk shape. The electrical ground plate is on top and uses a transparent conductive layer of indium tin oxide (ITO) to maintain a reference electrical connection for EWOD actuation. The actuation plate is on the bottom and has defined electrodes (also transparent ITO) for six droplet pathways that meet at a circular heating site.

ITO is commonly used for EWOD electrodes when visual or optical feedback is desired. It is also a useful heater material because it does not flake with heating (unlike nickel or copper) and has a relatively high thermal coefficient of resistance which enables more sensitive temperature measurement for a given resistance change [76].

The contact pads and connection lines to the heaters were etched from gold. Gold is useful for connections because it does not oxidize. For resistive heating, the majority of the voltage drop (and heating effect) should occur on the heater rather than the connection lines. Similarly, for thermistor temperature sensing, the connection lines should only have a minimal factor on the total heater resistance measured. Gold is useful as a connection line material, because compared to ITO, its conductivity is around 50 times greater and its thermal coefficient of resistance is 4 times less.

Silicon nitride was used as a dielectric for electrowetting. Its dielectric constant of 6-8 is relatively high (which is conducive for electrowetting), it is easy to deposit with IC processes, and it has a high chemical resistance.

Teflon® was used as the hydrophobic topcoat to achieve greater contact angle changes for electrowetting. Other hydrophobic polymers like Cytop® (glass transition temperature  $T_g = 108^\circ\text{C}$ ) have been demonstrated as superior hydrophobic coating materials for electrowetting, because their surfaces are charged less than Teflon® over repeated voltage cycling [77]. However, in radiochemistry processes, where heated reaction temperatures can approach  $200^\circ\text{C}$ , high thermal stability is also required. Teflon® AF 2400 ( $T_g = 240^\circ\text{C}$ ) was chosen for its higher thermal stability. Teflon® AF 2400 was considered more stable than both Teflon® AF 1600 ( $T_g = 160^\circ\text{C}$ ) and Cytop®, which were used on earlier devices. After the hydrophobic topcoat was switched to Teflon® AF 2400, less residual radioactivity remained “stuck” to the device surface after synthesis. Compared to the initially loaded activity, the extracted product increased from 45% to 77% (decay-corrected) for 3'-deoxy-3' [ $^{18}\text{F}$ ]fluorothymidine ([ $^{18}\text{F}$ ]FLT) synthesis.

One concern with Teflon® is that it can be a source for fluorine-19 contamination into the reagents and result in a lower specific activity (radioactivity per mass of tracer) of the final product [78]. However, because [<sup>18</sup>F]fallypride synthesized by EWOD has some of the highest reported specific activity (19 Ci μmol<sup>-1</sup>), fluorine-19 contamination from Teflon® appears not likely to be a major issue [58].

Both EWOD actuation plates and electrical ground plates were diced from 700 μm thick glass wafers coated with 140 nm ITO (Semiconductor Solutions) (Fig. 2.6). Chromium (20 nm) and gold (200 nm) were evaporated onto the wafers. The gold, chromium, and ITO layers were patterned to form EWOD electrodes, heaters, connection lines, and contact pads by photolithography and wet etching. The silicon nitride dielectric was deposited by plasma-enhanced chemical vapor deposition (PECVD) at a thickness of 2 μm on the actuation plate and a thinner 100 nm on the electrical ground plate. Teflon® (250 nm) was spin-coated and annealed at 350°C under vacuum to make the surfaces hydrophobic. A 140 μm gap between the assembled actuation plate and electrical ground plate was maintained by two layers of double-sided tape (3M Inc.).



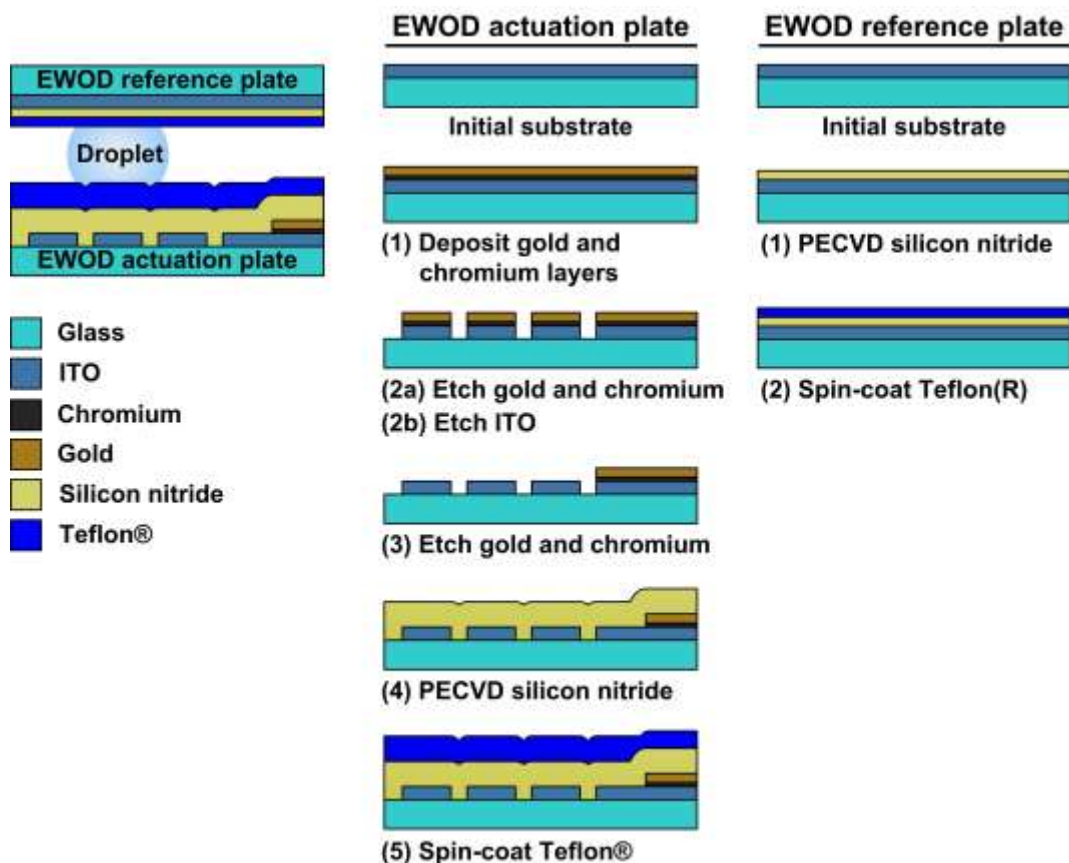


Figure 2.6: Process flow to fabricate EWOD actuation plate and ground plate with multifunctional electrodes.

## 2.4 EWOD control system

The EWOD device was operated inside an enclosure behind lead shielding. An electrical control box outside of the lead shielding contained a waveform generator, voltage amplifier, solid-state relays, a multichannel heater driver, and two digital I/O devices (Fig. 2.7). The EWOD device and imaging cameras within the enclosure were electrically connected to the control box by ribbon cables. The EWOD actuation voltage for radiosynthesis droplet

movement was generated from a 10 kHz signal (33220A waveform generator, Agilent Technologies) and amplified to 100 V<sub>rms</sub> (Model 601C, Trek). The voltage was applied selectively to desired electrodes for droplet movement by solid-state relays (AQW610EH PhotoMOS relay, Panasonic) that were controlled by a LabVIEW program using a digital I/O device (NI USB-6509, National Instruments).

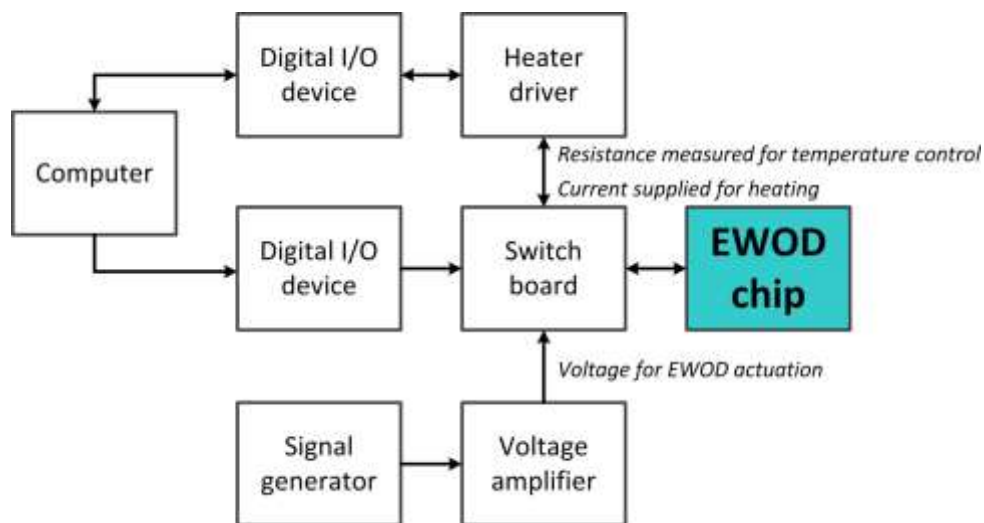


Figure 2.7: Electronic control scheme to operate the EWOD chip for tracer synthesis. A computer controls a switchboard through a digital input/output device. The switches connect the electrodes on the EWOD chip to an amplified voltage for EWOD actuation. When necessary, some switches connect the multifunctional electrodes to a heater driver for temperature sensing and resistive heating via feedback control from the computer through a second digital input/output device.

The device's multifunctional electrodes were connected to switches, which alternated between connections for EWOD actuation and connections for heating and temperature measurement. To maintain precise feedback-controlled temperatures over the four concentric multifunctional electrodes, a multichannel heater controller and driver were built. It incorporated a low noise, real-time, zero resistance current measurement, and also provided a self-powered, amplified voltage output with parameters controlled by a LabVIEW program.

## **2.5 Movement of liquids and droplet splitting**

Solvents and solutions commonly used for radiotracer synthesis were tested for EWOD compatibility and summarized in Table 2.1. Repeatable movement, splitting, and merging of droplets were accomplished with DI water, acetonitrile (MeCN), methanol (MeOH), dimethyl sulfoxide (DMSO), dimethylformamide (DMF), hexyl alcohol, tetrabutylammonium bicarbonate ( $\text{TBAHCO}_3$ ), *N,N,N',N'*-tetramethyl-*O*-(*N*-succinimidyl)uranium hexafluorophosphate (HSTU, 98%), hydrochloric acid (HCl, 1 N), sodium hydroxide (NaOH, 1 N) and Kryptofix 2.2.2/potassium carbonate in water ( $\text{K2.2.2/K}_2\text{CO}_3$ , 130/35 mM), with voltages below 100  $V_{\text{rms}}$  and frequencies ranging 0-20 kHz.

Table 2.1: EWOD actuation of typical radiochemistry solvents and solutions.

Liquid	Conc.	<i>f</i> (Hz)	<i>V</i> (Vrms)	Move	Split	Vapor pres (mmHg, 20°C)	Boiling point (°C)
<i>DI water</i>	pure	1000	60	Y	Y	17.5	100
<i>MeCN</i>	pure	500	40	Y	Y	73	82
<i>MeOH</i>	pure	100	50	Y	Y	97	65
<i>DMSO</i>	pure	1000	80	Y	Y	0.42	189
<i>DMF</i>	Pure	20000	80	Y	Y	2.7	153
<i>Thexyl Alcohol</i>	pure	1000	60	Y	Y	8.5	118
<i>TBAHCO<sub>3</sub></i>	75 mM	1000	80	Y	Y	(water/ethanol)	
<i>K<sub>2</sub>.2.2/K<sub>2</sub>CO<sub>3</sub> in water</i>	130 / 35 mM	1000	80	Y	Y	(water)	
<i>HCl</i>	1 M	1000	60	Y	Y	(water)	
<i>NaOH</i>	1M	1000	60	Y	Y	(water)	

## 2.6 Droplet heating

### 2.6.1 Heating on multifunctional electrodes

The temperature coefficient of resistance (TCR) was measured for individual resistive heating electrodes before EWOD devices were used for radiosynthesis. For TCR measurement, changes in the heater resistance were recorded over a series of temperature increments while the device and a thermocouple were immersed in a bath over a hot plate. A linear increase of heater resistance with temperature was established with initial calibrations using a silicone oil fluid bath at temperatures up to 155°C. Later devices were calibrated in a water bath at temperatures up to

90°C in order to avoid more rigorous cleaning that is required with silicone fluid. The TCR of the thin-film ITO heaters was measured on average as  $0.00098 \text{ K}^{-1}$ .

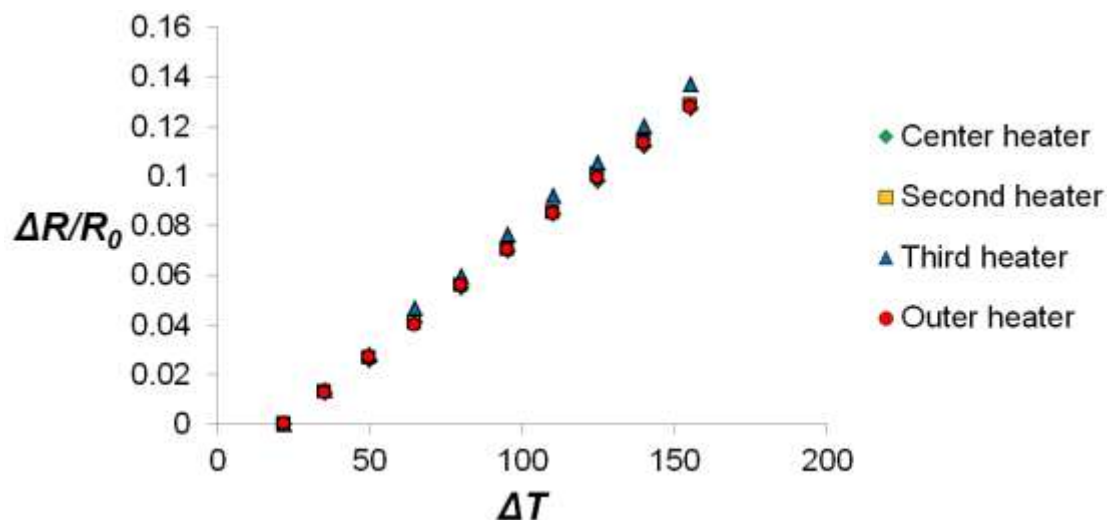


Figure 2.8: Linear increase of resistance change with temperature measured for all four multifunctional heaters on the same device.

The calibrated TCR was used by the LabVIEW heater control program to determine the heater temperature (relative to ambient temperature) based on the difference between resistance measurements taken during heating and resistance measured at ambient temperature. In heater tests with a  $15 \mu\text{L}$  droplet of DMSO squeezed between the EWOD plates, the heater temperature rose to a set temperature of  $100^\circ\text{C}$  in 1 minute under damped control, as shown in Fig. 2.9. The heater can ramp temperature more quickly if different control factors are used. However, preventing an overshoot in the reaction temperature is more important for consistent radiochemical production than quick heating times.

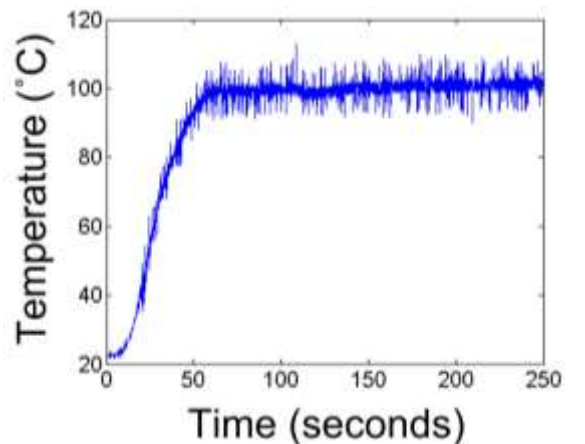


Figure 2.9: Heating of a 15  $\mu\text{L}$  DMSO droplet from room temperature to 100°C.

No active cooling was used with the EWOD radiosynthesizer device. Instead, power was shut off to the heater except for 0.5 mW due to current that was necessary for measuring temperature. It took the heater more than 3 minutes to cool down from 100°C to room temperature, as shown in Fig. 2.10. Impact of the long passive cooling time was limited for additional reaction steps by loading subsequent reagent droplets to the heater at temperatures below 60°C, instead of waiting for the heater to cool to room temperature.

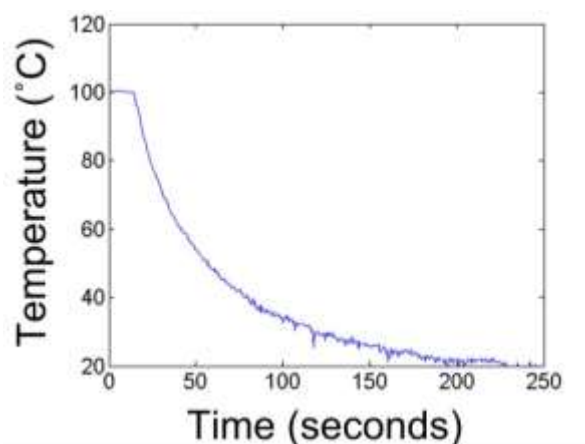


Figure 2.10: Passive cooling from 100°C to room temperature.

## 2.6.2 Droplet temperature

Temperature control is critical in radiochemistry to provide enough energy for chemical reactions and also limit thermal degradation of reagents or loss of volatile side-products [79]. Temperature control can also be important in water removal steps, which are necessary for no-carrier-added fluorination reactions.

For our EWOD radiosynthesis device, the measured temperature used for feedback control is the average temperature of the integrated heating electrode. But the temperature that is most relevant to the radiochemistry process is the droplet temperature, which can be considered to be the reaction temperature. During the design of the EWOD device, it was assumed that the droplet temperature would be similar to the heater temperature because the droplet and heater are only physically separated by thin dielectric and hydrophobic layers. Although the dielectric and hydrophobic layers consist of thermally insulating silicon nitride and Teflon®, their less than 2.5  $\mu\text{m}$  total thickness should not significantly interfere with heat transfer from the heater to the droplet.

In tests to confirm that the droplet temperature is similar to the heater temperature, a multifunctional electrode was used to measure the cover plate surface temperature during heating. Droplet temperature was not directly measured, but its temperature range was determined from measurements on the plates above and below it. Because heat is only transferred from the higher temperature objects to lower temperature objects and heat flow is from the heater through the droplet to the cover plate, the droplet cannot be hotter than the heater plate and it cannot be cooler than the cover plate. In the case of a 15  $\mu\text{L}$  droplet of DMSO heated at 100°C, the cover plate temperature was measured as 95.3°C for a 140  $\mu\text{m}$  plate gap (the gap used during

radiosynthesis on EWOD devices), 90.6°C for a 280  $\mu\text{m}$  plate gap, and 85.2°C for a 420  $\mu\text{m}$  plate gap. It took 74 seconds to reach a steady temperature for a 140  $\mu\text{m}$  plate gap, 76 seconds to reach a steady temperature for a 280  $\mu\text{m}$  plate gap, and 78 seconds to reach a steady temperature for a 420  $\mu\text{m}$  plate gap.

For more accurate control of droplet temperature, a heater can be used on the cover plate, so that the droplet is heated both from above and below. In such a condition, the lowest temperature of the droplet would be on the outer edge of its circumference. Because the droplet is squeezed (the diameter of a 15  $\mu\text{L}$  droplet is more than 80 times greater than the 140  $\mu\text{m}$  gap), the droplet temperature should closely match the heater temperature if the droplet is being exposed to equal temperatures from both plates. However, incorporating heaters on the cover plate would add both complexity and cost to the fabrication, and we did not find it necessary for radiosynthesis using a thin 140  $\mu\text{m}$  plate gap.

## **2.7 Summary**

In this chapter, we have described the design and fabrication of an EWOD device with multifunctional electrodes for radiochemistry. In order to test its ability to perform radiotracer synthesis, the EWOD device was used to move, split, and merge droplets of reagents typically used in radiochemistry. The multifunctional electrodes' ability to control the temperature of droplets was also evaluated. The next chapter will describe the use of this EWOD device as a radiosynthesizer.



## CHAPTER 3: RADIOLABELLING CHEMISTRY ON EWOD

### 3.1 Overview

This chapter describes the basic steps required for radiolabelling chemistry and performing those steps on one EWOD chip design in order to synthesize four exemplary radiotracers that are currently used in clinical and preclinical research: (1) [ $^{18}\text{F}$ ]fluoro-2-deoxy-D-glucose ([ $^{18}\text{F}$ ]FDG, a sugar analogue), (2) 3'-deoxy-3'-[ $^{18}\text{F}$ ]fluorothymidine ([ $^{18}\text{F}$ ]FLT, a DNA nucleoside analogue), (3) N-succinimidyl 4-[ $^{18}\text{F}$ ]fluorobenzoate, ([ $^{18}\text{F}$ ]SFB, a protein labelling compound), and [ $^{18}\text{F}$ ]fallypride (a neurotransmitter analogue). Synthesis schemes for each radiotracer are shown in Fig. 3.1. Key synthesis steps for each of the four  $^{18}\text{F}$ -labeled tracers are demonstrated and characterized with the chip: concentration of fluoride ion, solvent exchange, and chemical reactions. The obtained fluorination efficiencies of 90-95% are comparable to, or greater than, those achieved by conventional approaches.

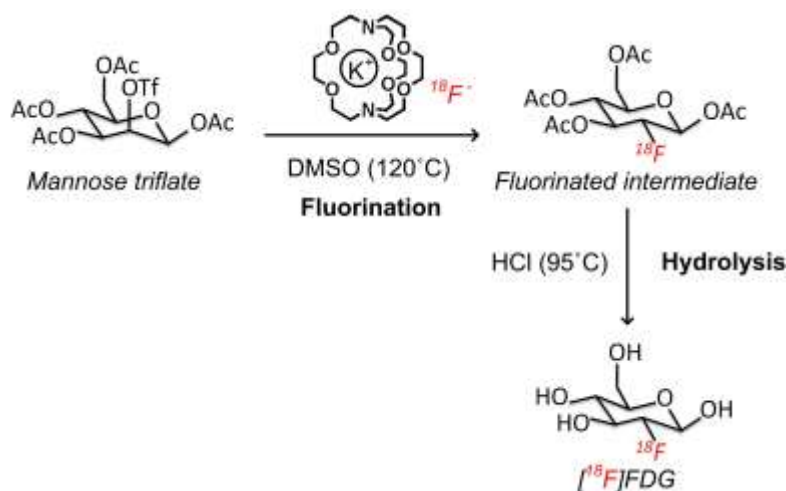


Figure 3.1(A): Synthesis scheme for two-step synthesis of [ $^{18}\text{F}$ ]FDG.

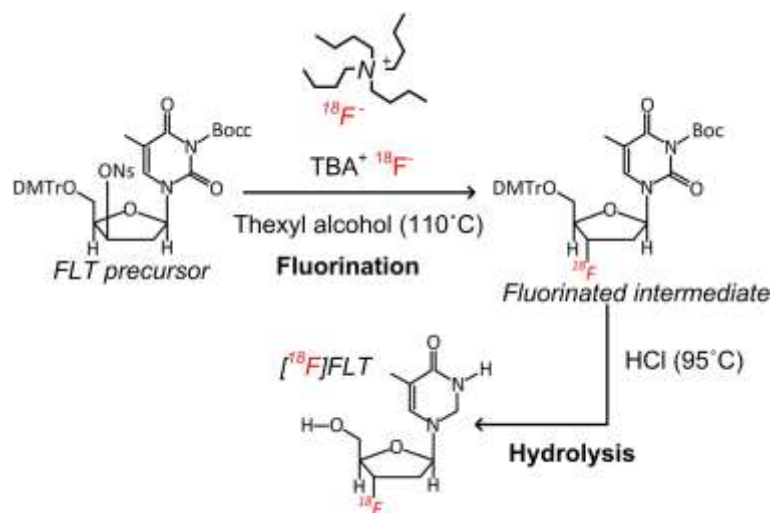


Figure 3.1(B): Synthesis scheme for two-step synthesis of  $[^{18}\text{F}]\text{FLT}$ .

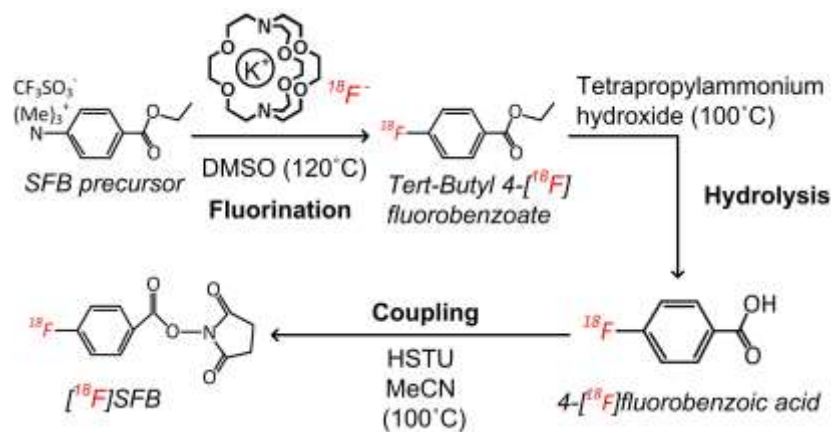


Figure 3.1(C): Synthesis scheme for three-step synthesis of  $[^{18}\text{F}]\text{SFB}$ .

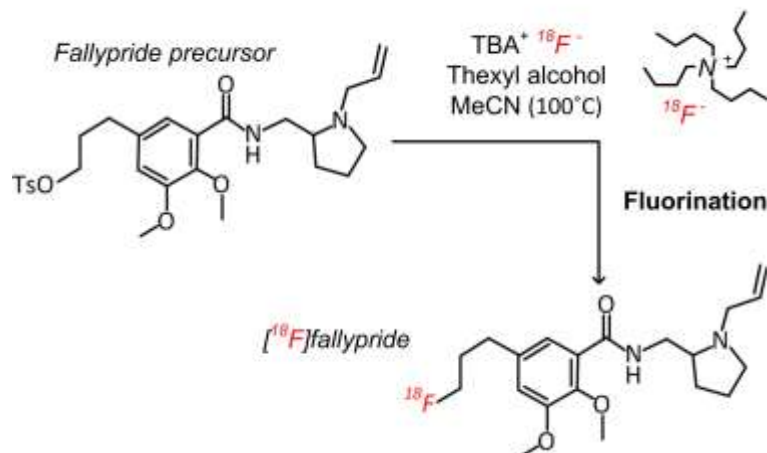


Figure 3.1(D): Synthesis scheme for single-step synthesis of  $[^{18}\text{F}]$ fallypride.

### 3.2 Radiotracers produced by EWOD radiosynthesizer

#### 3.2.1 $[^{18}\text{F}]$ FDG

In  $[^{18}\text{F}]$ FDG, fluorine-18 is substituted for the hydroxyl group on Carbon-2 of a glucose molecule, a location where fluorine does not affect the molecule's ability to undergo phosphorylation by hexokinase or facilitated transport across the blood-brain barrier [80]. Because removal of the Carbon-2 hydroxyl group interferes with function of the enzyme glucose-6-phosphate isomerase in the second step of glycolysis, the phosphorylated (by hexokinase) product of  $[^{18}\text{F}]$ FDG is intracellularly trapped at the site of metabolism and provides a record of metabolic activity that can be imaged by PET.

$[^{18}\text{F}]$ FDG was originally developed for mapping brain glucose metabolism *in vivo* [81], but because abnormal glucose metabolism is implicated with a variety of diseases,  $[^{18}\text{F}]$ FDG has since been used for many other applications such as oncologic, neurological, and cardiovascular

imaging [82]. [ $^{18}\text{F}$ ]FDG is now the most widely used PET tracer and it is currently in use at many imaging centers as an “off-the-shelf” radiopharmaceutical [83].

However, [ $^{18}\text{F}$ ]FDG is not target-specific, which can lead to false positives due to unrelated natural causes of increased glucose uptake and glycolysis like inflammation and muscle activity [84]. Another issue is that [ $^{18}\text{F}$ ]FDG has high background in areas such as the heart, brain, and the vicinity of the bladder.

### 3.2.2 [ $^{18}\text{F}$ ]FLT

[ $^{18}\text{F}$ ]FLT is an analogue of the DNA nucleoside thymidine, in which a hydroxyl group has been replaced with [ $^{18}\text{F}$ ]fluoride [85]. Substitution at the 3' site prevents further incorporation of [ $^{18}\text{F}$ ]FLT into replicating DNA. Like thymidine uptake, [ $^{18}\text{F}$ ]FLT uptake increases during the S phase (DNA synthetic phase) of the cell cycle. After entering cells, [ $^{18}\text{F}$ ]FLT is phosphorylated by thymidine kinase 1 into a more polarized molecule that cannot freely exit cells. Therefore, retention of [ $^{18}\text{F}$ ]FLT within the cell is a measure of thymidine kinase 1 activity, an enzyme that is closely correlated to cellular proliferation. For that reason, PET imaging with [ $^{18}\text{F}$ ]FLT has been used as a measure for cellular proliferation either in normally proliferating tissues or in abnormally growing tumors [86].

[ $^{18}\text{F}$ ]FLT may be particularly useful as an early indicator of success of tumor therapy, instead of relying on identifying an alteration in growth reflected by tumor size (which may take weeks or months to detect) [85]. It is in many cases a more specific hallmark of malignant tumors than [ $^{18}\text{F}$ ]FDG. However, [ $^{18}\text{F}$ ]FLT has high uptake in the liver and proliferating tissue like bone marrow [87], which can limit use of [ $^{18}\text{F}$ ]FLT for cancer staging near those regions of

the body. Although several studies have demonstrated successful use of [ $^{18}\text{F}$ ]FLT for cancer detection, it does not appear likely to replace [ $^{18}\text{F}$ ]FDG for most tumor types, because [ $^{18}\text{F}$ ]FLT generally has a lower uptake than [ $^{18}\text{F}$ ]FDG in most solid tumors [86]. Also, not all tumors with high proliferation have a high uptake of [ $^{18}\text{F}$ ]FLT.

### 3.2.3 [ $^{18}\text{F}$ ]SFB

[ $^{18}\text{F}$ ]SFB is an amine-reactive fluorine-18 labelled prosthetic group and acylation agent [88]. It is useful for radiolabelling peptides, proteins, and antibodies without exposing them to harsh reaction conditions, such as temperatures above 100°C and aprotic water-free solvents [8]. [ $^{18}\text{F}$ ]SFB can be labelled onto most bioactive peptides, which exhibit an N-terminal amino group (most commonly at lysine side chains) available for acylation [89].

It has been used to radiolabel a wide variety of biomolecules, including albumin, transferrin, monoclonal antibodies, bombesin, insulin, annexin-V, and arginine-glycine-aspartic acid (RGD) peptides [89, 90]. Although a large number of  $^{18}\text{F}$ -labelled prosthetic groups have been developed to attach to biomolecules through a wide range of methods (i.e., acylation, amidation, imidation, alkylation reactions, photochemical conjugation, and solid-phase synthesis), the acylation approach using [ $^{18}\text{F}$ ]SFB remains one of the most versatile and commonly used because of its *in vivo* stability and radiochemical yield [91].

Radiolabelled prosthetic groups can be coupled to biomolecules under mild conditions and preserve integrity of labelled peptides (even those that are heat or pH sensitive) [92]. However, preparation of radiolabelled prosthetic groups such as [ $^{18}\text{F}$ ]SFB often involves a time-consuming multi-step synthetic procedure. Other radiolabelled prosthetic groups with shorter

synthesis procedures have recently been developed, such as *N*-succinimidyl 4- $^{18}\text{F}$ -fluoromethyl-benzoate ( $^{18}\text{F}$ SFMB) and *N*-Succinimidyl 3-(di-*tert*-butyl $^{18}\text{F}$ fluorosilyl) benzoate ( $^{18}\text{F}$ SiFB) [89, 92], but have not yet gained wide acceptance. Furthermore, quicker synthesis time of  $^{18}\text{F}$ SFB has been demonstrated using microfluidic radiosynthesizers [93].

### 3.2.4 $^{18}\text{F}$ fallypride

$^{18}\text{F}$ fallypride is a fluorinated and substituted benzamide with high affinity for D2 and D3 dopamine receptors [94]. It is particularly useful for visualization of D2/D3 receptors in extrastriatal areas, which are considered to be important in neuroleptic drug interactions, reward mechanisms, cognitive processing, addiction, schizophrenia, emotion, Alzheimer's disease, Parkinson's disease, attention deficit hyperactivity disorder, and other attributes of human behavior [95]. Use of PET with  $^{18}\text{F}$ fallypride can determine concentration of D2/D3 receptors, occupancy of D2/D3 receptors, sensitivity of dopamine release (measured by competitive binding) to pharmacological or behavioral changes, and response to various neuroleptic drugs that can inhibit D2 receptors by causing increased secretion of prolactin [95, 96].

Relative to radiotracers that are trapped within cells through enzyme-mediated interactions,  $^{18}\text{F}$ fallypride requires 100 to 1000 times greater specific activity for PET imaging to avoid appreciable occupancy of D2/D3 receptors, which are saturable binding sites [16, 36, 97]. For preclinical imaging of small animals, the specific activity requirements may be even higher to perform PET imaging without inducing changes in physiology, such as dyskinesia (which is observed when more than 50% of D2/D3 receptors are saturated) [97].

### 3.3 Radiolabelling chemistry steps on EWOD device

#### 3.3.1 Reagents, materials, and analytical methods

No-carrier-added [ $^{18}\text{F}$ ]fluoride ion was obtained by irradiation of 97% [ $^{18}\text{O}$ ]-enriched water with an 11 MeV proton beam using a cyclotron (RDS-112, Siemens, Knoxville, TN) at the UCLA Ahmanson Biomedical Cyclotron Facility. Potassium carbonate ( $\text{K}_2\text{CO}_3$ , 99%), 2,3-dimethyl-2-butanol (hexyl alcohol), anhydrous acetonitrile (MeCN, 99.8%), anhydrous dimethyl sulfoxide (DMSO, 99.9%), anhydrous methanol (MeOH, 99.8%), and and *N,N,N',N'*-tetramethyl-*O*-(*N*-succinimidyl)uronium hexafluorophosphate (HSTU, 98%) were purchased from Sigma Aldrich. Hydrochloric acid (HCl, 1 N) and sodium hydroxide (NaOH, 1 N) were purchased from Fisher Scientific. Mannose triflate (FDG precursor), 4,7,13,16,21,24-hexaoxa-1,10-diazobicyclo (8.8.8)-hexacosane ( $\text{K}_{2.2.2}$ , 98%), tetrabutylammonium bicarbonate solution (75 mM) ( $\text{TBAHCO}_3$ ), 3-*N*-Boc-5'-*O*-dimethoxytrityl-3'-*O*-nosyl-thymidine (FLT precursor), 4-(tert-butoxycarbonyl)-trimethylbenzeneammonium triflate (SFB precursor), and tosyl-fallypride (fallypride precursor) were purchased from ABX Advanced Biochemical Compounds (Radeberg, Germany). All chemicals were used as received. A vortex mixer (Vortex Genie 2, Scientific Industries) was used for off-chip preparation of reagents.

Neutral alumina (50-300  $\mu\text{m}$  particle size), C-18 resin (55-105  $\mu\text{m}$  particle size), and hydrophilic-lipophilic-balanced resin were purchased from Waters (Milford, MA). Ion retardation resin (AG11 A8, 180-425  $\mu\text{m}$  particle size) and cation exchange resin (AG-50W-X4, 63-150  $\mu\text{m}$  particle size) were purchased from BioRad Laboratories (Hercules, CA).

Radioactivity was measured from samples using a calibrated ion chamber (Capintec CRC-15R). Radio thin-layer chromatography (radio-TLC) was analyzed with a scanner equipped

with scintillation probe for gamma rays (MiniGITA star, Raytest). High performance liquid chromatography (HPLC) was carried out on a reversed-phase C-18 column (250 x 4.6 mm, 5  $\mu$ m, Phenomenex Luna) equipped with a variable wavelength UV detector and a radiation detector (Eckert&Ziegler).

Radioactivity was also quantified using Cerenkov imaging, as described by Dooraghi et al. [98], in the cases when it was important to determine its position on chip. Cerenkov radiation is light that is produced when a beta particle travels faster than the speed at which light travels in the surrounding medium. Because the EWOD chip gap (140  $\mu$ m) is less than the average positron range (1.0 mm in water) most of the beta particles emitted by fluorine-18 are expected to travel through the transparent glass substrate (each plate is 0.7 mm thick), through which they can travel at a faster speed than light would travel in the glass. The emitted Cerenkov radiation is in the UV and visual spectrum and can be detected by a sensitive camera. With use of a scientific cooled camera in a light tight enclosure, Cerenkov imaging can both localize and quantify the on-chip radioactivity *in situ*. Radioactivity within a region of interest was quantified from image intensity using calibration and correction factors with MATLAB as described in previous work [98].

The Cerenkov setup is housed in a light-tight box with a hinged lid that can close over a gasket (Fig. 3.2). The chip was connected to electrical connections placed in the bottom of the box. A mirror was held on a motorized rotation stage above the chip to direct light into one of two cameras. One camera (DFK 21AU04, Imaging Source, Charlotte, NC) was used for standard visible imaging to remotely monitor the on chip processes. The second camera (QSI 540, Quantum Scientific Imaging, Poplarville, MS) was more sensitive and used for imaging



Cerenkov radiation. Electrical connections were fed into the box through a tube to minimize interference from exterior light.

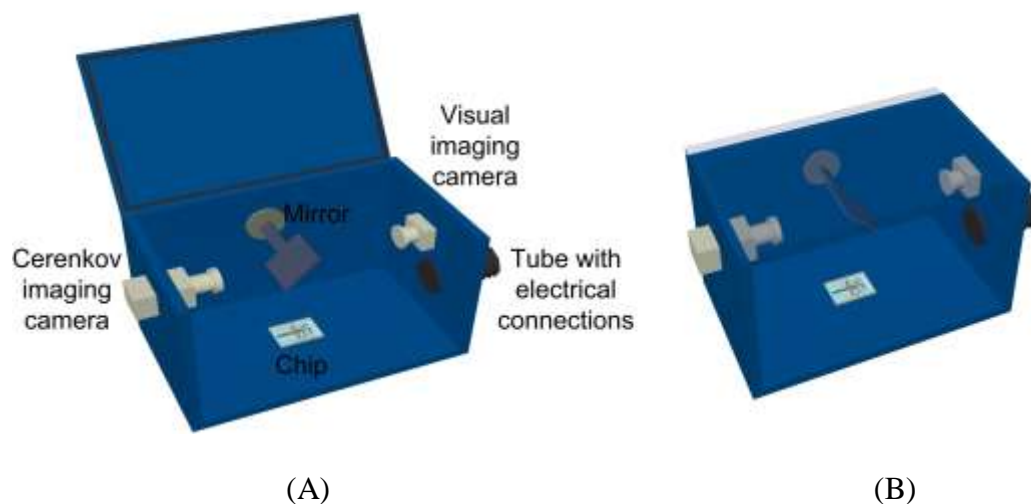


Figure 3.2: The Cerenkov imaging setup presented here is the same used by Dooraghi et al. [98]. (A) During regular EWOD operation, the lid was open and the mirror reflected the chip image towards the visual imaging camera. (B) To image the on chip radioactivity, the lid was manually closed and the motorized stage directed the mirror towards the Cerenkov imaging camera.

### 3.3.2 Fluoride concentration

[ $^{18}\text{F}$ ]fluoride is delivered in [ $^{18}\text{O}$ ]-enriched water from the cyclotron and is mixed with base and phase transfer catalyst. In earlier reports of using EWOD for radiosynthesis [60, 99], the mixing was done off chip with a vortex mixer prior to loading onto the EWOD chip. For

[<sup>18</sup>F]FDG and [<sup>18</sup>F]SFB radiolabelling in this chapter, mixing was instead performed on chip by EWOD actuation after loading solutions of base and phase transfer catalyst separate from [<sup>18</sup>F]fluoride onto the chip. After being loaded onto the electrical ground plate edge by using a micropipette, 2-10  $\mu$ L droplets were pulled between the plates and moved to the circular multifunctional electrode site by EWOD actuation. The loading process was repeated until the desired volume was reached, upon which the mixed droplet was heated at 105°C to dry.

The amount of radioactivity loaded was initially restricted by the droplet volume that could be squeezed within the 140  $\mu$ m gap over the 12 mm diameter heater site, limiting us to a maximum volume of 16  $\mu$ L fluoride solution that could be reduced by evaporation and a radioactivity of 16 mCi after typical cyclotron bombardment from the UCLA Ahmanson Biomedical Cyclotron Facility [99]. The necessary radioactivity for PET imaging depends on patient size and type of radiotracer. Human doses may require 10 mCi but mice doses can be as low as 200  $\mu$ Ci [5]. More radioactivity can be used on the EWOD device by repeated loading and heating steps, but this lengthens the synthesis time. Further development allowed us to concentrate larger volumes by not squeezing the initial droplet between the plates (*i.e.*, into a disk shape) but instead loading and heating a much larger droplet on the open surface of the bottom plate (*i.e.*, in a spherical shape) adjacent the edge of the top electrical ground plate, as shown in Fig. 3.3A. Compared to a closed method (with squeezed droplets) for concentration, the open method allowed a larger droplet to be loaded for a defined area on the device surface and enabled quicker evaporation of the solvent. Here, a 200  $\mu$ L droplet of fluoride with base and phase transfer catalyst could be heated outside of the gap and then pulled between the gap by EWOD after its volume reduced to 5  $\mu$ L (Fig. 3.3C). Within the gap, the droplet could shrink

more or be completely dried with further heating (Fig. 3.3D). The total heating time was 12 minutes, but the 10 minutes outside of the cover plate could potentially be reduced with the addition of a heater outside of the cover plate, specifically for concentration.

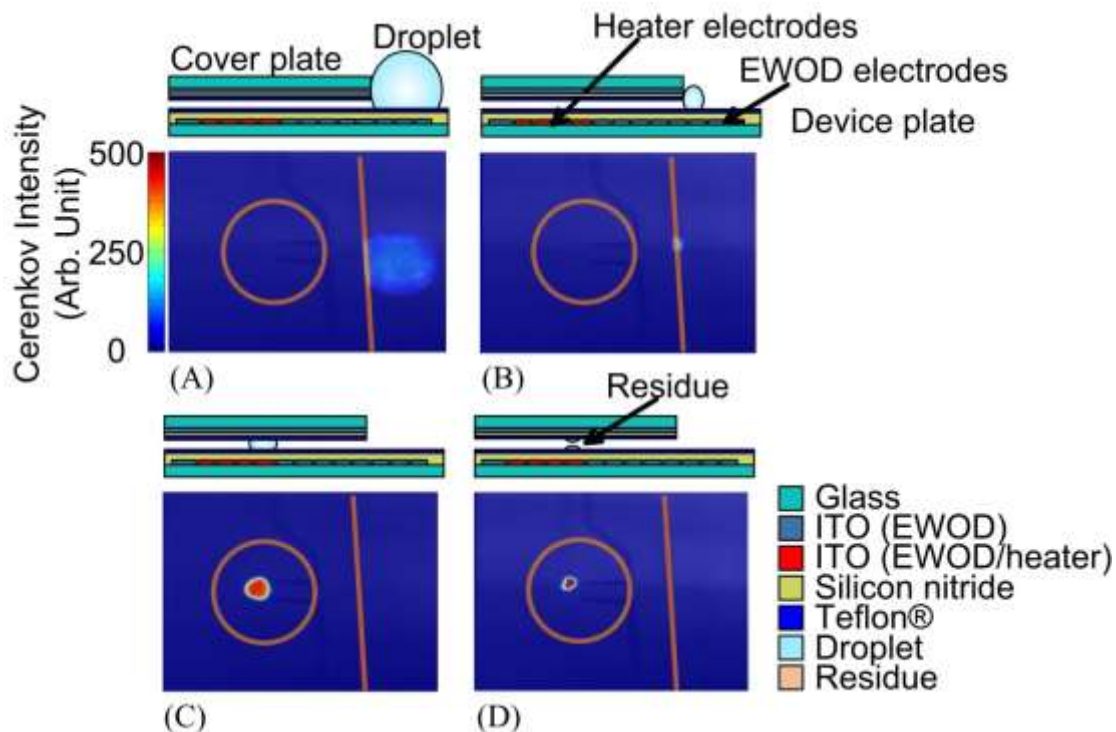


Figure 3.3: Images of Cerenkov radiation emitted during fluorine-18 positron decay during fluoride concentration and cross-section schematics of the chip in corresponding stages. In the Cerenkov images, red represents a higher concentration of radioactivity. Orange lines and circles were added to depict the cover plate edge and the heating site, respectively. (A) 200  $\mu\text{L}$  droplet of [ $^{18}\text{F}$ ]fluoride with base and phase transfer catalyst loaded to the cover plate edge (depicted with an orange line). (B) Droplet at cover plate edge after its volume was reduced by heating the nearby multifunctional electrodes to 150°C. (C) Droplet at center of heater after EWOD actuation. (D) Residue at the heater center after solvent evaporation.

Calibrated ion chamber measurements before and after concentration showed that negligible radioactivity was lost during the whole process. This method of removing bulk water for radiotracer synthesis is different from the conventional method, in which [ $^{18}\text{F}$ ]fluoride is typically trapped on a cartridge of anion exchange resin and then eluted off in a release solution [100]. The concentration can both reduce evaporation time (if the release solution contains less water) and also remove impurities that are released by the cyclotron target. However, the ability to concentrate fluoride ion directly on the EWOD chip without using anion exchange resin provides an alternative means of preparing radiotracers with high specific activity. Such a method avoids the introduction of high fluorine-19 carrier concentration (which can diminish specific activity) when the fluorine-18 solution was first concentrated with anion exchange resin [36].

### **3.3.3 Solvent exchange and azeotropic drying**

Because of its open-to-air configuration, the EWOD chip facilitates evaporative removal of solvent, unlike many other types of microfluidic devices [32]. Solvent exchange is performed on the EWOD chip by heating until the solvent has been evaporated and its vapors removed with a nitrogen stream, leaving behind a solute residue at the heater region. A droplet of the new solvent is loaded at the cover plate edge, and then EWOD actuation is used to pull the droplet in between the plates, move it to the residue site, and dissolve the residue.

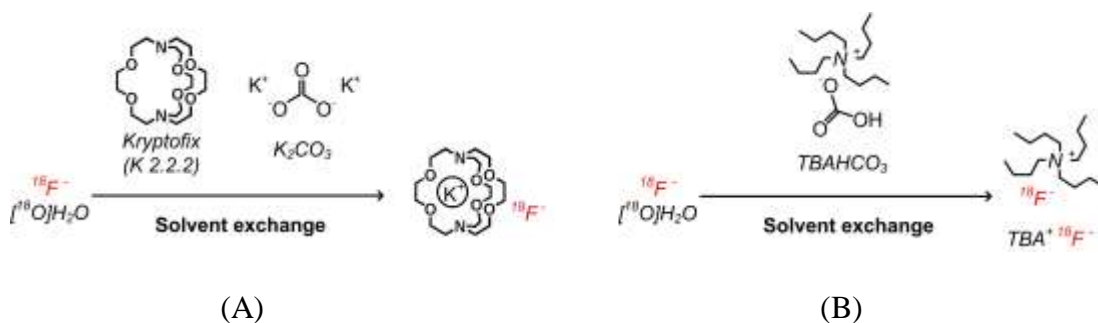


Figure 3.4: Solvent exchange of fluoride with phase transfer catalyst. (A) Potassium carbonate and Kryptofix were used in radiosynthesis for [<sup>18</sup>F]FDG and [<sup>18</sup>F]SFB. (B) Tetrabutylammonium bicarbonate was used in radiosynthesis of [<sup>18</sup>F]FLT and [<sup>18</sup>F]fallypride.

For azeotropic drying, MeCN is added at the electrical ground plate edge, moved to the reactor site by electrowetting, mixed, and heated at 105°C for 1 minute. Due to the properties of the water-MeCN azeotrope, this is an effective method for removing residual water. Typically, fluorine-18 radiochemistry processes using a macroscale synthesizer include 2-3 successive cycles of azeotropic evaporation with MeCN to obtain the naked [<sup>18</sup>F]fluoride ion for the subsequent fluorination reaction [8]. Multiple azeotropic evaporations were also used in the preliminary devices [60, 99] as well as our early work [57, 101]. However, in the current microfluidic droplet synthesis, no significant improvements in reaction yields were found when increasing the number of azeotropic drying steps on the EWOD chip. Thus, only one azeotropic drying step was used, reducing the overall synthesis time and therefore radioactive decay. Both dose calibrator measurements and Cerenkov imaging indicated negligible loss during the azeotropic drying process [98].

### 3.3.4 Fluorination and other reactions

Fluorination was realized on the EWOD chip by first loading a precursor solution. After electrowetting pulled the precursor droplet from the electrical ground plate edge and moved it to the dried fluoride, the droplet was mixed by applying EWOD actuation potential to the heater electrodes for a back and forth motion across the solid residue. In Cerenkov imaging studies for [<sup>18</sup>F]FDG synthesis, a relatively homogenous distribution of radioactivity was achieved after 30 seconds of EWOD-actuated mixing [98]. The heating site was then heated to 105-120°C for 2-6 minutes depending on the type of radiotracer. For [<sup>18</sup>F]FDG, the 10 minute fluorination time used before [60] was reduced to 5 minutes without a noticeable change in reaction yield.

Conventionally, nucleophilic radiofluorination reactions use MeCN as a solvent because its low boiling point (82°C) facilitates rapid removal by evaporation after the synthesis. Although many nucleophilic fluorination reactions have been reported to be more efficient in DMSO due to its high polarizability and ability to perform reactions at higher temperatures [102], DMSO is not typically used in macroscale synthesis because its low volatility (189°C boiling point) makes its evaporative removal difficult in a short time. However, microliter volumes of DMSO could be effectively evaporated at 120°C in the EWOD chip after fluorination. The remaining DMSO did not affect following reactions in the synthesis, and the residual amount (870 ppm) after synthesis, cartridge purification, and formulation (which further diluted the product) was below the acceptable limits for human use (5000 ppm) [60].

Ideally, fluorine incorporation is the last synthesis step for radiotracer preparation in order to minimize the overall synthesis time and thus minimize the amount of radioactivity decay and reduce radiation exposure to the operator. A synthesis process with fewer steps is also

inherently more reliable and simpler to automate. However, due to the high basicity of the “naked” fluoride ion, the majority of complex molecules require additional synthesis steps after fluorination, such as: removal of protecting groups (by acidic or alkaline hydrolysis), saponification, esterification, and coupling reactions.

To accomplish multistep reactions in the EWOD chip, the reagents were loaded from the electrical ground plate edge and mixed with the previous reaction’s products by electrowetting. The multifunctional electrodes were then heated to the set reaction temperature over a predetermined reaction time. All of the synthesis reactions were performed at the same heating site without any intermediate purification steps.

Although efforts were made to maximize individual isolated pathways for loading reagents, the synthesis results were not affected in tests where the same route was used for all reagents. This was the case, even if a reagent was water sensitive and followed the same path as an aqueous reagent. Contamination from adsorption was not an issue, because all of the radiotracer processes demonstrated involved a one-pot synthesis and only one reactor site was used on chip. Also, there was very limited radioactive residue on the chip during droplet routing based on previous work using Cerenkov imaging for analysis [98]. However, residue became significant on the reactor site after heating.

### **3.4 Off chip purification and evaluation**

#### **3.4.1 Extraction (i.e. Collection)**

The final reaction mixture from the EWOD chip was manually extracted by pipette after removing the electrical ground plate and washing both plates with solvent (*i.e.*, MeCN, DMSO,

MeOH, H<sub>2</sub>O). Radioactivities of the [<sup>18</sup>F]fluoride complex solution before and after loading, the total EWOD chip after the synthesis, the extracted product, actuation plate, electrical ground plate, and pipette tips were measured with a calibrated ion chamber. The extraction efficiency was determined by dividing the radioactivity of the crude product droplet after extraction by the post-synthesis radioactivity of the total EWOD chip before extraction.

An automated approach for extraction was also tested in which the crude product droplets were moved away from the reactor after synthesis reactions to an outlet droplet pathway by EWOD actuation, and then pulled off chip into a vial by vacuum. An additional 3-6 μL solvent was required to move the product droplets away from the heating site [<sup>18</sup>F]FLT (74% extraction efficiency with addition of 3 μL MeCN) and [<sup>18</sup>F]fallypride (87% extraction efficiency with addition of 6 μL MeOH), but no additional solvent was required for [<sup>18</sup>F]SFB (95% extraction efficiency).

### 3.4.2 Purification and analysis

The crude reaction mixtures were purified off chip to isolate the desired radiotracers from unreacted reagents, intermediates, and by-products, which are not safe to be administered into animals and patients, and can complicate interpretation of images if the by-products are radioactive. Two different purification methods were used depending on the type of radiotracer.

[<sup>18</sup>F]FDG and [<sup>18</sup>F]FLT were purified *via* a solid-phase extraction (SPE) method using miniaturized cartridges prepared in-house. Each cartridge contained 4 types of SPE sorbents. For [<sup>18</sup>F]FDG purification, neutral alumina, ion retardation, cation exchange, and C-18 sorbents removed impurities as the crude radiotracer mixture was pushed into the cartridge and the



purified radiotracer was collected at the output. For [ $^{18}\text{F}$ ]FLT purification, neutral alumina, ion retardation, and cation exchange sorbents were also used, but C-18 was replaced with hydrophilic-lipophilic-balanced resins to retain [ $^{18}\text{F}$ ]FLT as impurities from the crude radiotracer passed through the cartridge into waste. The desired [ $^{18}\text{F}$ ]FLT radiotracer was subsequently eluted from the cartridge as a purified product in ethanol.

HPLC was used to purify [ $^{18}\text{F}$ ]SFB and [ $^{18}\text{F}$ ]fallypride as the final radiotracer and other impurities were difficult to be purified *via* solid-phase extraction cartridges. Due to the small quantities of reagents used, the mass of impurities is much lower from the EWOD chip than conventional systems, and thus an analytical-scale HPLC column was sufficient for preparative use. A separate analytical HPLC system was used to test the chemical and radiochemical purity for all of the synthesized radiotracers after purification.

Radio-TLC was used to analyze the reaction efficiencies after crude reaction mixtures were spotted onto silica gel plates and developed in appropriate mobile phases. Multiple radioactivity peaks were visible in each TLC chromatogram, one corresponding to the desired reaction product and the other(s) to unreacted starting material and/or byproducts. The reaction efficiency was determined from the area under the product peak divided by the total area under all peaks. For radiotracer synthesis processes requiring multiple reactions, the combined reaction efficiency was the multiplied product of all the individual reaction efficiencies. Radio-TLC was also used to measure radiochemical purity of the purified product.

While we used fluorination efficiency and hydrolysis efficiency to characterize radiotracer synthesis for the preliminary results [57, 101], we have now demonstrated the entire PET probe production process starting from synthesis, and including purification and

reformulation. Here we report the final decay-corrected radiochemical yield obtained after the purification and reformulation in saline. The final radiochemical yield was determined by comparing the decay-corrected radioactivity of the purified product with the initial fluoride radioactivity loaded onto the chip for synthesis.


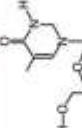
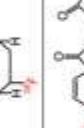

### 3.5 Radiotracer synthesis yield

Upon setting the main reaction parameters of reagent, concentration, temperature, and time, the reaction efficiencies for each radiotracer synthesis process were reliable and generally high (Table 3.1).

The four example tracers demonstrated here include both aliphatic nucleophilic fluorination reactions as well as aromatic nucleophilic fluorination, which generally require harsher reaction conditions. Compared with preliminary results [57, 101], the fluorination efficiency has improved to 90% or greater for all four tracers. Purified radiochemical yield for all four tracers is presented in the right-most column of Table 3.1.

As summarized in the 6th column of Table 3.1., the combined reaction efficiency (decay corrected) was  $93\% \pm 3\%$  (n=2) for [ $^{18}\text{F}$ ]FDG,  $95\% \pm 3\%$  (n=6) for FLT,  $85\% \pm 5\%$  (n=3) for [ $^{18}\text{F}$ ]SFB, and  $90\% \pm 9\%$  (n=6) for [ $^{18}\text{F}$ ]fallypride. These reaction efficiencies were comparable to or exceeded macroscale methods and represent the yield before extraction and purification

Table 3.1: Four diverse radiotracers synthesized using the same EWOD chip design

Tracer	Molecule	Application	Radiopharmacy availability	Fluorination efficiency <sup>1</sup>	Combined reaction efficiency <sup>1</sup>	Extraction efficiency <sup>1</sup>	Before-purification yield <sup>1,2</sup>	Synthesis Time <sup>3</sup>	Radiochemical Yield <sup>1</sup>
<sup>18</sup> F]fluoro-2-deoxy-D-glucose ( <sup>18</sup> F]FDG)		Sugar metabolism	Yes	93% ± 3% (n=2)	93% ± 3% (n=2)	63% ± 8% (n=2)	45% ± 10% (n=2)	50 ± 3 min (n=2)	37 ± 13% (n=2)
3'-deoxy-3'-[ <sup>18</sup> F]fluorothymidine ( <sup>18</sup> F]FLT)		DNA proliferation	Limited	95% ± 3% (n=6)	95% ± 3% (n=6)	81% ± 5% (n=6)	74% ± 7% (n=6)	40 ± 4 min (n=6)	56% ± 8% (n=6)
4-[ <sup>18</sup> F]fluorobenzoate ( <sup>18</sup> F]SFB)		Protein labeling	No	90% ± 6% (n=5)	85% ± 5% (n=3)	80% ± 17% (n=3)	34% ± 10% (n=3)	58 ± 8 min (n=3)	19% ± 8% (n=5)
[ <sup>18</sup> F]fallypride		Neuro-transmitter binding	No	90% ± 9% (n=6)	90% ± 9% (n=6)	94% ± 3% (n=6)	84% ± 7% (n=6)	31 ± 1 min (n=6)	65% ± 11% (n=6)

<sup>1</sup> All reported efficiencies and yields have been corrected for radioactive decay. <sup>2</sup> Before-purification yield was the extracted radioactivity multiplied by the combined reaction efficiency and divided by the loaded radioactivity. <sup>3</sup> Synthesis time was from start of loading to end of extraction.

Extraction efficiency varied with each radiotracer's synthesis: 63% ± 8% (n=2) for [<sup>18</sup>F]FDG, 81% ± 5% (n=6) for [<sup>18</sup>F]FLT, 80% ± 17% (n=3) for [<sup>18</sup>F]SFB, and 94% ± 3% (n=6)

for [ $^{18}\text{F}$ ]fallypride. Extraction efficiency of [ $^{18}\text{F}$ ]FDG was low during development of hydrophobic coating steps, but has been observed at 80% with Teflon® 2400 baked above 330°C in vacuum. Although the extraction efficiency was comparable with other microfluidic synthesizers, it was poor compared to macroscale synthesizers where extraction efficiency is typically greater than 95%. During the extraction step, 0-3% of the radioactivity was lost to the pipette tip. The remaining radioactivity was left on the actuation and cover plates, suggesting adsorption of fluoride onto the surface or fouling of Teflon® with  $^{18}\text{F}$ -labelled species.

Before-purification yields were determined by multiplying combined reaction efficiency by measured extraction radioactivity and dividing it by the initially loaded radioactivity. Compared with the before-purification yields presented in earlier work (50% for [ $^{18}\text{F}$ ]FLT and 72% for [ $^{18}\text{F}$ ]fallypride) [101], the current before-purification yields (73% for [ $^{18}\text{F}$ ]FLT and 84% for [ $^{18}\text{F}$ ]fallypride) have improved by 45% for [ $^{18}\text{F}$ ]FLT and 16% for [ $^{18}\text{F}$ ]fallypride.

The EWOD chip can use different solvents and shorter reaction times than conventional synthesizers, but because it is open to air, care must be taken to not lose radioactivity as volatile side products and intermediates. Evaporated reagents could condense in regions on chip that were closer to ambient temperature and had weak gas flow (such as on the opposite side of the reactor from where the source of a nitrogen stream was placed). Condensation that developed during [ $^{18}\text{F}$ ]FDG fluorination, was determined by Cerenkov imaging to have radioactivity levels at 5-14% of the total radioactivity, and radio-TLC analysis showed that the condensate radioactivity consisted mostly of unreacted [ $^{18}\text{F}$ ]fluoride (68%) with the remainder labelled onto the fluorinated intermediate [98]. However, the condensate could also be collected and merged into the main reaction droplet using EWOD during the fluorination reaction step. Improved

reaction yields (from 50% to 72%) suggested that some of the collected unreacted [ $^{18}\text{F}$ ]fluoride underwent the fluorination reaction after remerging with the main droplet [98].

Also because the reactor was not sealed, the droplet size reduced during heating, even if the temperature was below the boiling point. Attempts were made to keep a stable concentration by replenishing the volume with smaller solvent droplets. However, we found that reliably high reaction yields could be achieved with a simpler method of allowing droplet size to reduce, which resulted in an overall increase in the concentration of the reagents [58, 60].

Although reaction times are typically shorter when performed with microfluidic volumes [8], the overall radiotracer synthesis time (from initial loading to extraction) on the EWOD device was longer than desired and ranged from  $31 \pm 1$  min for [ $^{18}\text{F}$ ]fallypride (n=6) to  $58 \pm 8$  min for [ $^{18}\text{F}$ ]SFB (n=3). EWOD radiosynthesizer reaction times varied from 5 to 7 minutes (within a comparable range to other microfluidic radiosynthesizers) and heating for solvent exchange could be completed within 3 minutes, but the overall synthesis times were relatively long due to tedious process of manual reagent loading and manual activation of electrodes. The overall synthesis time is anticipated to be reduced with integrated reagent delivery and further automation in electrowetting and heating control [103].

### **3.6 Quality control and use of radiotracers**

#### **3.6.1 Quality control and imaging of [ $^{18}\text{F}$ ]FDG**

[ $^{18}\text{F}$ ]FDG produced by the EWOD radiosynthesizer was purified in a custom-made miniaturized cartridge consisting of a 750  $\mu\text{m}$  perfluoroalkoxy tubing packed with cation exchange resin (5 mg AG-50W-X4, BioRad Laboratories), ion retardation resin (5 mg, AG11 A8,

BioRad Laboratories), neutral alumina (30 mg, 50-300  $\mu\text{m}$  particle size, Waters), and C-18 functionalized beads (20 mg, 55-105  $\mu\text{m}$  particle size, Waters) [60]. The solid phase extraction sorbents were sandwiched between two polyethylene frits (20  $\mu\text{m}$  pore size). The cartridge was first conditioned with ethanol (0.5 mL) and then water (1 mL, 18 M $\Omega$ ). Crude product was injected into the cartridge, which neutralized acid (using cation exchange resin), removed ionic species (with ion retardation resin), retained unreacted [ $^{18}\text{F}$ ]fluoride ion (using neutral alumina), and removed other organic impurities (using C-18 functionalized beads). The final product was eluted with 0.25 mL water to achieve 99% chemically pure [ $^{18}\text{F}$ ]FDG. The purified [ $^{18}\text{F}$ ]FDG was analyzed by radio-HPLC with isocratic elution of MeCN/H $_2$ O 70:30 (vol/vol) at a flow rate of 1 mL/min to determine radiochemical purity. No radiochemical impurities were detected by radio-TLC or radio-HPLC after purification (Fig. 3.5) [60].

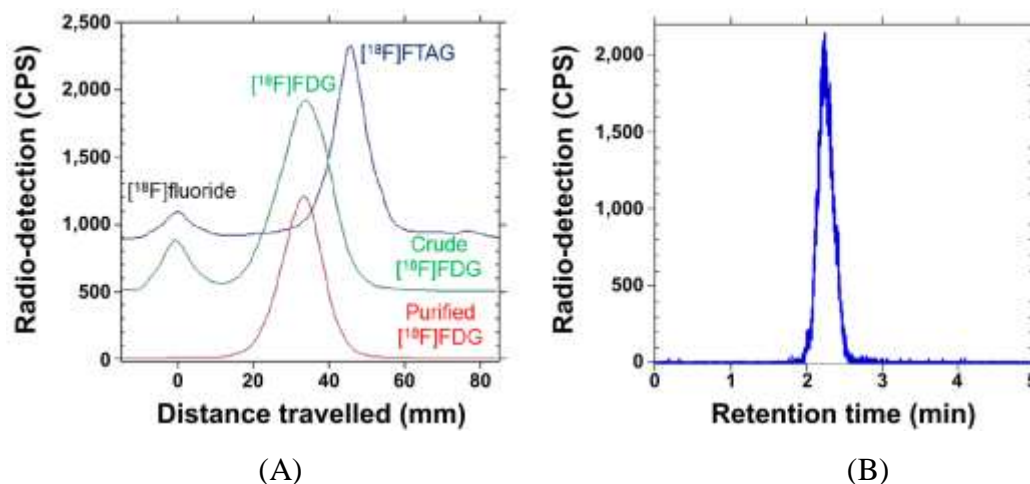
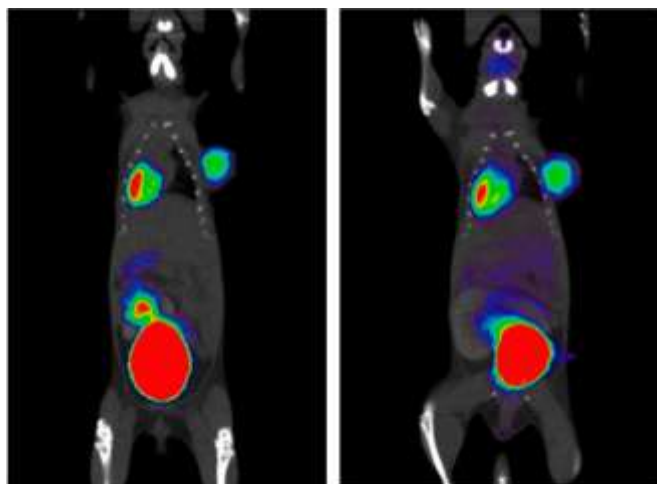


Fig 3.5: (A) Representative radio-TLC of crude [ $^{18}\text{F}$ ]FTAG (blue trace), crude [ $^{18}\text{F}$ ]FDG (green trace), and purified [ $^{18}\text{F}$ ]FDG (red trace). (B) Representative radio-HPLC chromatogram of purified [ $^{18}\text{F}$ ]FDG [60].

The amount of residual Kryptofix in the final [ $^{18}\text{F}$ ]FDG product was quantified with a colorimetric Kryptofix test, in which a TLC plate is stained with potassium permanganate solution to visualize oxidized Kryptofix (that appears as a yellow spot) [104]. In tests of EWOD produced [ $^{18}\text{F}$ ]FDG, the [ $^{18}\text{F}$ ]FDG sample spot was less intense compared to spots from standard Kryptofix solutions at 4  $\mu\text{g/mL}$  and 40  $\mu\text{g/mL}$ , which semiquantitatively confirmed the concentration of the final [ $^{18}\text{F}$ ]FDG sample is below the allowable level (50  $\mu\text{g/mL}$ ) determined by the United States Pharmacopeia (USP) [60]. Gas chromatography for residual solvent analysis showed that the [ $^{18}\text{F}$ ]FDG product contained 870 ppm of DMSO (5,000 ppm USP allowable limit), 115 ppm of ethanol (5,000 ppm USP allowable limit), and undetectable levels (<20 ppm) of acetonitrile (400 ppm USP allowable limit) [60].

The quality of [ $^{18}\text{F}$ ]FDG synthesized on-chip was further validated by a comparison study of *in vivo* biodistribution within a lymphoma xenograft-bearing mouse [60]. A 60  $\mu\text{L}$  (38  $\mu\text{Ci}$ ) batch of purified [ $^{18}\text{F}$ ]FDG produced by the EWOD radiosynthesizer, was formulated with 40  $\mu\text{L}$  of saline solution (0.9% wt./vol. of NaCl) and injected via the tail vein. Following a one hour delay for uptake and nonspecific clearance, the mouse was imaged for 10 minutes in a small animal PET scanner (MicroPET Inveon, Siemens), followed by a microCT scan (microCAT II, Siemens). Scan data was coregistered into a single image and reconstructed using a 3D filtered back-projection reconstruction algorithm for quantitation (Fig. 3.6).



(A)

(B)

Fig 3.6: Small animal PET/CT images of lymphoma xenograft-bearing mouse. (A) After administration of [ $^{18}\text{F}$ ]FDG prepared with EWOD radiosynthesizer. (B) After administration of [ $^{18}\text{F}$ ]FDG prepared at UCLA Biomedical Cyclotron facility [60].

Regions of interest were drawn around the tumor, heart, left kidney, right kidney, and bladder to calculate percent uptake. On the next day, the same mouse was injected with [ $^{18}\text{F}$ ]FDG obtained from the UCLA Biomedical cyclotron for comparison [60]. The percent uptake in organs was similar in PET imaging with each sets of [ $^{18}\text{F}$ ]FDG, but the percent uptake in the tumor was larger on the second day because it had grown 30% (Table 3.2).



Table 3.2: Biodistribution (% uptake) of [ $^{18}\text{F}$ ]FDG within same mouse on consecutive days. The tumor grew approximately 30% between the two micro-PET images [60].

Organ	% Uptake (EWOD [ $^{18}\text{F}$ ]FDG)	% Uptake (cyclotron facility [ $^{18}\text{F}$ ]FDG)
Whole body	100	100
Tumor	2.8	4.6
Heart	1.6	1.5
Left kidney	1.2	1.2
Right kidney	1.2	1.3

### 3.6.2 Quality control and imaging of [ $^{18}\text{F}$ ]FLT

[ $^{18}\text{F}$ ]FLT produced by the EWOD radiosynthesizer was purified using a miniaturized cartridge that contained 5 mg of ion retardation resin, 5 mg of cation exchange resin, 30 mg of neutral alumina, and 150 mg of Oasis HLB resins packed within a 1-mL syringe barrel (Becton, Dickinson and Company) [4]. Polyethylene frits (20  $\mu\text{m}$  pore size) were used to hold the resins and prevent formation of air bubbles. The cartridges were conditioned with 1 mL of methanol and 2 mL of water before use. The crude reaction mixture collected from the chip was passed through the cartridge to trap the desired product. Sequential elution with 9 mL of 1% ethanol in water, and 6 mL of 5% ethanol in water, and a final washing step of 0.2 mL of 100% ethanol was used to release side products to waste. After removal of side products, [ $^{18}\text{F}$ ]FLT product was eluted from the cartridge using 0.5 mL of ethanol and collected into a sterile empty vial. Ethanol

was then removed from the purified product by evaporation with heating at 75°C and a nitrogen stream for 5 minutes. The dried [<sup>18</sup>F]FLT residue was then re-dissolved in 0.2 mL of saline.

Radiochemical purity was determined by radio-TLC (Fig. 3.7A). A small aliquot of the formulated product was spotted onto a silica gel plate and developed with 50:50 (vol/vol) ethyl acetate/ethanol. Radioactivity distribution along the silica gel-plate was determined with a radio-TLC scanner and verified that the final product was obtained in greater than 99% radiochemical purity [4].

Chemical purity of the formulated [<sup>18</sup>F]FLT was analyzed using an analytical HPLC with ultraviolet detection at 265 nm and a radiodetector (Fig. 3.7B). Product and impurities (such as 2',3'-didehydro-3'-deoxy-thymidine (stavudine) and thymidine) in the final sample were identified by comparing their retention times to known standards. The final sample contained 0.3 ppm of stavudine, 0.05 ppm of thymine, and 0.07 ppm of FLT [4].

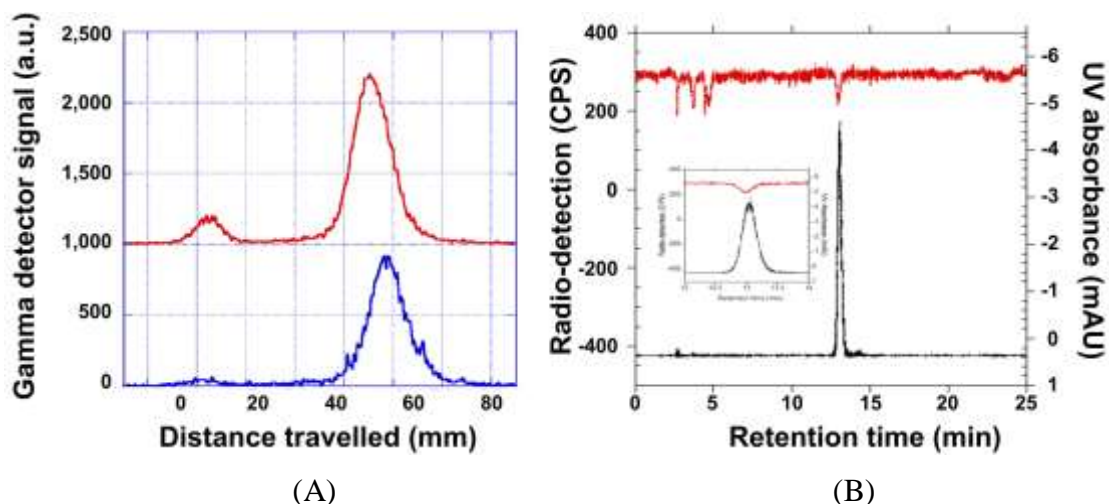


Fig 3.7: (A) Representative radio-TLC of crude [ $^{18}\text{F}$ ]FLT mixture (red trace) and cartridge purified [ $^{18}\text{F}$ ]FLT (blue trace). (B) Representative HPLC chromatogram used for specific activity analysis of [ $^{18}\text{F}$ ]FLT. The inset displays a narrow region where both UV and radio peaks of FLT can be observed and quantified [4].

The final product solution was observed to be clear and free of particulates and its pH was between 6.5 and 7 (measured by paper test strips). The LAL test for endotoxins detected less than 1 EU/mL in the final sample, which is lower than the established U.S. Pharmacopeia endotoxin limit of 175 EU/mL per dose for radiopharmaceuticals [4].

Starting with approximately 333 MBq (9 mCi) of radioactivity on the EWOD chip, 52 MBq (1.4 mCi, not decay-corrected) of [ $^{18}\text{F}$ ]FLT was successfully prepared after cartridge purification and formulation. Specific activities of EWOD produced [ $^{18}\text{F}$ ]FLT were measured to be 1,800-2400 GBq/ $\mu\text{mol}$  (48-64 Ci/ $\mu\text{mol}$ ), which are more than 10 times higher than literature reports using conventional macroscale radiosynthesizers [4].

Residual solvents in the formulated [ $^{18}\text{F}$ ]FLT were analyzed with gas chromatography, which showed that the final product contained less than 20 ppm of acetonitrile (400 ppm allowable limit), DMSO (5,000 ppm allowable limit), ethanol (5,000 ppm allowable limit), and thexyl alcohol (5,000 ppm allowable limit) [4].

The quality of [ $^{18}\text{F}$ ]FLT synthesized on-chip was further validated by small-animal PET imaging studies of several A431 (human epidermis carcinoma cell line) tumor-bearing mice using a microPET Inveon scanner (Siemens Preclinical Solutions, Malvern, PA) and MicroCAT II CT scanner (Siemens Preclinical Solutions, Malvern, PA). The mice were injected in the tail vein with 1.5 to 1.7 MBq (40 to 45  $\mu\text{Ci}$ ) of [ $^{18}\text{F}$ ]FLT in saline. After 60 minutes of uptake time, the mice were anesthetized with 2% isoflurane and placed in microPET and microCAT chambers. As expected, the PET images showed high accumulation of [ $^{18}\text{F}$ ]FLT in the tumor due to high level of expression of thymidine kinase-1 enzyme in rapidly proliferating cells (Fig. 3.8). No adverse effect on the physiology of the mice was observed after injection [4].

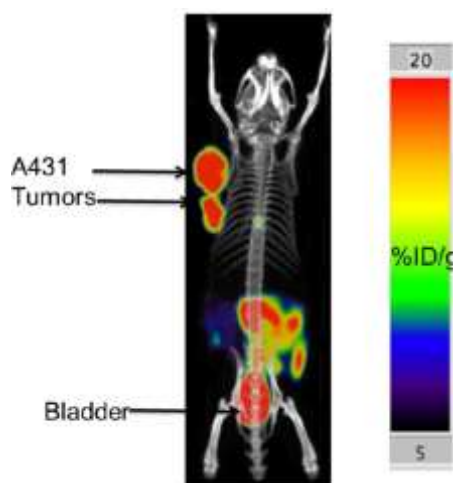


Fig 3.8: Biodistribution of EWOD synthesized [ $^{18}\text{F}$ ]FLT in a mouse bearing A431 tumors [4].

### 3.6.3 Quality control and conjugation of [<sup>18</sup>F]SFB

Crude product of [<sup>18</sup>F]SFB produced on the EWOD chip was injected directly onto an analytical HPLC (with UV detector (305 nm) and  $\gamma$ -ray detector) for purification. The [<sup>18</sup>F]SFB was separated using an isocratic elution of MeCN/H<sub>2</sub>O/TFA 50:50:1 (v/v/v) at a flow rate of 0.5 mL/min and it was collected in a 20 mL scintillation vial that already contained 3  $\mu$ L of acetic acid (1 M). The collected [<sup>18</sup>F]SFB was dried directly on a hot plate at 75°C with a nitrogen stream for 10 minutes to evaporate the HPLC mobile phase. Dried [<sup>18</sup>F]SFB was then transferred to a 2 mL Eppendorf vial using 0.5 mL of acetonitrile and placed in a water bath to evaporate the acetonitrile.

Radiochemical purity of EWOD produced [<sup>18</sup>F]SFB was determined by radio-TLC (Fig. 3.9A). A small aliquot of the formulated product was spotted onto a silica gel plate and developed with 1:1 (vol/vol) ethyl acetate/hexane. Radioactivity distribution along the silica gel-plate was determined with a radio-TLC scanner and verified that the final purified product was obtained in greater than 99% radiochemical purity. Chemical purity of the formulated [<sup>18</sup>F]SFB was verified using a different analytical HPLC (Fig. 3.9B).

[<sup>18</sup>F]SFB was conjugated onto anti-Prostate Stem Cell Antigen (PSCA) diabody (A2 DB) to form <sup>18</sup>F-labeled A2 Db ([<sup>18</sup>F]FB-A2 Db) as described by Liu et al. [93]. Purified [<sup>18</sup>F]FB-A2 Db was produced with 34.4% radiolabelling yield of [<sup>18</sup>F]SFB onto A2 Db, 106.2 kBq/ $\mu$ g (2.87  $\mu$ Ci/ $\mu$ g) specific activity, and 98.9% radiochemical purity.

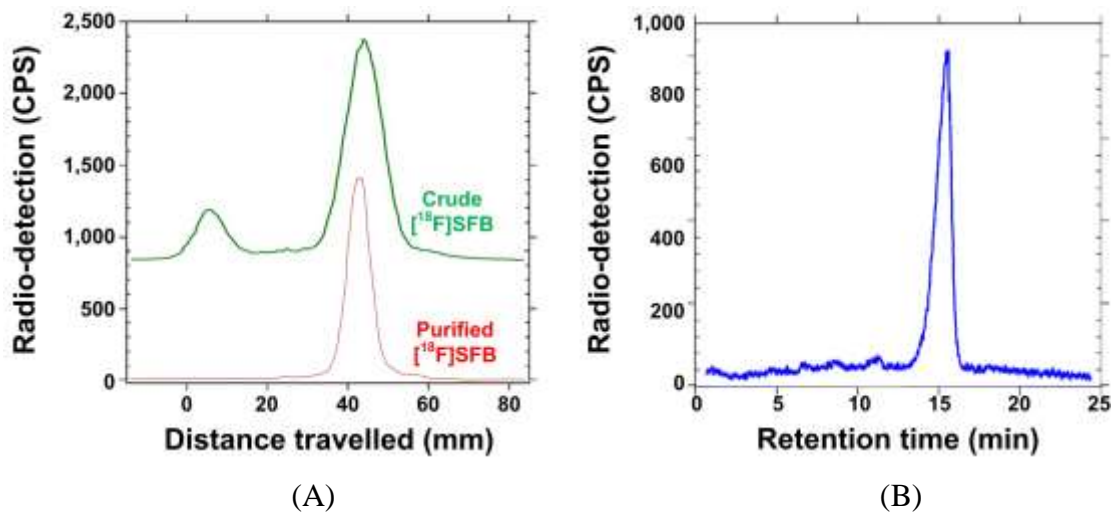


Fig 3.9: (A) Representative radio-TLC of crude [ $^{18}\text{F}$ ]SFB (green trace) and purified [ $^{18}\text{F}$ ]SFB (red trace). (B) Representative radio-HPLC chromatogram of purified [ $^{18}\text{F}$ ]SFB.

### 3.6.4 Quality control and imaging of [ $^{18}\text{F}$ ]fallypride

Crude product of [ $^{18}\text{F}$ ]fallypride produced on the EWOD chip was injected directly onto an analytical HPLC (with UV detector (305 nm) and  $\gamma$ -ray detector) for purification [58]. The [ $^{18}\text{F}$ ]fallypride was separated using an isocratic elution of MeCN/HCOOHNH<sub>4</sub> (aq, 25 mM) 55:45 v/v and 1% of triethylamine at a flow rate of 1 mL/min. The [ $^{18}\text{F}$ ]fallypride was collected (2 mL) and diluted with water (15 mL) and then passed through a preconditioned t-C18 cartridge to remove the HPLC mobile phase. [ $^{18}\text{F}$ ]fallypride was eluted from the cartridge using ethanol (1.5 mL) and then ethanol was evaporated at 75°C under nitrogen flow for 10 minutes. The dried residue was reformulated in 0.5 mL of saline for micro-PET imaging.

Radiochemical purity of [ $^{18}\text{F}$ ]fallypride was determined by radio-TLC (Fig. 3.10A). A small aliquot of the formulated product was spotted onto a silica gel plate and developed with 65:45 (vol/vol) acetonitrile/ammonium formate (25 mM) + 1% triethylamine. Radioactivity distribution along the silica gel-plate was determined with a radio-TLC scanner and verified that the final purified product was obtained in greater than 99% radiochemical purity [58]. Chemical and radiochemical purity of the formulated [ $^{18}\text{F}$ ]fallypride was verified using a different analytical HPLC (C18 luna column, 1.5 mL/min, UV detector at 254 nm wavelength) (Fig. 3.10B).

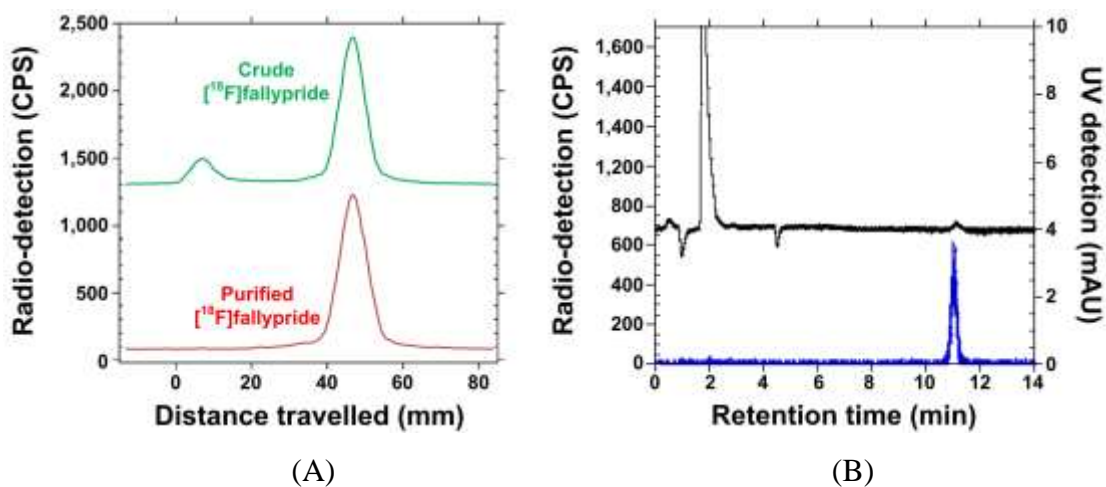


Fig 3.10: (A) Representative radio-TLC of crude [ $^{18}\text{F}$ ]fallypride (green trace) and purified [ $^{18}\text{F}$ ]fallypride (red trace). (B) HPLC chromatogram of reformulated [ $^{18}\text{F}$ ]fallypride synthesized on the EWOD chip [58]. The initial large peak in the UV trace (black line) is a solvent peak (type of artifact) and does not represent any impurities.

For specific activity measurement, cold mass of the synthesized fallypride was calculated from analytical HPLC data based on a calibration curve of standard fallypride, and radioactivity was measured using a dose calibrator. Specific activity of [ $^{18}\text{F}$ ]fallypride synthesized on the EWOD chip was 730 GBq/ $\mu\text{mol}$  (19.7 Ci/ $\mu\text{mol}$ ), despite starting with only 290 MBq (8 mCi) of radioactivity [58]. In comparison, [ $^{18}\text{F}$ ]fallypride produced by the NanoTek capillary reactor under optimal conditions, was 4 times lower at 185 GBq/ $\mu\text{mol}$  (5 Ci/ $\mu\text{mol}$ ) despite starting with a higher radioactivity of 555 MBq (15 mCi) [36].

The EWOD produced [ $^{18}\text{F}$ ]fallypride had sufficiently high specific activity for imaging the striatum in the brain of healthy BALB/c mice. Mice were anesthetized with isoflurane (4%), injected with [ $^{18}\text{F}$ ]fallypride (3.5-7.5 MBq / 94-201  $\mu\text{Ci}$ ) via tail vein, and imaged via microPET for 60 minutes (MicroPET Inveon, Siemens) followed by a microCT scan (microCAT II, Siemens). MicroPET and microCT scans were reconstructed using a 3D filtered back-projection algorithm and co-registered to yield a single image (Fig. 3.11A). Regions of interest of the left and right striatum were drawn to calculate the ratio of specific binding to non-specific binding and the cerebellum was used as a reference region to measure non-specific binding (Fig. 3.11B). Both the left and right striatum were clearly visualized [58].



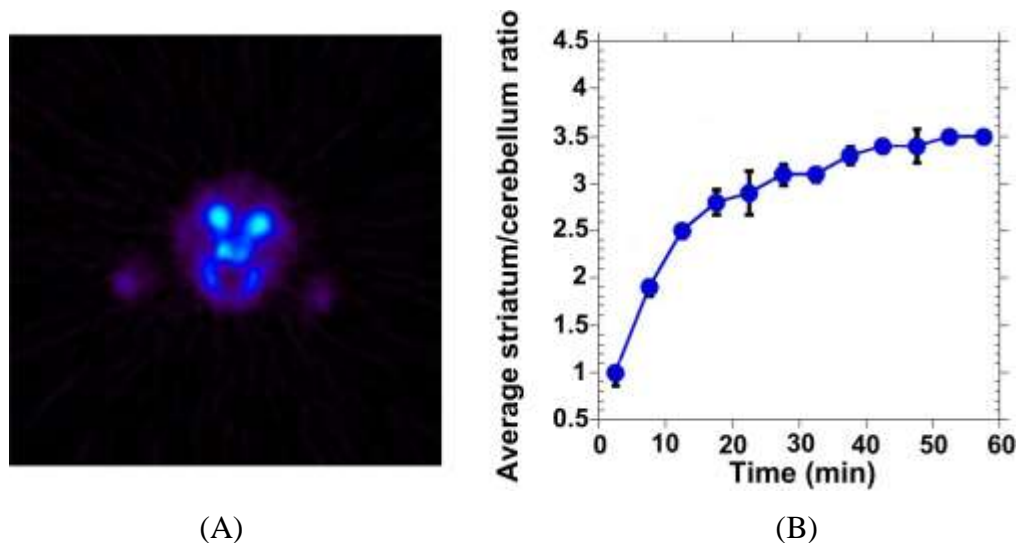


Fig 3.11: (A) Representative micro-PET image of striatum in brain of a mouse using  $[^{18}\text{F}]$ fallypride prepared on an EWOD microfluidic radiosynthesizer. (B) Average ratio of  $[^{18}\text{F}]$ fallypride binding in the striatum versus the cerebellum as a function of scan duration for the microPET experiment [58].

### 3.7 Summary

We have developed an EWOD radiosynthesizer in an effort to create an affordable and flexible platform to enable researchers and clinicians to produce their own tracer of interest on demand. To demonstrate the success of the effort, we have successfully performed several classes of radiochemical reactions (including aliphatic nucleophilic substitution, aromatic nucleophilic substitution, hydrolytic deprotection, saponification, and esterification) using one EWOD chip design. Our goal is a universal chip that can produce the radiotracer of choice as long as reagents are provided. A mass-produced universal chip may be disposable and fresh for

each radiosynthesis, allowing imaging centers to produce multiple, different radiotracers back-to-back by simply swapping the chips and reagents.

To date, [ $^{18}\text{F}$ ]FDG and [ $^{18}\text{F}$ ]NaF are the only two radiotracers that are routinely available from commercial radiopharmacies. Other PET tracers are highly expensive or only available from specialized radiochemistry facilities. Several research groups have advanced microfluidic radiosynthesizer technology in recent years, and the first microfluidic device for clinical production of human doses of  $^{18}\text{F}$ -labeled PET tracers was presented in early 2013 [32].

The EWOD radiosynthesizer is distinctive as the only batch microfluidic reactor using droplets in air or an inert gas. Advantages in its flexibility for radiosynthesis (because fluid paths are software-programmable) and ease of evaporation steps were demonstrated. The EWOD radiosynthesizer also has the potential to produce radiotracers with unprecedented high specific radioactivity [58].

In this chapter, concentration, solvent exchange, and reaction steps on an EWOD device were described for radiosynthesis of several PET tracers, but purification was performed off chip. The next chapter will discuss incorporation of purification steps onto the EWOD device.

## CHAPTER 4: ON CHIP SOLID-PHASE EXTRACTION FOR RADIOISOTOPE REMOVAL

### 4.1 Overview

After the final reaction has been completed in the radiochemistry process, it is necessary to purify the reaction mixture in order to isolate the radiolabeled tracer from impurities that should not be present in the final prepared product for injection [2]. Impurities in the radiochemistry process arise from incomplete reactions, degradations, radiolysis, radionuclide production contaminants, and excess reagents like precursor and radioisotope [105]. Purification to remove these impurities can be accomplished by several chemical separation methods, which typically involve a solid-phase or resin for trapping or retardation. For example, in the synthesis of [ $^{18}\text{F}$ ]FDG, the crude product is passed through alumina resin to trap any unreacted [ $^{18}\text{F}$ ]fluoride.

This chapter discusses two approaches to implementing purification steps on the EWOD device. In one approach, an exposed portion of the EWOD cover plate was functionalized to remove excess fluoride by trapping on the surface (Fig. 4.1A) [106]. In the second approach, sorbent particles used in radiochemistry cartridge purification were loaded to the device, mixed with the crude reaction mixture to remove fluoride, and then separated from the desired radiotracer by mechanical filtration (Fig. 4.1B) [107].

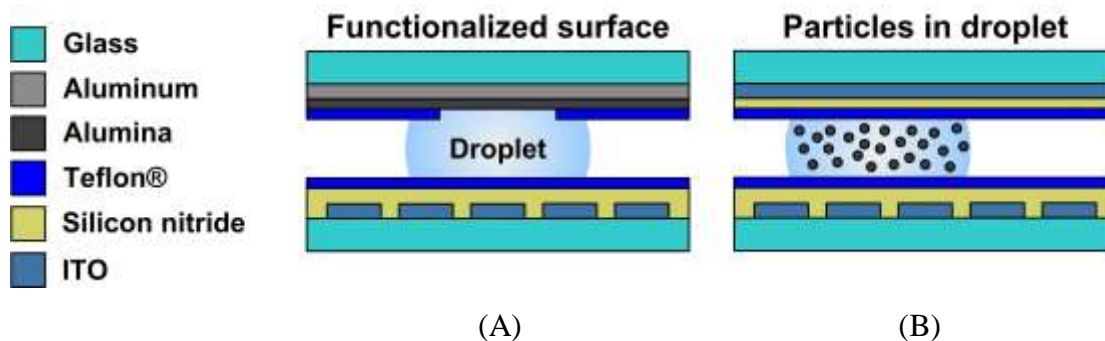


Figure 4.1: Two methods of on-chip purification (A) Exposed functionalized surface in Teflon® window to remove fluoride from the droplet. (B) Purification particles mixed within droplet to remove fluoride.

$^{18}\text{F}$ Fluoride was chosen as the analyte to evaluate extraction because it is both easy to measure with radioactivity detectors and it is relevant to radiochemistry. Removal of excess  $^{18}\text{F}$ fluoride after tracer synthesis reactions is important because any leftover  $^{18}\text{F}$ fluoride injected into a living subject is likely to be taken up into bone, causing a high background signal and complicating interpretation of images [108].

Both methods for on-chip purification were evaluated using radio-TLC to compare the product from  $^{18}\text{F}$ fallypride synthesis before and after fluoride removal. In both cases, nearly all the excess  $^{18}\text{F}$ fluoride was removed. Because on-chip purification separates the intended product from excess fluoride, it enables an on-line measurement of fluorination reaction yield when used in combination with Cerenkov imaging of radioactivity. An initial evaluation of the proposed reaction yield measurement technique is also presented in this chapter.

## 4.2 Conventional radiochemistry purification

The most general method for radiotracer purification is high-performance liquid chromatography (HPLC), an analytical tool used in drug discovery, development, and production [20, 109]. HPLC utilizes a column packed with chromatographic separation material, a mobile phase (or solvent), a high pressure pump, and detectors (to identify both the chemical and radiation signals in the case of radiochemistry) [20]. After a reaction mixture is injected into an HPLC, components of the reaction mixture will have characteristic retention factors ( $R_f$ ) based on different interactions with both the column (stationary phase) and elution buffer (mobile phase). Because the reaction mixture components exit the column at different times, the desired product can be separated from impurities by collecting the column output at the correct time.

Although HPLC, with proper selection of column and elution buffer, can be used to purify nearly all radiotracers, it also adds a significant amount of time to the radiochemistry process, which is a concern for short half-life radiotracers. Several groups have circumvented time-consuming HPLC by developing solid-phase extraction (SPE) methods as a faster alternative for purification of radiotracers like [ $^{18}\text{F}$ ]FDG, [ $^{18}\text{F}$ ]FLT, [ $^{18}\text{F}$ ]SFB, and 2- [ $^{18}\text{F}$ ]fluoroethyl-choline [60, 110, 111, 112]. In solid-phase extraction, sorbents adsorb components from the solution surrounding it through use of a variety of forces such as van der Waals, hydrogen-bonding, dipole-dipole interactions, hydrophobic interaction, or ion-exchange processes. In some cases, impurities are adsorbed onto SPE sorbents as the product passes through. In other cases, the desired product is first adsorbed onto a sorbent while impurities pass through, and then the desired product is released by passing through an elution solvent..

Disposable SPE cartridges have become the standard purification method for producing [ $^{18}\text{F}$ ]FDG with automated radiosynthesizers, like GE TRACERlab, Synthra FDG<sup>two</sup>, IBA Synthera®, Eckert & Ziegler FDG-Plus, and Siemens Explora® FDG<sub>4</sub> Module. In the case of [ $^{18}\text{F}$ ]FDG, cartridges are packed with cation exchange resin or anion exchange resin (to neutralize the acid or base used in the deprotection step), ion exchange resins (to trap any remaining ionic species), alumina (to retain unreacted fluoride ions), and reverse-phase silica or C-18 functionalized beads (to remove organic impurities like Kryptofix) (Fig. 4.2) [60, 113].

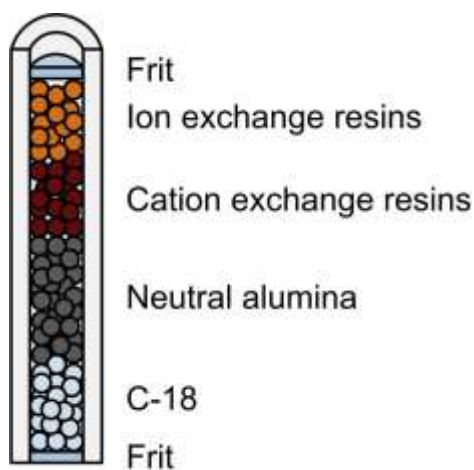


Figure 4.2: Diagram of custom made cartridge for purification of [ $^{18}\text{F}$ ]FDG with SPE sorbents packed within a 760  $\mu\text{m}$  inner diameter perfluoroalkoxy tube and held between two frits [60].

### 4.3 Microfluidic solid-phase extraction

Recently, microfluidic chips have been designed for solid-phase extraction of radiotracers [114, 115]. The SPE chips consisted of glass channels (30 mm x 4.7 mm, 300  $\mu\text{m}$  depth) packed with SPE particles and were used for purification of [ $^{18}\text{F}$ ]FDG with less required fluid volume and mass of SPE particles compared to cartridges used by commercial macroscale radiosynthesizers. The SPE chips were suitable for a modular radiochemistry-on-chip platform, in which the platform could be modified for the production of a variety of radiotracers simply by inserting the appropriate modules (such as concentration module, solvent-exchange module, reactor module, and purification module) [31]. However, in the case of an EWOD radiosynthesizer, which is intended to be a flexible radiotracer production system with only electronic reconfiguration and small volume batch operation of fluids (instead of continuous flow), it is necessary to further scale down the purification and on-chip implementation would be ideal.

Various types of solid-phase extraction have been performed on EWOD devices. Shah et al. used antibody-conjugated magnetic beads to concentrate cells specifically bound to the beads through a combination of magnetic collection and EWOD droplet splitting [116]. In a different approach by Yang et al. [117], a porous polymer monolith was first prepared on chip as a SPE solid stationary phase by photopolymerization with UV exposure through the glass substrate and then it was used to remove salts and surfactants from droplets. Several other promising methods for separation on an EWOD device were demonstrated but not used for purification [118, 119]. Cho et al. [118], demonstrated on chip capillary electrophoresis of carboxylate modified latex particles and polystyrene beads by patterning exposed electrodes in the cover plate to generate an

electric field within the droplet through direct electrical contact. After different particle types were localized according to their charge, droplets could be split by EWOD actuation to separate them. However, the applied voltage for electrophoresis was limited to below  $5 V_{DC}$  due to electrolysis. Particles were also separated on chip by Schertzer et al. [119], who showed that photolithography patterned polymer structures on an EWOD device could be used for the mechanical filtration of droplets. Mechanical filtration of a single droplet is difficult in EWOD, because small pore sizes present a significant capillary pressure that obstructs droplet movement and prevents the droplet from crossing the filter. However, after a second droplet from the opposite side of the filter is merged with the first droplet (4.3B), the total fluid volume can pass across the filter with only EWOD actuation (Fig. 4.3D).

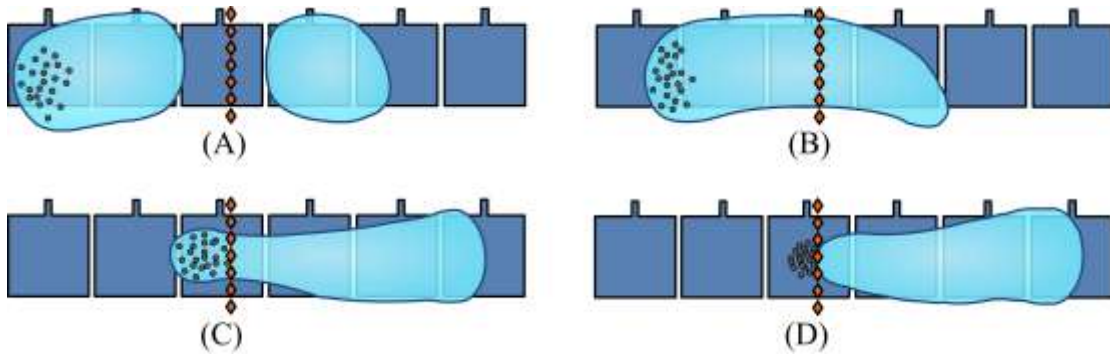


Figure 4.3: Scheme of droplet being drawn passed filter structures (shown as vertically aligned small red diamonds). (A) Droplets are moved to the obstruction from opposite sides. (B) Droplets are merged across the obstruction. (C) The merged droplet is pulled away from the obstruction. (D) The droplet is pulled entirely through [119].



Mechanical filtration of sorbent particles is a promising approach for on chip SPE with EWOD devices, because conventional, commercially-available sorbent particles can be used without any further chemical modification to the device or purification media, and because a broad range of purification processes can be implemented simply by selecting the type(s) of sorbent particles used. Although a mechanical filter structure needs to be added to the chip, only electrowetting actuation is required for separation of particles.

#### 4.4 Exposed alumina for on chip removal of fluoride

##### 4.4.1 Alumina as dielectric and SPE surface

Recognizing that alumina has been used as a dielectric layer for EWOD [120] and also as a sorbent for SPE removal of ions, our initial approach to incorporate SPE on an EWOD device was to use alumina both as an insulating layer and as an adsorptive surface for removal of fluoride (Fig. 4.4).

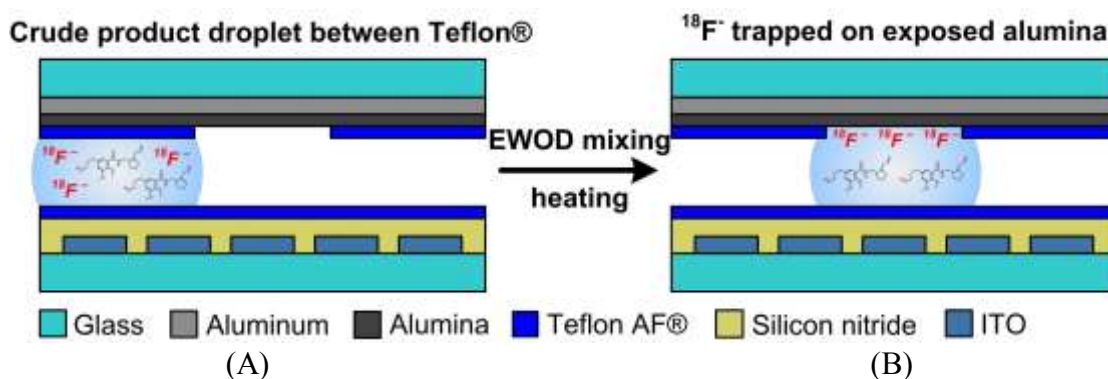


Figure 4.4: Cross-section schematic of exposed alumina on EWOD cover plate for removal of fluoride by SPE. (A) Crude reaction mixture droplet moved to exposed alumina (through window in Teflon® layer). (B) After EWOD mixing and heating, fluoride is adsorbed onto the exposed alumina.

The purification cover plate was fabricated by evaporating aluminum (65 nm) onto glass slides. Nonporous alumina was grown by anodization with a constant current step (1 mA, 20 min) and a constant voltage step (60 V, 1 hour). A conductive but transparent 15 nm aluminum layer was left beneath the grown alumina (80 nm) (Fig. 4.5). Bake steps (500°C, 3 hours) were used before and after anodization to induce  $\gamma'$ -Al<sub>2</sub>O<sub>3</sub> crystalline formation [121]. Teflon® (Teflon AF 1600) was spin-coated and patterned by lift-off of low-tack tape to open a window for the underlying alumina. EWOD actuation on alumina-exposed regions was confirmed with repeatable actuation of water, acetonitrile, dimethyl sulfoxide, and methanol droplets using 90 V<sub>rms</sub>, 10 kHz.

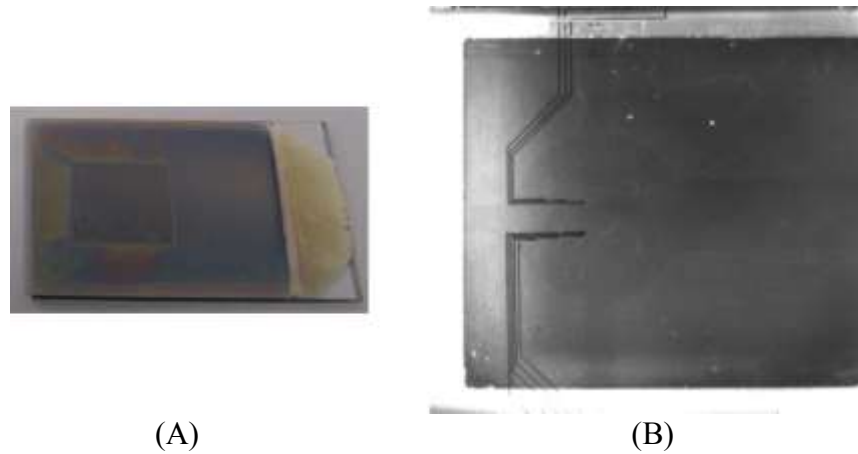


Figure 4.5: (A) Cover plate with a window in the Teflon® layer to expose the underlying alumina. (B) Video image of exposed alumina ground plate assembled over EWOD actuation plate. The 15 nm aluminum electrical ground layer is transparent.

#### 4.4.2 Fluoride adsorption on alumina cover plate

Fluoride adsorption on various cover-plate surfaces was examined by squeezing cyclotron-produced [ $^{18}\text{F}$ ]fluoride ion in water droplets between parallel plates with a 150  $\mu\text{m}$  gap for 10 minutes. The loaded radioactivity was measured in a dose calibrator (CRC-25R, Capintec). The plates were then separated and washed with 20  $\mu\text{L}$  of water before the radioactivity of each plate was again measured. Fluoride trapping efficiency was quantified as the ratio of radioactivity left on the plate compared with the radioactivity initially loaded. Fluoride trapping on an alumina cover plate baked at 500°C was also examined with EWOD mixing (30 sec) and resistive heating (85°C, 3 min).

As seen in Table 4.1, both alumina prepared without any baking steps and bare glass trapped nearly an equal amount of radioactivity, 17% of the total. After baking at 500°C, the trapping efficiency increased to 43% (for 3 hour bake time) and 61% (for 6 hour bake time), suggesting that the heat treatment had induced a transformation in the alumina to a crystalline phase that was more effective for fluoride adsorption [121, 122]. When EWOD mixing and resistive heating were also used, the trapping efficiency improved to 97%.

Table 4.1: Adsorption of fluoride ion on various cover-plate surfaces.

Sample	% Radioactivity on cover plate		
	No mixing or heating	EWOD mixing, no heating	EWOD mixing + heating
<i>Alumina (baked 6 hrs at 500°C), after extraction</i>	61%	95%	97%
<i>Alumina (baked 6 hrs at 500°C), after water wash</i>	61%	81%	94%
<i>Alumina (baked 3 hrs at 500°C)</i>	43%	Not tested	Not tested
<i>Alumina (no baking)</i>	17%	Not tested	Not tested
<i>Bare glass</i>	17%	Not tested	Not tested
<i>Teflon®-coated glass</i>	0%	Not tested	Not tested

#### 4.4.3 Fluoride removal after radiolabelling

To demonstrate on-chip removal of [<sup>18</sup>F]fluoride, [<sup>18</sup>F]fallypride was radiolabeled on chip as previously discussed in Chapter 3. At the end of synthesis, the regular ITO/silicon nitride cover plate was replaced with an exposed alumina version. Crude product was first collected using a micropipette with 10 µL of MeOH and MeCN and analyzed by radio-TLC to quantify the ratio of [<sup>18</sup>F]fluoride compared with the [<sup>18</sup>F]fallypride product. Crude product was then transferred back onto the chip and squeezed between the parallel plates. An EWOD mixing sequence (30 seconds) and heating (65°C, 4.5 minutes) were used to facilitate adsorption of ions onto the exposed alumina surface. The remaining droplet was collected by syringe after removal of the alumina cover plate. Radiochemical purity (proportion of total radioactivity labeled onto desired radiotracer) was analyzed by radio-TLC.

The initial radio-TLC of crude product showed a radiofluorination efficiency of 88%, which was typical for the on-chip [ $^{18}\text{F}$ ]fallypride synthesis by EWOD (Fig. 4.6A). After the fluoride removal step, the final product radiochemical purity was 100% (Fig. 4.6B). The radio-TLC showed that all of the unreacted [ $^{18}\text{F}$ ]fluoride was removed from the crude reaction mixture.

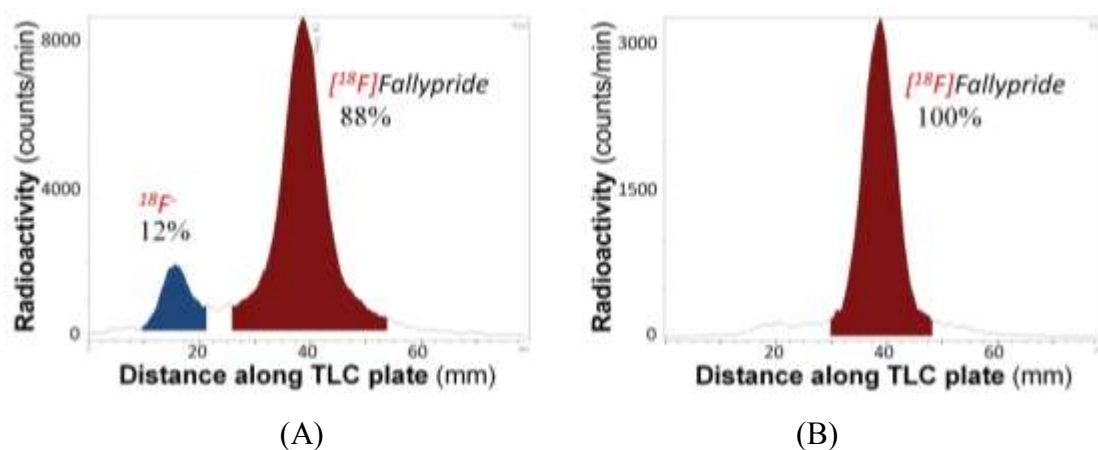


Figure 4.6: Radio-TLC analysis. (A) Crude product to determine the radiofluorination efficiency of [ $^{18}\text{F}$ ]fallypride. (B) Purified product after extraction using the alumina exposed cover plate.

The demonstration of planar alumina as a solid-phase extraction surface shows that with adequate mixing, it is possible to perform purification on chip in a parallel-plate EWOD device using only surface modifications, eliminating the use of a packed column. The alumina cover plate was only designed to remove [ $^{18}\text{F}$ ]fluoride, but with further processing alumina can be prepared for adsorption of other ions, amines, and aromatic compounds [123]. However, the type of surface functionalization required for purification would depend on the radiotracer that is

synthesized. The exposed area necessary for the trapping would also vary depending on the quantity of adsorbents and surface density of trapping sites. Such a radiotracer dependent device change, does not fit with the overall goal of a single EWOD device for flexible synthesis of many radiotracers. Furthermore, the fluid could not be removed from the exposed alumina through EWOD alone and needed to be extracted by pipette, vacuum suction, or capillary forces (into a thin glass tube).

## **4.5 On-chip filtration of SPE particles**

### **4.5.1 Device design**

In a different approach to achieve on-chip purification, commercial SPE particles were loaded within droplets and used as the purification material. With this method, the EWOD device surface does not need to be functionalized to remove impurities. Instead of modifying EWOD surface chemistry, commercial sorbent materials specific for removing a desired chemical compound can be loaded for purification. After purification sorbent particles have been mixed with the crude product droplet to adsorb chemical compounds, they can be removed from the product droplet by filtration through mechanical filter structures on chip using only EWOD actuation.

The EWOD chip for synthesis and filtration of SPE particles had the main actuation electrodes on the bottom glass plate and a ground electrode on the top glass plate (Fig. 4.7). A mechanical filter was fabricated on the cover plate. It consisted of KMPR® pillars (140  $\mu\text{m}$  height, 60  $\mu\text{m}$  side-to-side gap between pillars) that were patterned into diamond shapes by photolithography, similar to the SU-8 pillars fabricated on the bottom plate by Schertzer et al.

[119]]. KMPR® was chosen as the thick photoresist material for pillars because it has been found to have better moisture resistance and adhesion compared to SU-8 [124]. In contrast to our previous radiochemistry on EWOD work, no dielectric was added to the cover plate except for the thin Teflon® layer used as a hydrophobic coating.

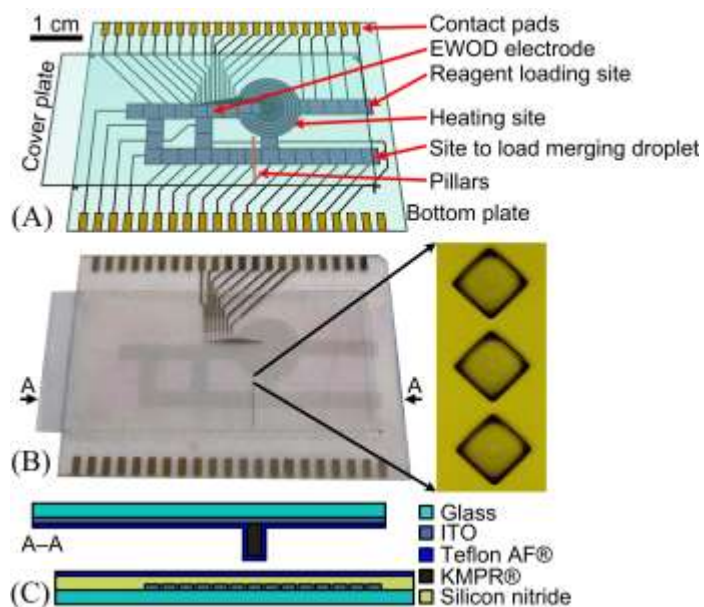


Figure 4.7: Device for on chip SPE by mechanical filtration. (A) Schematic of the chip showing the actuation glass plate patterned with EWOD electrodes, the electric contact pads along the two edges, and the electrical ground glass plate assembled on top. A single site at the cover plate edge was used to load reagents for radiosynthesis. A second site was used to introduce a droplet for merging with the crude product droplet at the filter site. (B) Assembled EWOD device with 12 mm circular reactor site (feedback-controlled resistive heaters) and filtration pillars on the cover plate. The zoomed in view shows pillars (140  $\mu\text{m}$  tall, 60  $\mu\text{m}$  gap between pillar edges). (C) Cross-sectional view of the chip.

The reactor site on the bottom plate was not changed from previous work and still consisted of 4 concentric multifunctional electrodes made from ITO, which could be used either for EWOD actuation or for feedback-controlled heating. Three droplet pathways of ITO square electrodes led to the reactor site, and a pathway loop was introduced for mixing reagents. A 2  $\mu\text{m}$  silicon nitride layer was deposited by plasma-enhanced chemical vapor deposition to serve as a dielectric. Teflon AF 2400® was spin-coated and annealed at 340°C to make the surface hydrophobic.

#### **4.5.2 Fluoride removal after radiolabelling**

A similar test of on-chip purification was conducted in which [ $^{18}\text{F}$ ]fallypride was synthesized on chip, and then [ $^{18}\text{F}$ ]fluoride was removed on the same chip. The radioactive material was loaded onto chip as two 2.5  $\mu\text{L}$  droplets of [ $^{18}\text{F}$ ]fluoride in water for a total of 4.4 mCi of radioactivity. The droplets were loaded at the top plate edge by pipette, and then electrowetting was used to pull the droplets into the plate gap and move them to the reactor site. A 2.5  $\mu\text{L}$  droplet of tetrabutylammonium bicarbonate (25 mM) was moved to the reactor site in a similar fashion and then mixed with the fluoride droplets using electrowetting. Water was removed from the loaded droplets by heating the reactor site to 105°C for 1 minute. An azeotropic drying step was completed to ensure water removal by loading 9  $\mu\text{L}$  of acetonitrile to the chip by pipette, mixing it with the dried fluoride and tetrabutyl bicarbonate using electrowetting, and then heating the mixture to 105°C for 1 minute. The material to be radiolabeled was added as a 4  $\mu\text{L}$  droplet of tosyl-fallypride in hexyl alcohol (75 mM). It was



moved to the reactor site by electrowetting and heated to 100°C for 7 minutes to perform the fluorination reaction.

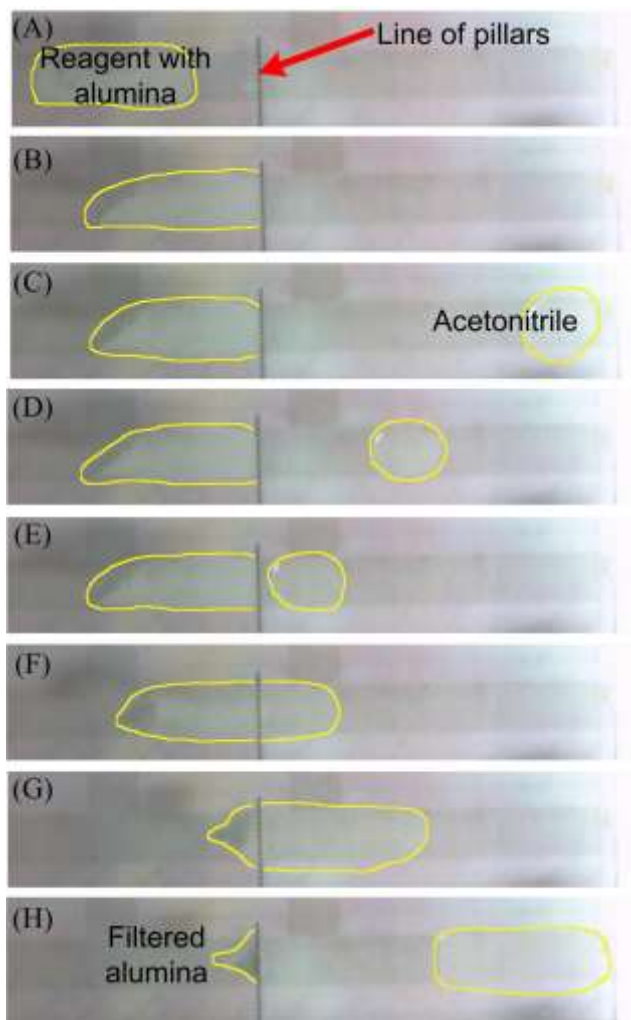


Figure 4.8: Filtration across line of pillars using electrowetting (from top down). (A-B) The reagent mixture droplet on the left side contains alumina particles and is moved to the filter. (C-G) A pure droplet of acetonitrile is loaded on the right side and brought to the filter site to help the reagent mixture droplet cross the filter. (H) After the droplet crosses the filter, particles remain on the left side. Outlines were added to the droplet images for clarity.

To measure fluorination yield, an aliquot of the reaction droplet was removed from the device with a capillary tube and spotted onto a silica gel plate (J.T. Baker, New Jersey). The silica gel plate was developed in a 1:1 mixture of methanol:ethyl acetate with a droplet of triethylamine and then analyzed in a radio-TLC scanner (MiniGITA star, Raytest).

Neutral alumina particles were purchased from ABX Advanced Biochemical Compounds (Radeberg, Germany). Alumina particles (80  $\mu\text{m}$  diameter) suspended in acetonitrile (0.5 mg alumina /  $\mu\text{L}$  acetonitrile) were pipetted onto the chip (3  $\mu\text{L}$  total) and mixed with the reaction droplet using electrowetting (Fig. 4.8). The mixture droplet was then pulled across a line of pillars, which filtered alumina particles out of the droplet. The effectiveness of fluoride removal was evaluated using radio-TLC of an aliquot sampled from the [ $^{18}\text{F}$ ]fallypride droplet. A measurement of  $99\% \pm 2\%$  (n=4) showed near quantitative removal of [ $^{18}\text{F}$ ]fluoride (Fig. 4.9). Typically SPE cartridges are packed with more than 10 mg of alumina to ensure enough surface interaction for trapping. However, with electrowetting mixing, only 1.5 mg of alumina was needed.

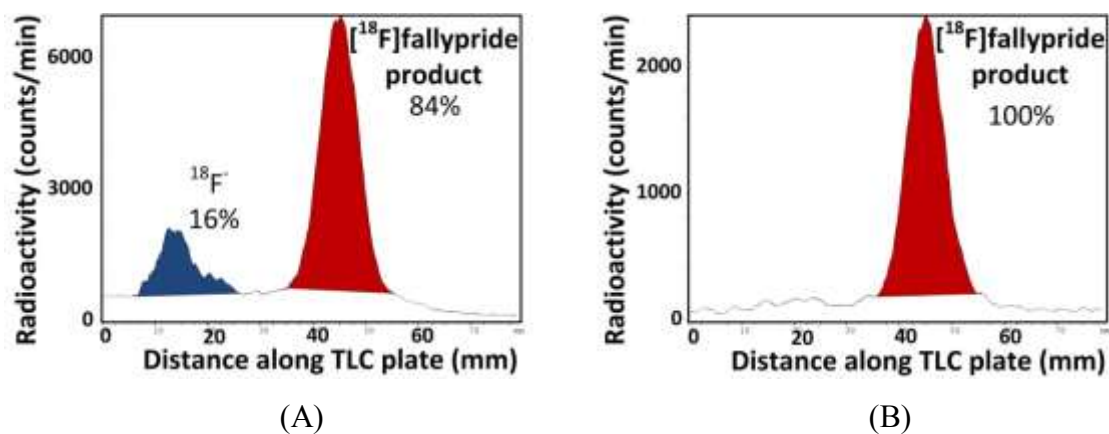


Figure 4.9: Radio-TLC analysis of: (A) crude mixture before purification. 84% of the radioactivity was labeled to the desired product  $[^{18}\text{F}]\text{fallypride}$ , and the other 16% was unreacted  $^{18}\text{F}^-$ , (B) The single peak of  $[^{18}\text{F}]\text{fallypride}$  at 45 mm from the left indicates a successful purification.

### 4.5.3 Reaction-yield measurement

After alumina had been filtered from the product droplet, a single Cerenkov image was tested as a substitute to radio-TLC for measurement of fluorination yield. The yield was measured by comparing the intensity of the Cerenkov radiation in the filtered alumina (and trapped  $[^{18}\text{F}]\text{fluoride}$ ) region with that of the  $[^{18}\text{F}]\text{fallypride}$  droplet (Fig. 4.10). The fluorination yield measured by Cerenkov imaging (82.0%) was consistent with the yield measured by radio-TLC (83.9%).

Quantitation of Cerenkov photons can depend on material properties such as chemical composition, density, and index of refraction of the material through which the beta particles pass [98]. For that reason, Cerenkov measurement of the  $[^{18}\text{F}]\text{fluoride}$  radioactivity on filtered

alumina particles may be complicated by both the alumina and nearby KMPR® pillars. Such complications can be avoided for Cerenkov measurement of fluorination yield by using two Cerenkov images. Total radioactivity can be quantified from a first image taken of the crude fluorination product before addition of alumina. Radioactivity of the fluorinated product can be quantified with a second image taken of the product droplet after filtration of alumina. In both images, no alumina or KMPR® pillars would interfere with the region of interest, and a more accurate measurement of fluorination yield would be expected through comparison of the fluorinated product radioactivity with the total radioactivity.



Figure 4.10: (A) Visible light image capture of droplet after filtration of alumina particles. (B) Cerenkov image, showing purified product droplet (right) and alumina-containing droplet (left).

#### 4.6 Summary

Addition of on-chip purification enables all four general stage of radiochemistry synthesis on one EWOD chip: concentration of cyclotron-produced [ $^{18}\text{F}$ ]fluoride ion, solvent exchange, reaction, and product isolation [5]. Although only alumina was used in the current

demonstration, the same mixing and filtration method are expected to be valid for other SPE resins and impurity removal, opening the door for complete on-chip purification of [ $^{18}\text{F}$ ]FDG and additional PET radiotracers at the end of synthesis, along with  $^{18}\text{F}$ -labeled intermediates in the cases when it is necessary mid-synthesis [20]. This technique has a significant advantage for mid-synthesis purification because it can be performed within the relatively small volume that is used on EWOD chips. Other techniques like cartridge and HPLC purification require use of a larger volume and often dilute the desired reagent, which would then need to be concentrated for further use on the EWOD chip.

Other SPE resins of interest are cation-exchange resin, ion-exchange resin, and C18, which in addition to alumina can be used to remove all the impurities for SPE purification of the most commonly used radiotracer, [ $^{18}\text{F}$ ]fluoro-2-deoxy-D-glucose ([ $^{18}\text{F}$ ]FDG) [60]. However, use of this method is limited to radiotracers that have sufficiently different chemical and physical properties from impurities involved with their synthesis; otherwise, SPE cannot be used for radiotracer purification, and product isolation is generally performed with HPLC instead. There are also cases, when a combined use of SPE and HPLC is required for complete purification, such as when excess fluoride is first removed by SPE to prevent it from saturating the HPLC column and spilling over into the product [108].

Filtration of alumina from the radiotracer droplet, which separates the radiofluorinated product from impurities (e.g. unreacted [ $^{18}\text{F}$ ]fluoride), also enabled on-chip measurement of the fluorination reaction yield using Cerenkov imaging. Although more development is needed to demonstrate its reliability and validity as an analytical method, the technique holds potential as an on-chip measurement for synthesis development or quality control. As an on-chip

measurement of fluorination yield, it has advantages in that sample does not need to be extracted (or lost), only a light-tight enclosure and sensitive CCD camera are required (instead of complex equipment like radio-TLC or radio-HPLC), and it can be performed in the same lead shielding that houses the EWOD chip (without causing further radioactivity exposure to a chemist). An on-chip measurement of reaction yield would also be beneficial for quicker optimization of radiotracer synthesis processes, particularly if devices are designed for testing different conditions in parallel, and the reaction yields can be measured simultaneously with a single Cerenkov image.

# CHAPTER 5: MIRRORED CONFIGURATION OF ANODIZED DIELECTRICS FOR RELIABLE ELECTROWETTING

## 5.1 Overview

An insulating layer is included in electrowetting-on-dielectric (EWOD) to prevent electrochemical reactions between the liquid and electrode surface when voltages were applied [42, 56]. The dielectric allows a higher electric field for stronger actuation force before electrical leakage or breakdown can occur [41].

Dielectric properties strongly affect the performance and reliability of EWOD devices. Desired would be a high dielectric constant and a high breakdown strength, so the dielectric could be deposited as a thin layer, which would reduce the required voltage that needs to be applied for a given electrowetting effect [38]. It should also be deposited as a pinhole free layer for reliable performance with low fabrication cost. Many dielectrics have been used for EWOD (*e.g.*, photoresists, PDMS, Parylene, silicon dioxide, silicon nitride, barium strontium titanite (BST), and bismuth zinc niobate (BZT)) [125], but it has been difficult to achieve both good electrical performance and easy deposition, because one generally limits the other.

Recently, valve metal oxides (*i.e.*, oxides grown from Al, Ta, Bi, Sb) grown by anodization have been proposed as promising layers for EWOD with high dielectric constants (8-110), high breakdown strength, and a simple low cost fabrication (low deposition temperature and free of reactive gases) [120, 126, 127]. Furthermore, because anodized valve metal oxides are grown electrochemically (with faster growth rates along weaker insulation paths), the formed layer is considered uniform with few pinholes [128].

However, valve metal oxides are so named because of their current rectifying behavior, which can impose a restricted range of allowable voltages when used for EWOD [120, 128, 129]. For anodized dielectrics, although the cathodic current is almost zero, anodic currents can be significant and increase with applied voltage (Fig. 5.1) [128].

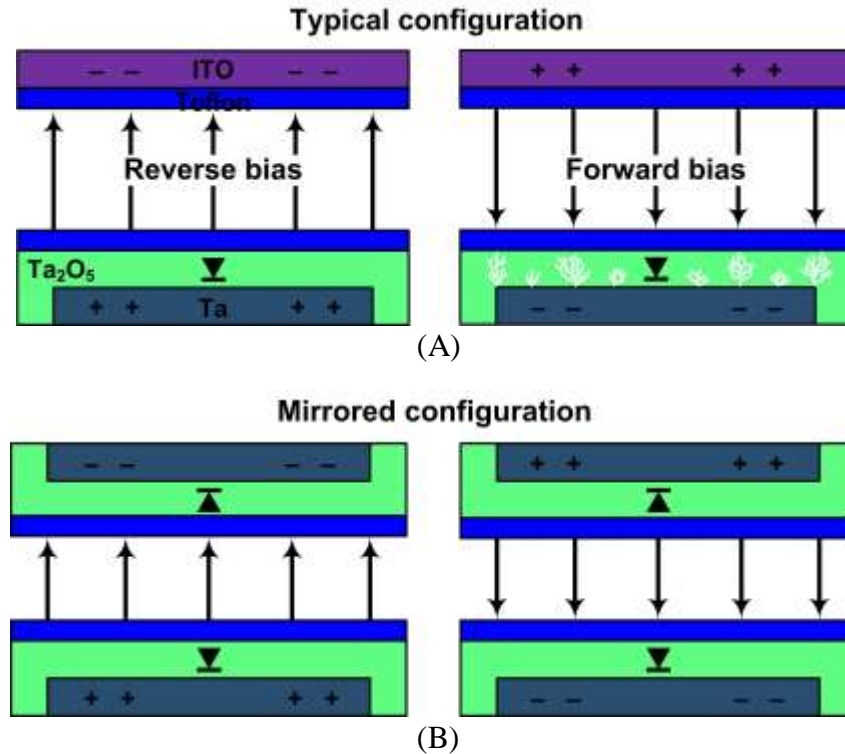


Figure 5.1: (A) Current rectifying behavior for a valve metal oxide (*e.g.*, Ta<sub>2</sub>O<sub>5</sub>) anodized from a valve metal (*e.g.*, Ta). Under reverse (negative) bias, the tantalum pentoxide (colored green) blocks current. However, under forward (positive) bias, the tantalum pentoxide passes current. The dielectric strength is higher under reverse bias than forward bias. Dielectric breakdown is indicated by white lines. (B) A mirrored configuration is proposed to assure one of the aluminum oxide layers is always under the correct (reverse) bias to restrict current.



This chapter introduces a mirrored configuration (resembling nonpolar electrolytic capacitors) to solve the main problem of using an anodized dielectric for EWOD, *i.e.*, the problem of allowing actuations only in one polarity [130]. Using tantalum pentoxide as the valve metal oxide for experimental evaluation, the proposed configuration is compared with the typical EWOD parallel-plate configuration (with no significant insulating dielectric on the plate used as a connection to electrical ground). The performance is further compared with silicon oxide and silicon nitride, which are considered most reliable among the common dielectrics for EWOD. Current leakage measurements under a range of applied biases confirm that in a mirrored configuration, one of the two opposing dielectrics would always be correctly biased to restrict current through the EWOD device. The utility is demonstrated by manipulating water droplets on both parallel-plate and coplanar electrode arrangements on EWOD devices.

## **5.2 Anodized dielectrics for EWOD**

The current rectifying behavior of the valve metal oxide used for EWOD was demonstrated by Huang et al. [129], who showed that the devices with anodized Ta<sub>2</sub>O<sub>5</sub> performed well when the droplet was applied a reverse biased DC or low frequency voltages under 100 Hz; but the performance deteriorated severely for forward biased DC or higher frequency AC voltages.

Despite their current rectifying effect, progress has been made to reliably use valve metal oxides as the primary dielectric in EWOD devices. Huang et al. [129] demonstrated that if the Ta<sub>2</sub>O<sub>5</sub> was sputter-deposited (instead of grown electrochemically) onto Ta and then anodized, the final dielectric layer was pinhole free and insensitive to polarities when tested with 13 V (13% of

the anodization formation potential) actuation sufficient for a contact angle change of  $18^\circ$ . It was not tested under higher voltages (greater than 50% of the anodization formation potential) under which a current-rectifying effect would be more noticeable [128]. There is also a concern with utility of sputtering  $Ta_2O_5$  before anodizing because an etch process to pattern electrodes would expose Ta sidewalls without the sputtered oxide. Other work used valve metals for “self-healing” dielectrics [127], in which any exposed portion of the electrode was anodized during the EWOD operation instead of undergoing electrolysis. However, droplet composition and voltage restrictions were involved in the self-healing devices, which require electrolyte droplet solutions within a limited pH range and application of a voltage polarity suitable for anodization.

### **5.3 Mirrored configuration of anodized dielectrics for EWOD**

Anodized dielectrics are used in electrolytic capacitors because they provide large capacitance to volume ratios at a low cost [131]. Although electrolytic capacitors use valve metal oxides that have current rectifying effects, nonpolar electrolytic capacitors can be formed when the anodized dielectric is incorporated on both capacitor electrodes in a mirrored (or symmetric) configuration [132]. In this configuration, one of the pair of valve metal oxide dielectrics will always be under the correct (reverse) bias to restrict current.

This concept was utilized to create a polarity dependent EWOD actuation for moving droplets across a surface without sequential activation of electrodes [133, 134]. They used a single high resistivity electrode and designed exposed aluminum vias through a thermal oxide dielectric that were spaced so that at least two vias were always beneath the droplet. The native oxide that formed on aluminum (a valve metal) acted as a diode so that current flowed through a

via on the low voltage side, but current was impeded by a via on the high voltage side of the droplet. The resulting charge accumulation on the high voltage side caused the droplet to move in its direction. Although current flowed through the droplet, it was limited by the use of diodes with opposite polarity.

Here, we propose a mirrored pair of valve metal oxides as the main dielectric for EWOD devices, as illustrated in Fig. 5.1. Instead of removing the rectifying effect, valve metal oxides are instead utilized in a fashion that always at least one is under the reverse bias to limit current. This mirrored configuration differs from the typical parallel-plate EWOD, which utilizes an insulating dielectric on only one plate.

#### 5.4 Anodization

For anodization (or anodic oxidation), the sample electrode and a counter electrode are immersed in a conducting electrolyte solution and a bias is applied between the two electrodes

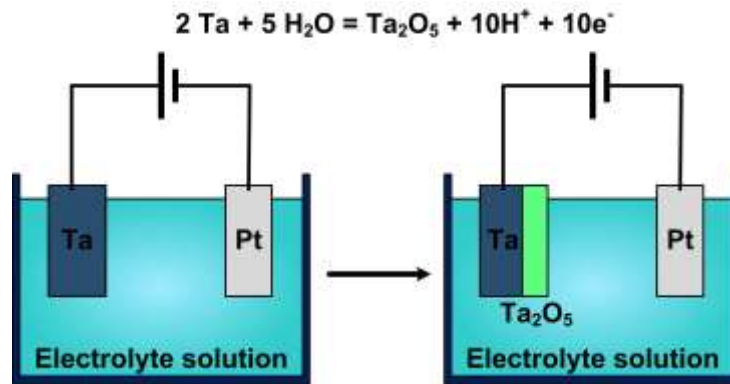


Figure 5.2: Anodization setup: platinum was used as a counter electrode and connected with the ground terminal of the power supply. The electrolyte solution was mixed during the process by a magnetic stirrer.

(Fig. 5.2). Oxidation occurs at the anode and reduction occurs at the cathode [128]. The sample electrode is connected as the anode (positively charged), where the applied electric field causes oxide growth from both the metal/oxide interface via inward migration of oxygen and the oxide/electrolyte solution interface via outward migration of metal [135].

The oxide thickness from anodization has been modeled as a linear function of the applied voltage [136], and it can be precisely controlled by the applied anodization voltage. However, the anodization constant (or proportionality constant of oxide thickness with respect to voltage) depends on the growth conditions (*e.g.*, electrolyte, temperature, pH) [128].

## **5.5 Testing the mirrored configuration of anodized dielectrics for EWOD**

### **5.5.1 Sample fabrication**

All of the samples were fabricated on clean glass slides (0.7 mm thick). For parallel-plate EWOD tests, 500 nm of Ta was sputter-coated on the glass as the EWOD electrodes, on which Ta<sub>2</sub>O<sub>5</sub>, silicon nitride, or silicon oxide was formed as the dielectric. Ground plates were also prepared by evaporating 20/200 nm of chrome/gold as the reference electrode for typical parallel-plate EWOD architecture.

Tantalum pentoxide dielectric was grown from tantalum electrodes by anodization in a room temperature 0.05 M solution of citric acid in DI water using a constant current step with current density of 0.1 mA/cm<sup>2</sup> (55 minutes) (Fig. 5.3). The constant current step was followed by a 1 hour constant voltage step with voltage of 50 V (for 83 nm thick Ta<sub>2</sub>O<sub>5</sub>) or 100 V (for 165 nm thick Ta<sub>2</sub>O<sub>5</sub>). On other samples intended for comparison, silicon oxide and silicon nitride were deposited onto tantalum electrodes at a thickness of 165 nm using PECVD. No dielectric

was deposited on the gold-coated ground plates.

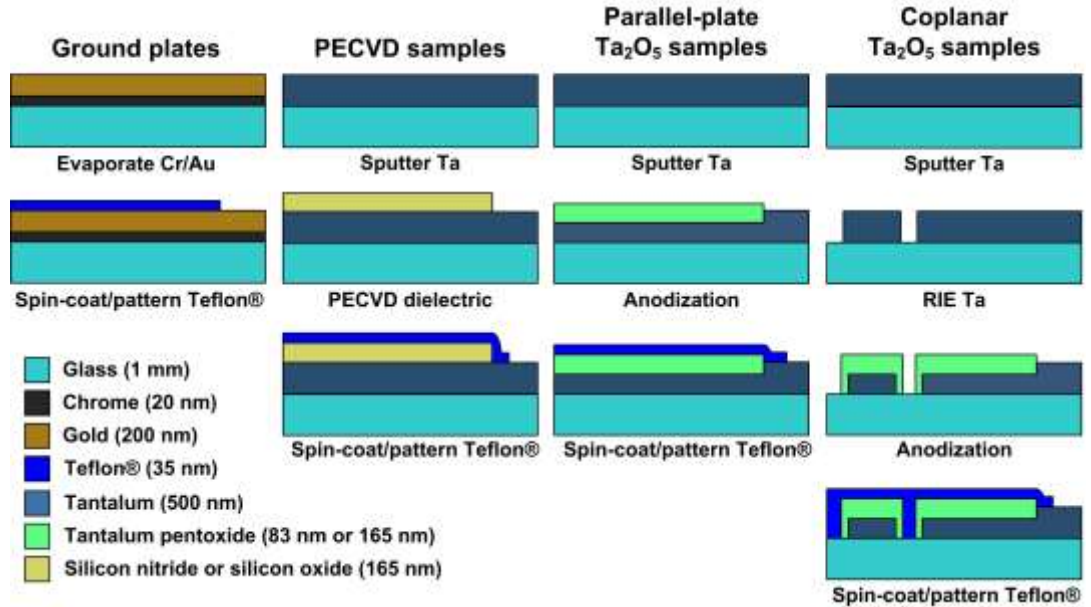


Figure 5.3: Fabrication process flow for samples to test and compare a mirrored configuration of valve metal oxide as an EWOD dielectric.

For coplanar EWOD tests, two different sets of electrodes were prepared. The first was to actuate sessile droplets to measure the contact angle changes [137], and the second consisted of two rows of square electrodes to move droplets side-to-side with sequential activation of neighboring electrodes (Fig. 5.4). The coplanar EWOD device fabrication began with 500 nm of sputtered tantalum on glass slides. The electrodes were patterned by photolithography with AZ 4620 photoresist (6.2  $\mu\text{m}$  thick, MicroChemicals GmbH, Germany) and dry-etched by RIE ( $\text{SF}_6$  gas, 40 mTorr, 35 V DC bias, 115 W forward RF power). Before anodization, photoresist was stripped using a solvent wash and  $\text{H}_2\text{SO}_4:\text{H}_2\text{O}_2$  (4:1) cleaning step. Tantalum pentoxide was anodized under the same conditions as parallel-plate samples with 0.05 M citric acid in DI water,

a constant current step of  $0.1 \text{ mA/cm}^2$  (55 minutes), and a 1 hour constant voltage step at 100 V. A hydrophobic layer of Teflon AF 2400® (35 nm) was spin-coated onto all of the samples and patterned by lift-off to expose bare metal for electrical contact.

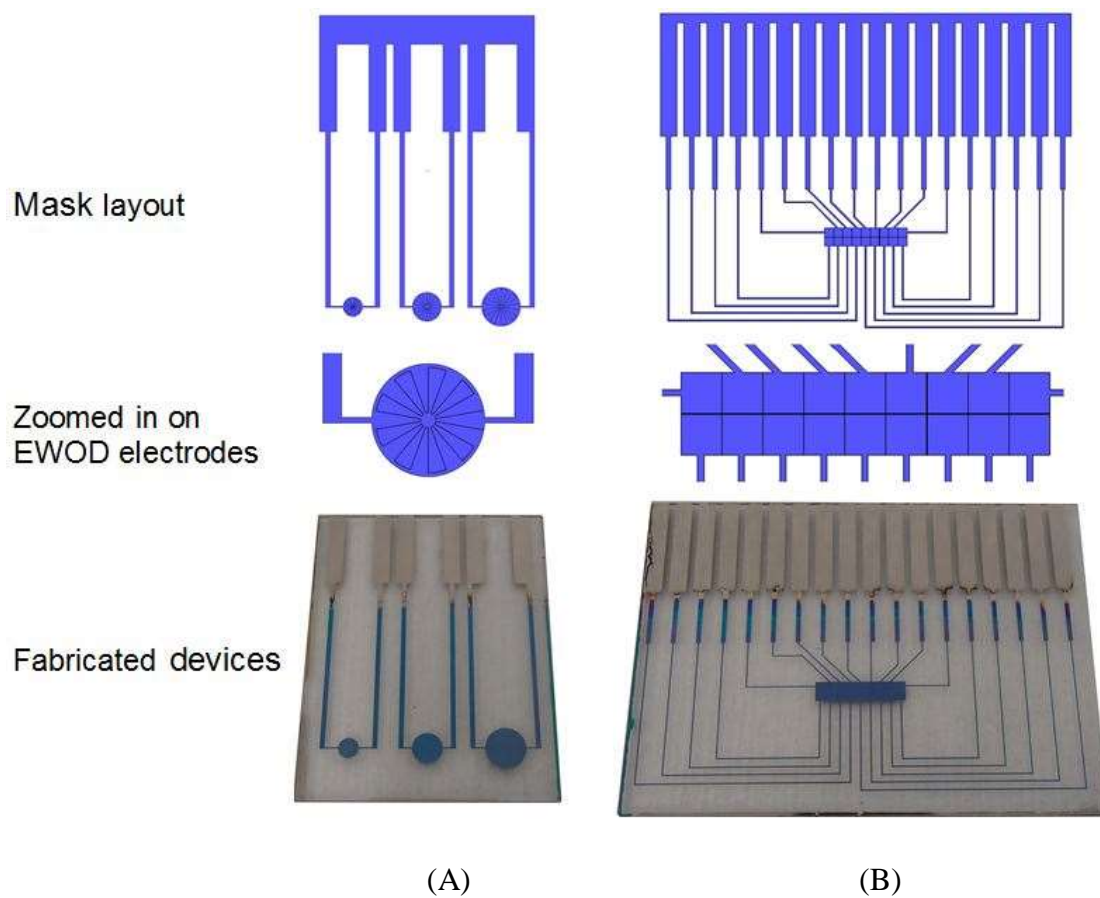


Figure 5.4: Coplanar EWOD devices with anodized tantalum pentoxide. (A) Sessile droplet actuation design adapted from Yi et al. [137]. (B) Two rows of square electrodes for moving droplets side-to-side.

### 5.5.2 Experimental setup

In the typical parallel-plate EWOD configuration, a dielectric is used on the main plate with actuation electrodes but not on the ground plate with a reference electrode other than the hydrophobic topcoat. In the mirrored configuration for parallel-plate EWOD, both plates include a dielectric ( $\text{Ta}_2\text{O}_5$  was used for testing). In the mirrored configuration for coplanar EWOD,  $\text{Ta}_2\text{O}_5$  insulated both actuation and reference electrodes on a single plate.

Test droplets consisted of a 1:1 mixture of glycerin and KCl in water standard solution in order to prevent evaporation (with glycerin) and ensure conductivity (with KCl). The chloride from KCl is also useful for testing because it has been shown to exacerbate dielectric failure in EWOD [138]. Sessile droplets were used for contact angle measurement and also for coplanar EWOD testing. For parallel-plate current leakage tests, droplets were sandwiched between the plates with a gap of 70  $\mu\text{m}$ .

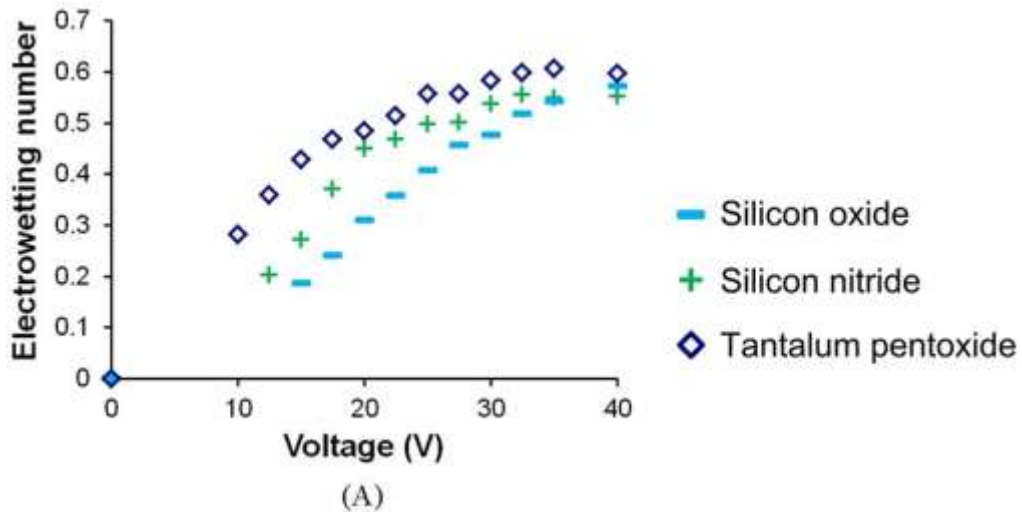
EWOD voltage actuation was supplied by a sourcemeter (Keithley 2425) and leakage current was measured with an electrometer (Keithley 6514). Both Keithley instruments were connected to a computer with a GPIB controller (GPIB-USB-HS, National Instruments) for control and data recording. For high frequency cycling tests, photoMOS relays (AQW610EH PhotoMos relay, Panasonic) controlled through a DAQ (NI USB-6255, National Instruments) were used to switch electrical connections to the plates.

Current leakage was measured for both breakdown tests and lifetime tests. In breakdown tests, currents were measured with respect to applied electric field. In lifetime tests, current leakage was compared for three types of biases: forward bias, reverse bias, and alternating bias. For all of the biases tested in the lifetime test, 1 second actuation up to 35 V was alternated with

1 second of 0 V, i.e., 0.5 Hz, for 1000 cycles. Contact angles were measured using a contact angle measurement program with images of the droplet during EWOD actuation captured through a CCD camera (PixeLink, model PL B742U).

### 5.5.3 Results for parallel-plate EWOD

In measurements of contact angle change with applied voltage (Fig. 5.5), increased actuation was observed with  $Ta_2O_5$  before contact angle saturation (at  $\sim 30$  V). The increased actuation compared to silicon oxide and silicon nitride at voltages less than 30 V was expected, because of the significantly higher dielectric constant of  $Ta_2O_5$  (21-28) compared to silicon oxide (4-6) and silicon nitride ( $\sim 8$ ) [125, 128]. Beyond saturation voltage, the silicon oxide current leakage increased significantly compared to that of silicon nitride and  $Ta_2O_5$ .





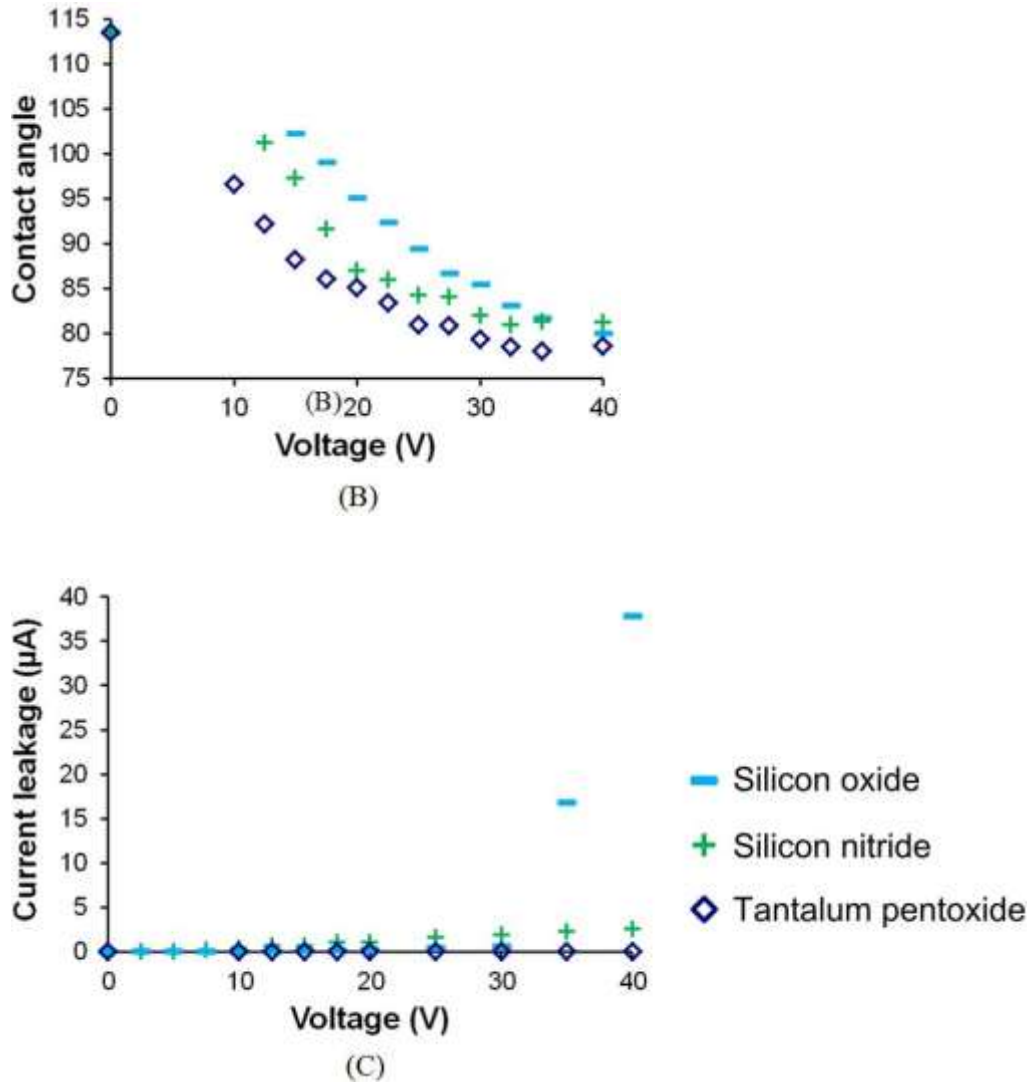


Figure 5.5: Comparison of measured EWOD actuation (contact angle change) and current leakage for an applied voltage with three different dielectrics: PECVD silicon nitride (+), PECVD silicon oxide (-), and anodized tantalum pentoxide ( $\Delta$ ). All of the dielectrics were 165 nm thick. The dimensionless electrowetting number  $E_w$  expresses reduction of interfacial energy of the solid-liquid interface with applied electric field [41]. A larger  $E_w$  corresponds to stronger electrowetting actuation. Tantalum pentoxide shows stronger electrowetting effect and less current leakage, corroborating previous reports [129].

In breakdown tests, the measured leakage currents were low for the Ta<sub>2</sub>O<sub>5</sub> samples, but climbed significantly for silicon oxide samples once the applied field increased past 30 MV/m (Fig. 5.6). Silicon nitride samples broke down beyond 425 MV/m. Mirrored Ta<sub>2</sub>O<sub>5</sub> samples of the same dielectric thickness broke down at a similar electric field, but with less current leakage. Current leakage for the forward biased Ta<sub>2</sub>O<sub>5</sub> was consistently higher compared with the reverse biased Ta<sub>2</sub>O<sub>5</sub>. Mirrored configuration samples were made with half the thickness (83 nm) of Ta<sub>2</sub>O<sub>5</sub> on each plate so that the total dielectric thickness was comparable to that on the test samples (165 nm) used in the typical parallel-plate configuration. In the mirrored configuration samples with half thickness on each plate, current leakage nearly matched that of the full thickness Ta<sub>2</sub>O<sub>5</sub> samples under reverse bias. The lowest current leakage was measured for Ta<sub>2</sub>O<sub>5</sub> in a mirrored configuration with a full 165 nm thickness on each plate, in which case one half of the externally applied voltage is applied to the 165 nm thick dielectric.

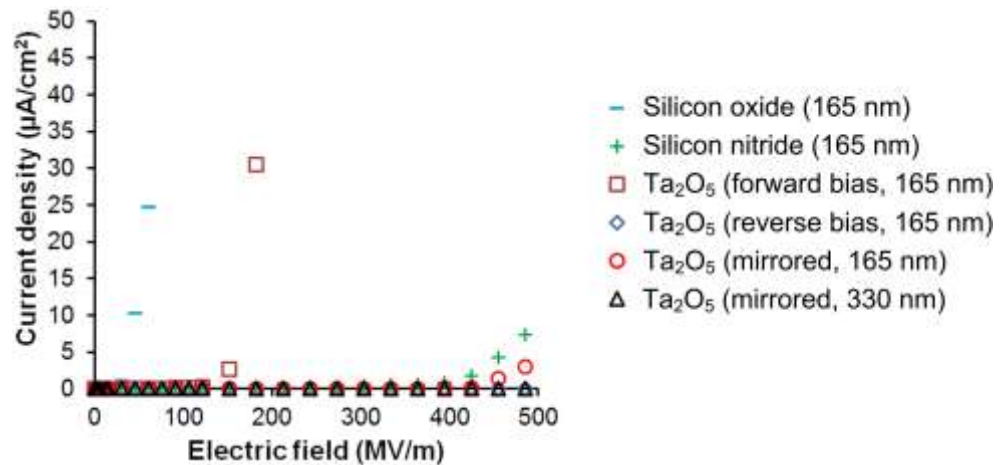


Figure 5.6: Current leakage measured as a function of electric field across typical EWOD and mirrored EWOD devices. The dielectrics were 165 nm thick unless specified. Tantalum pentoxide dielectrics had low current leakage compared with silicon oxide dielectric when it was under reverse bias or in a mirrored configuration.

The cumulative damaging effect of forward bias actuation was seen clearly in lifetime tests. Under forward bias (Fig. 5.7A), leakage current climbed over repeated cycles, but the leakage current increase was not steady as electrolysis bubbles moved the droplet. For reverse bias (Fig. 5.7B), the leakage current was expected to decrease with repeated voltage cycling (as a result of self-healing [127, 139]). However, the leakage current was too low to measure a noticeable decrease. For the 0.5 Hz alternating bias in a mirrored-configuration, no significant current change was measured. For the typical EWOD configuration under an 0.5 Hz alternating bias, significant current leaked during the cycle periods under forward bias but not during the reverse bias periods (Fig. 5.8).

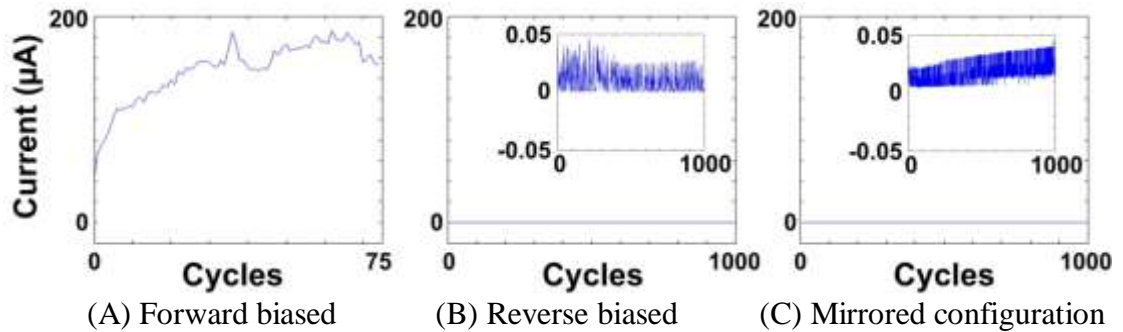


Figure 5.7: Measurement of current leakage under cycles of voltage pulse (0.5 Hz; 50% duty cycle) applied to a droplet on a 165 nm thick tantalum pentoxide. (A) The leakage current was significant for forward bias. (B) The leakage current was negligible for reverse bias. (C) For the mirrored configuration, the leakage current was negligible for both biases as well as an alternating bias.

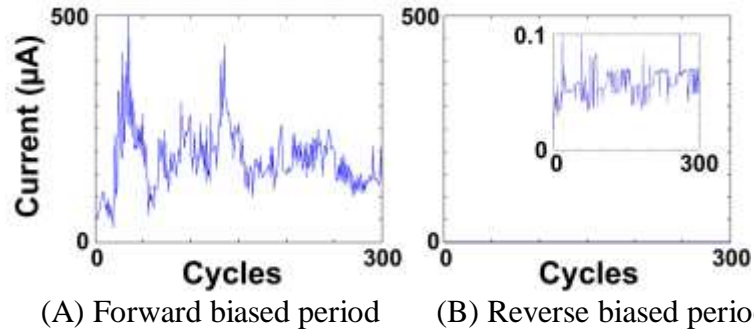


Figure 5.8: Measurement of current leakage under cycles of 0.5 Hz AC voltage applied to a droplet on a 165 nm thick tantalum pentoxide. (A) The leakage current was significant for periods under forward bias. (B) The leakage current was negligible for periods under reverse bias.

By using anodized dielectrics in a mirrored configuration, current leakage was limited during actuation of a parallel-plate EWOD device, regardless of voltage bias. Fabrication of the mirrored configuration is simpler than adding a sputtering step to deposit a valve metal oxide [129], although its use of an equal dielectric thickness on both plates is somewhat different from typical EWOD devices. In most parallel plate EWOD devices, the main dielectric of a necessary thickness is deposited entirely on the plate with patterned EWOD electrodes for simpler fabrication. The dielectric on the opposite plate is generally much thinner, and in some cases only consists of a hydrophobic topcoat.

#### **5.5.4 Results for parallel-plate EWOD**

In the case of coplanar EWOD devices, where both the actuation and reference electrodes are fabricated on the same plate [137], a mirrored configuration was incorporated with anodization of only a single plate. Because the valve metal oxide dielectric would still cover both the actuation and ground electrodes, its rectifying current effect should also oppose itself. The use of a mirrored configuration of anodized dielectrics for coplanar EWOD devices was tested by measuring current leakage during actuation.

In sessile droplet actuation with a 5  $\mu\text{L}$  droplet, current leakage was less than 15 nA for approximately  $20^\circ$  contact angle change using 25 V (Fig. 5.9). In a separate coplanar design with neighboring square electrodes, a 2.5  $\mu\text{L}$  droplet was moved across the electrodes with 25 V and an average current leakage during the actuation of 55 nA (Fig. 5.10).

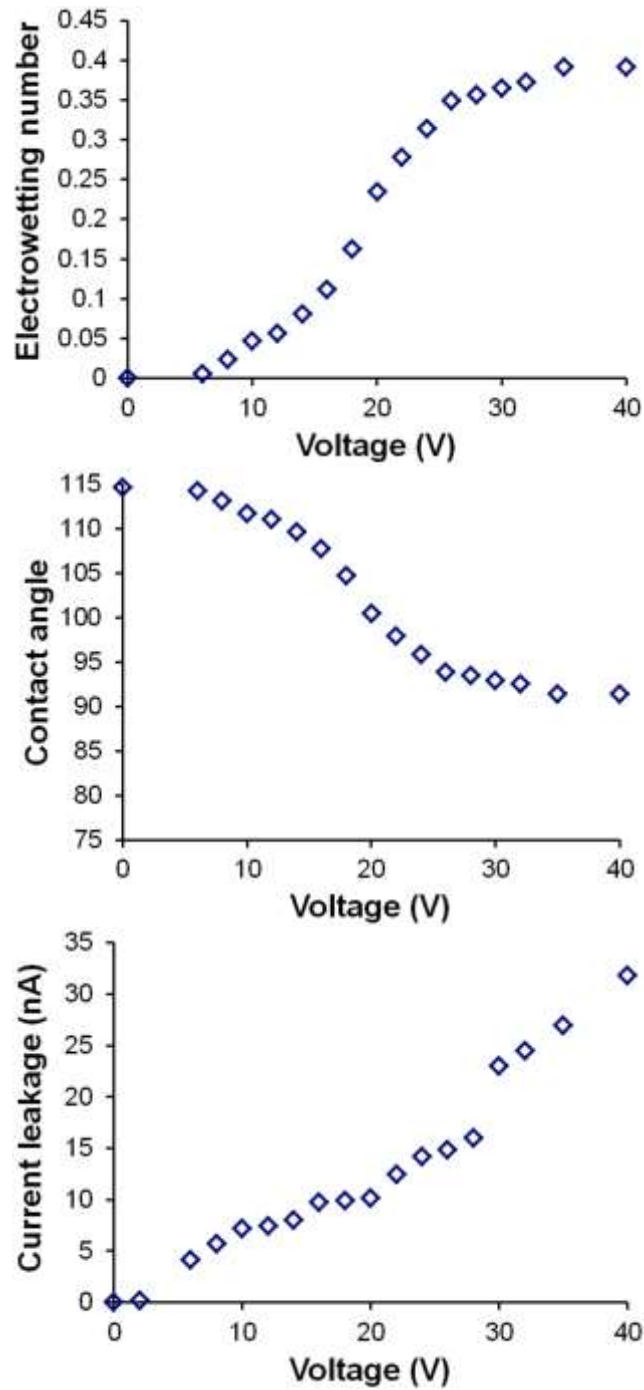


Figure 5.9: Comparison of measured EWOD actuation (contact angle change) and current leakage for an applied voltage with 165 nm Ta<sub>2</sub>O<sub>5</sub> grown over coplanar EWOD electrodes.

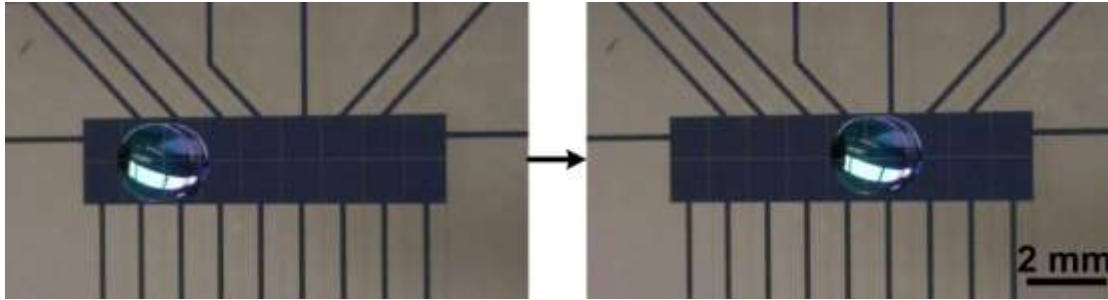


Figure 5.10: Transportation of 2.5  $\mu\text{L}$  droplet on a coplanar EWOD device with 165 nm thick tantalum pentoxide dielectric, using 25  $V_{\text{DC}}$  actuation signals.

Compared with the parallel-plate configuration, the current leakage for the coplanar EWOD was relatively high (considering that 165 nm of  $\text{Ta}_2\text{O}_5$  covers both the actuation and ground electrodes as in the parallel-plate mirrored configuration with full thickness on both plates). The relatively high current leakage compared to parallel-plate devices may be due to incomplete insulation along the side edges of tantalum electrodes during the anodization process as the electric field for anodized growth was applied perpendicular to the surface, while EWOD actuation involves an electric field parallel to the surface applied along gaps between activated and grounded electrodes. In such a case, an additional anodization step using neighboring electrodes as counter electrodes for additional growth of  $\text{Ta}_2\text{O}_5$  may improve sidewall insulation.

## 5.6 Summary

The mirrored configuration for valve metal oxide dielectrics was tested using  $\text{Ta}_2\text{O}_5$  in both parallel-plate and coplanar EWOD devices. In lifetime tests, the mirrored configuration had negligible current leakage over 1,000 actuation cycles. In breakdown tests, the polarity effect

was demonstrated when Ta<sub>2</sub>O<sub>5</sub> covered one plate, *i.e.*, not a mirrored configuration, but not noticeable when Ta<sub>2</sub>O<sub>5</sub> covered both plates in a mirrored configuration. In comparisons with PECVD silicon nitride and silicon oxide, current leakage was lower across the Ta<sub>2</sub>O<sub>5</sub> dielectrics. Droplet movement was demonstrated on an open EWOD plate, which has coplanar electrodes covered with Ta<sub>2</sub>O<sub>5</sub>, while exhibiting little current leakage as expected from the mirrored configuration.



## CHAPTER 6: SUMMARY AND CONCLUSIONS

This dissertation was focused on developing an EWOD radiosynthesizer device to produce a variety of PET radiotracers. The purpose is to address a current need of PET imaging centers to have access to radiotracers that are most suitable for their studies. Developments are being made to lower costs, reduce infrastructure, and increase simplicity of PET tracer production so that imaging centers can produce dose-on-demand radiotracers of their choice, as long as [ $^{18}\text{F}$ ]fluoride is provided.

There are many reasons to perform radiotracer synthesis using microfluidics, such as the already low volumes used in conventional radiochemistry, reduced reagent consumption, and improved reaction efficiency. Of the microfluidic platforms, EWOD is unique because its open-air configuration is not only conducive to solvent exchange steps required with [ $^{18}\text{F}$ ]fluoride labelling chemistry but it also enables easy reconfiguration of fluid paths through electrical signals alone (without mechanical valves or pumps).

EWOD actuation is able to manipulate the solutions and fluids typically used in radiochemistry procedures, and when heaters are incorporated into its electrodes, an EWOD device can perform concentration, solvent exchange, and reaction steps for radiosynthesis. A reactor site for the EWOD radiosynthesizer was designed to have four concentric multifunctional electrodes that could be used for EWOD actuation, resistive heating, and thermistor temperature sensing. The concentric heating sites enabled more accurate temperature control for a large range of volumes and were particularly useful in heating steps where droplet size reduced as solvent was evaporated.

A single design of the EWOD radiosynthesizer was used for production of four different PET tracers (a sugar, a DNA nucleoside, a protein-labelling agent, and a neurotransmitter) with yields that were comparable to or higher than conventional approaches. The EWOD radiosynthesizer also has potential to produce radiotracers with unprecedented high specific radioactivity. The parameters and factors that influence specific activity need to be investigated further, but could have a significant impact in cases where the radiotracer's intended target can be easily saturated or when the radiotracer itself is toxic.

Two methods to incorporate purification steps onto the EWOD radiosynthesizer were investigated. The first used a functionalized dielectric surface to remove impurities from droplets. Although it was successful in removing fluoride, functionalizing a surface to remove other impurities requires specific changes in EWOD device fabrication that are dependent on the intended radiotracer. A second method was developed more in line with our overall goal for a single EWOD device that can produce diverse radiotracers without any changes except in the loaded reagents and applied electrical signals. In the second method, a filter site was added on the cover plate, so that SPE sorbents particles could be loaded onto the chip, mixed with its intended targets, and then separated from the droplet by mechanical filtration. Because this method can separate the radiotracer from radioactive fluoride, it has potential to be used with Cerenkov imaging for measurement of fluorination yield. Further work should investigate its use as an online measurement of fluorination yield and whether accuracy can be improved by taking Cerenkov images before and after purification to remove influence of SPE sorbents on Cerenkov quantification.

In an effort to achieve low cost but high performing dielectric layers for EWOD devices, valve metal oxides in a mirrored configuration was proposed and tested. Tantalum pentoxide was electrochemically grown on tantalum EWOD electrodes by anodization. In testing of tantalum pentoxide in typical parallel-plate EWOD configuration, mirrored parallel-plate configuration, and coplanar EWOD, the tantalum pentoxide limited current leakage under all biases tested for both the mirrored parallel-plate configuration and coplanar EWOD. Because the conduction mechanism through valve metal oxides depend on the conditions in which the oxide is formed and processing before and after oxide growth, additional treatments may be taken to improve the dielectric properties and should be investigated.

## REFERENCES

- [1] M. E. Phelps, "Positron emission tomography provides molecular imaging of biological processes," *Proceedings of the National Academy of Sciences of the United States of America*, vol. 97, pp. 9226-9233, 2000.
- [2] K. Serdons, A. Verbruggen and G. M. Bormans, "Developing new molecular imaging probes for PET," *Molecular Imaging*, vol. 48, pp. 104-111, 2009.
- [3] S. S. Gambhir, "Molecular imaging of cancer with positron emission tomography," *Nature Reviews Cancer*, vol. 2, pp. 683-693, 2002.
- [4] M. R. Javed, S. Chen, H.-K. Kim, L. Wei, J. Czernin, C.-J. Kim, R. M. van Dam and P. Y. Keng, "Efficient radiosynthesis of 3'-deoxy-3'-18F-fluorothymidine using electrowetting-on-dielectric digital microfluidic chip," *Journal of Nuclear Medicine*, vol. 55, pp. 321-328, 2014.
- [5] A. M. Elizarov, "Microreactors for radiopharmaceutical synthesis," *Lab on a Chip*, vol. 9, pp. 1326-133, 2009.
- [6] P. W. Miller, A. J. deMello and A. D. Gee, "Application of microfluidics to the ultra-rapid preparation of fluorine-18 labelled compounds," *Current Radiopharmaceuticals*, vol. 3, pp. 254-262, 2010.
- [7] S. Vallabhajosula, "18F-labeled positron emission tomographic radiopharmaceuticals in oncology: an overview of radiochemistry and mechanisms of tumor localization," *Seminars in Nuclear Medicine*, vol. 37, pp. 400-419, 2007.
- [8] L. Cai, S. Lu and V. W. Pike, "Chemistry with [18F]fluoride ion," *European Journal of Organic Chemistry*, vol. 17, pp. 2853-2873, 2008.
- [9] R. Wong, R. Iwata, H. Saiki, S. Furomoto, Y. Ishikawa and E. Ozeki, "Reactivity of electrochemically concentrated anhydrous [18F]fluoride for microfluidic radiosynthesis of 18F-labeled compounds," *Applied Radiation and Isotopes*, vol. 70, pp. 193-199, 2012.
- [10] R. Iwata, Radiosynthesis database of PET probes, Japan: National Institute of Radiological Sciences, 2013.
- [11] O. Couturier, A. Luxen, J.-F. Chatal, J.-P. Vuillez, P. Rigo and R. Hustinx, "Fluorinated tracers for imaging cancer with positron emission tomography," *European Journal of Nuclear Medicine and Molecular Imaging*, vol. 34, pp. 1182-1206, 2004.

- [12] C. Hsieh, *Positron Emission Tomography - Current Clinical and Research Aspects*, New York: InTech, 2012, pp. 153-182.
- [13] R. Krasikova, "PET radiochemistry automation: state of the art and future trends in  $^{18}\text{F}$ -nucleophilic fluorination," *Current Organic Chemistry*, vol. 17, pp. 2097-2107, 2013.
- [14] C. Van de Wiele, C. Lahorte, W. Oyen, O. Boermen, I. Goethals, G. Slegers and R. A. Dierckx, "Nuclear medicine imaging to predict response to radiotherapy: a review," *International Journal of Radiation Oncology, Biology, Physics*, vol. 55, pp. 5-15, 2003.
- [15] E. E. Kim, M.-C. Lee, T. Inoue and W.-H. Wong, *Clinical PET and PET/CT: Principles and Applications*, New York: Springer, 2013.
- [16] S. Vhallabhajosula, *Molecular Imaging: Radiopharmaceuticals for PET and SPECT*, New York: Springer, 2009.
- [17] R. Merrifield, J. Stewart and N. Jernberg, "Instrument for automated synthesis of peptides," *Analytical Chemistry*, vol. 38, pp. 1904-1914, 1966.
- [18] M. H. Caruthers, "Gene synthesis machines: DNA chemistry and its uses," *Science*, vol. 230, pp. 281-285, 1985.
- [19] M. J. Welch and C. S. Redvanly, *Handbook of Radiopharmaceuticals: Radiochemistry and Applications*, West Sussex, England: John Wiley & Sons, Inc., 2003.
- [20] P. A. Schubiger, L. Lehmann and M. Friebe, *PET Chemistry: The driving force in molecular imaging*, New York: Springer, 2007.
- [21] J. S. Fowler, R. MacGregor, A. Wolf, A. Farrell, K. Karlstrom and T. Ruth, "A shielded synthesis system for production of 2-deoxy-2- $^{18}\text{F}$ fluoro-D-glucose," *Journal of Nuclear Medicine*, vol. 22, pp. 376-380, 1981.
- [22] J. R. Barrio, N. MacDonald, J. G.D. Robinson, A. Najafi, J. Cook and D. Kuhl, "Remote, semiautomated production of F-18-labeled 2-deoxy-2-fluoro-D-glucose," *Journal of Nuclear Medicine*, vol. 22, pp. 372-375, 1981.
- [23] R. Iwata, T. Ido, T. Takahashi and M. Monma, "Automated synthesis system for production of 2-deoxy-2- $^{18}\text{F}$ fluoro-D-glucose with computer control," *International Journal of Applied Radiation and Isotopes*, vol. 35, pp. 445-454, 1984.
- [24] M. Monma, K. Ishiwata, R. Iwata and T. Ido, "Automated synthesis system for production of  $^{11}\text{C}$ -glucose," *Radioisotopes*, vol. 33, pp. 15-20, 1984.

- [25] H. C. Padgett, D. G. Schmidt, A. Luxen, G. T. Bida, N. Satyamurthy and J. R. Barrio, "Computer-controlled radiochemical synthesis: a chemistry process control unit for automated production of radiochemicals," *International Journal of Radiation Applications and Instrumentation. Part A. Applied Radiation and Isotopes*, vol. 40, pp. 443-445, 1989.
- [26] E. Webster, M. S. Haka, P. Gutierrez, K. Young and S. Zigler, "A short synopsis on the cleaning validation of the Siemens Explora GN and LC units," *Journal of Labelled Compounds and Radiopharmaceuticals*, vol. 54, p. S438, 2011.
- [27] W. Wadsak and M. Mitterhauser, "Basics and principles of radiopharmaceuticals for PET/CT," *European Journal of Radiology*, vol. 73, pp. 461-469, 2010.
- [28] G. Pascali, P. Watts and P. A. Salvadori, "Microfluidics in radiopharmaceutical chemistry," *Nuclear Medicine and Biology*, vol. 40, pp. 776-787, 2013.
- [29] K. S. Elvira, X. C. Solvas, R. C. R. Wooten and A. J. deMello, "The past, present and potential for microfluidic reactor technology in chemical synthesis," *Nature Chemistry*, vol. 5, pp. 905-915, 2013.
- [30] C. Rensch, A. Jackson, S. Lindner, R. Salvamoser, V. Samper, S. Riese, P. Bartenstein, C. Wängler and B. Wängler, "Microfluidics: A Groundbreaking Technology for PET Tracer Production," *Molecules*, vol. 18, pp. 7930-7956, 2013.
- [31] V. Arima, G. Pascali, O. Lade, H. R. Kretchmer, I. Bernsdorf, V. Hammond, P. Watts, F. D. Leonardis, M. D. Tarn, N. Pamme, B. Z. Cvetkovic, P. S. Dittrich, N. Vasovic, R. Duane, A. Jaksic, A. Zacheo, A. Zizzari, L. Marra, E. Perrone, P. A. Salvadori and R. Rinaldi, "Radiochemistry on chip: towards dose-on-demand synthesis of PET radiopharmaceuticals," *Lab on a Chip*, vol. 13, pp. 2328-2336, 2013.
- [32] A. Lebedev, R. Miraghai, K. Kotta, C. E. Ball, J. Zhang, M. S. Buchsbaum, H. C. Kolb and A. Elizarov, "Batch-reactor microfluidic device: first human use of a microfluidically produced PET radiotracer," *Lab on a Chip*, vol. 13, pp. 136-145, 2013.
- [33] G. Pascali, A. Berton, M. DeSimone, N. Wyatt, L. Matesic, I. Greguric and P. A. Salvadori, "Hardware and software modifications on the Advion NanoTek microfluidic platform to extend flexibility for radiochemical synthesis," *Applied Radiation and Isotopes*, vol. 84, pp. 40-47, 2014.
- [34] H.-J. Wester, B. W. Schoultz, C. Hultsch and G. Henriksen, "Fast and repetitive in-capillary production of [<sup>18</sup>F]FDG," *European Journal of Nuclear Medicine and Molecular Imaging*, vol. 36, pp. 653-658, 2009.

- [35] S. A. M. W. van de Broek, R. Beckeremail, K. Kochemail and P. J. Nieuwland, "Microreactor technology: Real-Time Flow Measurements in Organic Synthesis," *Micromachines*, vol. 3, pp. 244-254, 2012.
- [36] S. Lu, A. M. Giamis and V. W. Pike, "Synthesis of [<sup>18</sup>F]fallypride in a micro-reactor: rapid optimization and multiple-production in small doses for micro-PET studies," *Current Radiopharmaceuticals*, vol. 2, pp. 49-55, 2009.
- [37] M. Yu, J. Matteo, D. Townsend and R. Nutt, "Rapid microfluidic production of PET biomarker [<sup>18</sup>F]FDG," *Journal of Nuclear Medicine*, vol. 47, p. 159P, 2006.
- [38] H. Moon, S. K. Cho, R. L. Garrell and C.-J. Kim, "Low voltage electrowetting-on-dielectric," *Journal of Applied Physics*, vol. 92, pp. 4080-4087, 2002.
- [39] K. Choi, A. H. Ng, R. Fobel and A. R. Wheeler, "Digital Microfluidics," *Annual Review of Analytical Chemistry*, vol. 5, pp. 413-440, 2012.
- [40] M. J. Jebrail, M. S. Bartsch and K. D. Patel, "Digital microfluidics: a versatile tool for applications in chemistry, biology, and medicine," *Lab on a Chip*, vol. 12, pp. 2452-2463, 2012.
- [41] W. C. Nelson and C.-J. Kim, "Droplet actuation by electrowetting-on-dielectric (EWOD): A Review," *Journal of Adhesion Science and Technology*, vol. 26, pp. 1747-1771, 2012.
- [42] B. Berge, "Électrocapillarité et mouillage de films isolants par l'eau (Electrocapillarity and wetting of insulator films by water)," *Comptes rendus de l'Académie des sciences, Série II*, vol. 317, pp. 157-163, 1993.
- [43] G. Beni and S. Hackwood, "Electrowetting displays," *Applied Physics Letters*, vol. 22, pp. 372-375, 1981.
- [44] B. Berge and J. Peseux, "Variable focal lens controlled by an external voltage: an application of electrowetting," *European Physical Journal E*, vol. 2000, pp. 159-163, 2000.
- [45] B. Hendriks, S. Kuiper, M. v. As, C. Renders and T. Tukker, "Electrowetting-based variable-focus lens for miniature systems," *Optical Review*, vol. 12, pp. 255-259, 2005.
- [46] J. Gong, G. Cha, Y. S. Ju and C.-J. Kim, "Thermal switches based on coplanar EWOD for satellite thermal control," in *Proceedings of International Conference on Micro Electro Mechanical Systems (MEMS)*, Tucson, AZ, pp. 848-851, 2008.

- [47] P. Sen and C.-J. Kim, "A fast liquid-metal droplet microswitch using EWOD-driven contact-line sliding," *Journal of Microelectromechanical Systems*, vol. 18, pp. 174-185, 2009.
- [48] T. Krupenkin and J. A. Taylor, "Reverse electrowetting as a new approach to high-power energy harvesting," *Nature Communications*, vol. 2, p. 448, 2011.
- [49] A. Banpurkar, M. Duits, D. van den Ende and F. Mugele, "Electrowetting of complex fluids: perspectives for rheometry on chip," *Langmuir*, vol. 25, pp. 1245-1252, 2009.
- [50] W. Nelson, P. Kavehpour and C.-J. Kim, "A micro extensional filament rheometer enabled by EWOD," in *Proceedings of International Conference on Micro Electro Mechanical Systems (MEMS)*, Hong Kong, China, pp. 75-78, 2010.
- [51] M. J. Jebrail, N. Assem, J. M. Mudrik, M. D. Dryden, K. Lin, A. K. Yudin and A. R. Wheeler, "Combinatorial Synthesis of Peptidomimetics Using Digital Microfluidics," *Journal of Flow Chemistry*, 2012, 2, 103-107, vol. 2, pp. 103-107, 2012.
- [52] H. Moon, A. R. Wheeler, R. L. Garrell, J. A. Loo and C.-J. Kim, "An integrated digital microfluidic chip for multiplexed proteomic sample preparation and analysis by MALDI-MS," *Lab on a Chip*, vol. 6, pp. 1213-1219, 2006.
- [53] A. E. Kirby and A. R. Wheeler, "Digital microfluidics: an emerging sample preparation platform for mass spectrometry," *Analytical Chemistry*, vol. 85, pp. 6178-6184, 2013.
- [54] L. Zhua, Y. Fenga, X. Yea, J. Fenga, Y. Wua and Z. Zhou, "An ELISA chip based on an EWOD microfluidic platform," *Journal of Adhesion Science and Technology*, vol. 26, pp. 2113-2124, 2012.
- [55] S.-K. Fan, P.-W. Huang, T.-T. Wanga and Y.-H. Peng, "Cross-scale electric manipulations of cells and droplets by frequency-modulated dielectrophoresis and electrowetting," *Lab on a Chip*, vol. 8, pp. 1325-1331, 2008.
- [56] J. Lee, H. Moon, J. Fowler, T. Schoellhammer and C.-J. Kim, "Electrowetting and electrowetting-on-dielectric for microscale liquid handling," *Sensors and Actuators A: Physical*, vol. 95, pp. 259-268, 2002.
- [57] S. Chen, R. Javed, J. Lei, H.-K. Kim, G. Flores, R. M. van Dam, P. Y. Keng and C.-J. Kim, "Synthesis of diverse tracers on EWOD microdevice for positron emission tomography (PET)," in *Technical Digest of Solid-State Sensor and Actuator Workshop*, Hilton Head Island, SC, United States, pp.189-192, 2012.
- [58] M. R. Javed, S. Chen, J. Lei, J. Collins, M. Sergeev, H.-K. Kim, C.-J. Kim, R. M. van Dam and P. Y. Keng, "High yield and high specific activity synthesis of [ $^{18}\text{F}$ ]fallypride in a



- batch microfluidic reactor for micro-PET imaging," *Chemical Communications*, vol. 50, pp. 1192-1194, 2014.
- [59] C. Rensch, B. Waengler, A. Yaroshenko, V. Samper, M. Baller, N. Heumesser, J. Ulin, S. Riese and G. Resichl, "Microfluidic reactor geometries for radiolysis reduction in radiopharmaceuticals," *Applied Radiation and Isotopes*, vol. 70, pp. 1691-1697, 2012.
- [60] P. Y. Keng, S. Chen, H. Ding, S. Sadeghi, G. J. Shah, A. Dooraghi, M. E. Phelps, N. Satyamurthy, A. F. Chatziioannou, C.-J. Kim and R. M. van Dam, "Micro-chemical synthesis of molecular probes on an electronic microfluidic device," *Proceedings of the National Academy of Sciences of the United States of America*, vol. 109, pp. 690-695, 2012.
- [61] S. Chen, M. R. Javed, H.-K. Kim, J. Lei, M. Lazari, G. J. Shah, R. M. van Dam, P.-Y. Keng and C.-J. Kim, "Radiolabelling diverse positron emission tomography (PET) tracers using a single digital microfluidic reactor chip," *Lab on a Chip*, vol. 14, pp. 902-910, 2014.
- [62] W. Wadsak and M. Mitterhauser, "Basics and principles of radiopharmaceuticals for PET/CT," *European Journal of Radiology*, vol. 73, pp. 461-469, 2010.
- [63] G. Maltezos, M. Johnston, K. Taganov, C. Srichantaratsamee, J. Gormon, D. Baltimore, W. Chantratita and A. Scherer, "Exploring the limits of ultrafast polymerase chain reaction using liquid for thermal heat exchange: A proof of principle," *Applied Physics Letters*, vol. 97, p. 264101, 2010.
- [64] W. Ren, J. Perumal, J. Wang, H. Wang, S. Sharma and D.-P. Kim, "Whole ceramic-like microreactors from inorganic polymers for high temperature or/and high pressure chemical syntheses," *Lab on a Chip*, 2014, 14, 779-786, vol. 14, pp. 779-786, 2014.
- [65] K. Domansky, W. Inman, J. Serdy, A. Dash, M. H. M. Lim and L. G. Griffith, "Perfused Multiwell plate for 3D liver tissue engineering," *Lab on a Chip*, vol. 10, pp. 51-58, 2010.
- [66] M. N. Slyadnev, Y. Tanaka, M. Tokeshi and T. Kitamori, "Photothermal temperature control of a chemical reaction on a microchip using an infrared diode laser," *Analytical Chemistry*, vol. 73, pp. 4037-4044, 2001.
- [67] G. Maltezos, M. Johnston and A. Scherer, "Thermal management in microfluidics using micro-Peltier junctions," *Applied Physics Letters*, vol. 87, p. 154105, 2005.

- [68] Y.-H. Chang, G.-B. Lee, F.-C. Huang, Y.-Y. Chen and J.-L. Lin, "Integrated polymerase chain reaction chips utilizing digital microfluidics," *Biomedical Microdevices*, vol. 8, pp. 215-225, 2006.
- [69] A. J. L. Morgan, J. Naylor, S. Gooding, C. John, O. Squires, J. Lees, D. A. Barrow and A. Porch, "Efficient microwave heating of microfluidic systems," *Sensors and Actuators B: Chemical*, vol. 181, pp. 904-909, 2013.
- [70] R. M. Guijt, A. Dodge, G. W. K. van Dedem, N. F. d. Rooij and E. Verpoorte, "Chemical and physical processes for integrated temperature control in microfluidic devices," *Lab on a Chip*, vol. 3, pp. 1-4, 2003.
- [71] T. B. Jones, "Liquid dielectrophoresis on the microscale," *Journal of Electrostatics*, Vols. 51-52, pp. 290-299, 2001.
- [72] D. Issadore, K. J. Humphry, K. A. Brown, L. Sandberg, D. A. Weitz and R. M. Westervelt, "Microwave dielectric heating of drops in microfluidic devices," *Lab on a Chip*, vol. 9, pp. 1701-1706, 2009.
- [73] J.-H. Wei, W.-S. Hsu and S.-K. Fan, "Realizing temperature-controlled digital microfluidic chips with versatile microelectrodes," in *2nd IEEE International Conference on Nano/Micro Engineered and Molecular Systems*, Bangkok, Thailand, pp. 981-984, 2007.
- [74] W. Nelson, I. Peng, J. A. Loo, R. L. Garrell and C.-J. Kim, "An EWOD droplet microfluidic chip with integrated local temperature control for multiplex proteomics," in *Proceedings of IEEE International Conference on Micro Electro Mechanical Systems*, Sorrento, Italy, pp. 280-283, 2009.
- [75] W. C. Nelson, I. Peng, G.-A. Lee, J. A. Loo, R. L. Garrell and C.-J. Kim, "Incubated protein reduction and digestion on an EWOD digital microfluidic chip for MALDI-MS," *Analytical Chemistry*, vol. 82, pp. 9932-9937, 2010.
- [76] Y. V. Deshmukh, *Industrial heating: principles, techniques, materials, applications, and design*, New York: CRC Press, 2005.
- [77] B. Koo and C.-J. Kim, "Evaluation of repeated electrowetting on three different fluoropolymer top coatings," *Journal of Micromechanics and Microengineering*, vol. 23, p. 067002, 2013.
- [78] M. S. Berridge, S. M. Apana and J. M. Hersh, "Teflon radiolysis as a major source of carrier in fluorine-18," *Journal of Labelled Compounds and Radiopharmaceuticals*, vol. 52, pp. 543-548, 2009.

- [79] O. Jacobson and X. Chen, "PET designated fluoride-18 production and chemistry," *Current Topics in Medicinal Chemistry*, vol. 10, pp. 1048-1059, 2010.
- [80] J. S. Fowler and T. Ido, "Initial and subsequent approach for the synthesis of  $^{18}\text{F}$ FDG," *Seminars in Nuclear Medicine*, vol. 32, pp. 6-12, 2002.
- [81] M. Reivich, D. Kuhl, A. Wolf, J. Greenberg, M. Phelps, T. Ido, V. Casella, J. Fowler, E. Hoffman, A. Alavi, P. Som and L. Sokoloff, "The [ $^{18}\text{F}$ ]fluorodeoxyglucose method for the measurement of local cerebral glucose utilization in man," *Circulation Research*, vol. 44, pp. 127-137, 1979.
- [82] B. Beuthien-Baumann, K. Hamacher, F. Oberdorfer and J. Steinbach, "Preparation of fluorine-18 labelled sugars and derivatives and their application as tracer for positron-emission-tomography," *Carbohydrate Research*, vol. 327, pp. 107-118, 2000.
- [83] J. S. Fowler, N. D. Volkow, G.-J. Wang and Y.-S. Ding, "2-deoxy-2- $^{18}\text{F}$ fluoro-d-glucose and alternative radiotracers for positron emission tomography imaging using the human brain as a model," *Seminars in Nuclear Medicine*, vol. 34, pp. 112-121, 2004.
- [84] G. J. Cook, E. A. Wegner and I. Fogelman, "Pitfalls and artifacts in  $^{18}\text{F}$ FDG PET and PET/CT oncologic imaging," *Seminars in Nuclear Medicine*, vol. 34, pp. 122-133, 2004.
- [85] A. F. Shields, J. R. Grierson, B. M. Dohmen, H.-J. Machulla, J. C. Stayanoff, J. M. Lawhorn-Crews, J. E. Obradovich, O. Muzik and T. J. Mangner, "Imaging proliferation in vivo with [ $^{18}\text{F}$ ]FLT and positron emission tomography," *Nature Medicine*, vol. 4, pp. 1334-1336, 1998.
- [86] O. S. Tehrani and A. F. Shields, "PET Imaging of proliferation with pyrimidines," *Journal of Nuclear Medicine*, vol. 54, pp. 903-912, 2013.
- [87] T. Barwick, B. Bencherif, J. M. Mountz and N. Avril, "Molecular PET and PET/CT imaging of tumour cell proliferation using F-18 fluoro-L-thymidine: a comprehensive evaluation," *Nuclear Medicine Communications*, vol. 30, pp. 908-917, 2009.
- [88] M. Kuchar, M. Pretze, T. Kniess, J. Steinbach, J. Pietzsch and R. Löser, "Site-selective radiolabeling of peptides by  $^{18}\text{F}$ -fluorobenzoylation with [ $^{18}\text{F}$ ]SFB in solution and on solid phase: a comparative study," *Amino Acids*, vol. 43, pp. 1431-1443, 2012.
- [89] A. P. Kostikov, J. Chin, K. Orchowski, E. Schirmacher, S. Niedermoser, K. Jurkschat, L. Iovkova-Berends, C. Wängler, B. Wängler and R. Schirmacher, "Synthesis of [ $^{18}\text{F}$ ]SiFB: a prosthetic group for direct protein radiolabeling for application in positron emission tomography," *Nature Protocols*, vol. 7, pp. 1956-1963, 2012.

- [90] G. Vaidyanathan and M. R. Zalutsky, "Synthesis of N-succinimidyl 4-[<sup>18</sup>F]fluorobenzoate, an agent for labeling proteins and peptides with 18F," *Nature Protocols*, vol. 1, pp. 1655-1661, 2006.
- [91] G. Tang, W. Zeng, M. Yu and G. Kabalka, "Facile synthesis of N-succinimidyl 4-[<sup>18</sup>F]fluorobenzoate ([<sup>18</sup>F]SFB) for protein labeling," *Journal of Labelled Compounds and Radiopharmaceuticals*, vol. 51, pp. 68-71, 2008.
- [92] W. Li, L. Lang, G. Niu, N. Guo, Y. Ma, D. O. Kiesewetter, B. Shen and X. Chen, "N-Succinimidyl 4-[<sup>18</sup>F]-fluoromethylbenzoate-labeled dimeric RGD peptide for imaging tumor integrin expression," *Amino Acids*, vol. 43, pp. 1349-1357, 2012.
- [93] K. Liu, E. J. Lepin, M.-W. Wang, F. Guo, W.-Y. Lin, Y.-C. Chen, S. J. Sirk, S. Olma, M. E. Phelps, X.-Z. Zhao, H.-R. Tseng, R. M. van Dam, A. M. Wu and C. K.-F. Shen, "Microfluidic-based 18F-labeling of Biomolecules for ImmunoPET," *Molecular Imaging*, vol. 10, pp. 168-177, 2011.
- [94] J. Mukherjee, Z.-Y. Yang, T. Brown, R. Lew, M. Wernick, X. Ouyang, N. Yasillo, C.-T. Chen, R. Mintzer and M. Cooper, "Preliminary assessment of extrastriatal dopamine d-2 receptor binding in the rodent and nonhuman primate brains using the high affinity radioligand, 18F fallypride," *Nuclear Medicine and Biology*, vol. 26, pp. 519-527, 1999.
- [95] J. Mukherjee, B. T. Christian, K. A. Dunigan, B. Shi, T. K. Narayanan, M. Satter and J. Mantil, "Brain imaging of <sup>18</sup>F-fallypride in normal volunteers: blood analysis, distribution, test-retest studies, and preliminary assessment of sensitivity to aging effects on dopamine D-2/D-3 receptors," *Synapse*, vol. 46, pp. 170-188, 2002.
- [96] J. T. Dunn, C. Clark-Papasavas, P. Marsden, S. Baker, M. Cleij, S. Kapur, R. Kessler, R. Howard and S. J. Reeves, "Establishing test-retest reliability of an adapted [<sup>18</sup>F]fallypride imaging protocol in older people," *Journal of Cerebral Blood Flow & Metabolism*, vol. 33, pp. 1098-1103, 2013.
- [97] M.-P. Kung and H. F. Kung, "Mass effect of injected dose in small rodent imaging by SPECT and PET," *Nuclear Medicine and Biology*, vol. 32, pp. 673-678, 2005.
- [98] A. A. Dooraghi, P. Y. Keng, S. Chen, M. R. Javed, C.-J. Kim, A. F. Chatziioannou and R. M. van Dam, "Optimization of microfluidic PET tracer synthesis with Cerenkov imaging," *Analyst*, vol. 138, pp. 5654-5664, 2013.

- [99] S. Chen, P. Keng, G. J. Shah, R. M. v. Dam and C.-J. Kim, "Synthesis of  $^{18}\text{F}$ -labeled probes on EWOD platform for positron emission tomography (PET) preclinical imaging," in *Proceedings of IEEE International Conference on Micro Electro Mechanical Systems*, Cancun, Mexico, 2011.
- [100] N. A. Gomzina, V. V. Zaitsev and R. N. Krasikova, "Optimization of nucleophilic fluorination step in the synthesis of various compounds labelled with fluorine-18 for their use as PET radiotracers," *Journal of Labelled Compounds and Radiopharmaceuticals*, vol. 44, pp. S895-S897, 2001.
- [101] H. K. Kim, S. Chen, J. L. R. Javed, C.-J. Kim, P. Y. Keng and R. M. van Dam, "Multi-step organic synthesis of four different molecular probes in digital microfluidic devices," in *Proceedings of the International Conference on Miniaturized Systems for Chemistry and Life Sciences*, Okinawa, Japan, pp. 617-619, 2012.
- [102] A. J. Parker, "Protic-dipolar aprotic solvent effects on rates of bimolecular reactions," *Chemical Reviews*, vol. 69, pp. 1-32, 1969.
- [103] G. J. Shah, H. Ding, S. Sadeghi, S. Chen, C.-J. Kim and R. M. van Dam, "On-demand droplet loading for automated organic chemistry on digital microfluidics," *Lab on a Chip*, vol. 13, pp. 2785-2795, 2013.
- [104] P. J. Scott and M. R. Kilbourn, "Determination of residual Kryptofix 2.2.2 levels in [ $^{18}\text{F}$ ]-labeled radiopharmaceuticals for human use," *Applied Radiation and Isotopes*, vol. 65, pp. 1359-1362, 2007.
- [105] G. B. Saha, *Fundamentals of Nuclear Pharmacy*, New York: Springer, 2010.
- [106] S. Chen, J. Lei, R. M. van Dam, P. Y. Keng and C.-J. Kim, "Planar alumina purification of  $^{18}\text{F}$ -labeled radiotracer synthesis on EWOD chip for positron emission tomography (PET)," in *Proceedings of the International Conference on Miniaturized Systems for Chemistry and Life Sciences*, Okinawa, Japan, pp. 1771-1773, 2012.
- [107] S. Chen, D. Alex A, M. Lazari, R. M. van Dam, A. F. Chatziioannou and a. C.-J. Kim, "On-chip product purification for complete microfluidic radiotracer synthesis," in *Proceedings of the International Conference of MEMS*, San Francisco, California, pp. 284-287, 2014.
- [108] S. K. Chitneni, K. Serdons, N. Evens, H. Fonge, S. Celen, C. M. Deroose, Z. Debyser, L. Mortelmans, A. M. Verbruggen and G. M. Bormans, "Efficient purification and metabolite analysis of radiotracers using high-performance liquid chromatography and on-line solid-phase extraction," *Journal of Chromatography A*, vol. 1189, pp. 323-331, 2008.

- [109] Y. Kazakevich and R. LoBrutto, *HPLC for Pharmaceutical Scientists*, New Jersey: John Wiley & Sons, Inc., 2007.
- [110] C. Pascali, A. Bogni, L. Fugazza, C. Cucchi, O. Crispu, L. Laera, R. Iwata, G. Maiocchi, F. Crippa and E. Bombardieri, "Simple preparation and purification of ethanol-free solutions of 3'-deoxy-3'-[<sup>18</sup>F]fluorothymidine by means of disposable solid-phase extraction cartridges," *Nuclear Medicine and Biology*, vol. 39, pp. 540-550, 2012.
- [111] V. D. Gialleonardo, A. Signore, A. W. Glaudemans, R. A. Dierckx and E. F. D. Vries, "N-(4-<sup>18</sup>F-fluorobenzoyl)interleukin-2 for PET of human-activated T lymphocytes," *Journal of Nuclear Medicine*, vol. 53, pp. 679-686, 2012.
- [112] J. Schmaljohann, E. Schirmmacher, B. Wängler, C. Wängler, R. Schirmmacher and S. Guhlke, "Fully automated SPE-based synthesis and purification of 2-[<sup>18</sup>F]fluoroethylcholine for human use," *Nuclear Medicine and Biology*, vol. 38, pp. 165-170, 2011.
- [113] T. Chaly, R. Mattacchieri, J. W. Velez, J. R. Dahl and D. Margouleff, "A large scale manual production of [<sup>18</sup>F]FDG using a synthetic unit made of sterile disposable components and operated by a Master Slave Manipulator," *International Journal of Radiation Applications and Instrumentation. Part A. Applied Radiation and Isotopes*, vol. 41, pp. 29-34, 1990.
- [114] F. D. Leonardis, G. Pascali, P. A. Salvadori, P. Watts and N. Pamme, "On-chip pre-concentration and complexation of [<sup>18</sup>F]fluoride ions via regenerable anion exchange particles for radiochemical synthesis of positron emission tomography tracers," *Journal of Chromatography A*, vol. 1218, pp. 4714-4719, 2011.
- [115] M. D. Tarn, G. Pascali, F. D. Leonardis, P. Watts, P. A. Salvadori and N. Pamme, "Purification of 2-[<sup>18</sup>F]fluoro-2-deoxy-D-glucose by on chip solid-phase extraction," *Journal of Chromatography A*, vol. 1280, pp. 117-121, 2013.
- [116] G. J. Shah, J. L. Veale, Y. Korin, E. F. Reed, H. A. Gritsch and C.-J. Kim, "Specific binding and magnetic concentration of CD8+ T-lymphocytes on electrowetting-on-dielectric platform," *Biomicrofluidics*, vol. 4, p. 044106, 2010.
- [117] H. Yang, J. M. Mudrik, M. J. Jebrail and A. R. Wheeler, "A digital microfluidic method for in situ formation of porous polymer monoliths with application to solid-phase extraction," *Analytical Chemistry*, vol. 83, pp. 3824-3830, 2011.
- [118] S. K. Cho, Y. Zhao and C.-J. Kim, "Concentration and binary separation of micro particles for droplet-based digital microfluidics," *Lab on a Chip*, vol. 7, pp. 490-498, 2007.

- [119] M. J. Schertzer, R. Ben-Mrad and P. E. Sullivan, "Mechanical filtration of particles in electrowetting on dielectric devices," *Journal of Microelectromechanical Systems*, vol. 20, pp. 1010-1015, 2011.
- [120] M. Mibus, C. Jensen, X. Hu, C. Knospe, M. L. Reed and G. Zangari, "Dielectric breakdown and failure of anodic aluminum oxide films for electrowetting systems," *Journal of Applied Physics*, vol. 114, p. 014901, 2013.
- [121] J.-K. Chang, C.-M. Lin, C.-M. Liao, C.-H. Chen and W.-T. Tsai, "Effect of heat-treatment on characteristics of anodized aluminum oxide formed in ammonium adipate solution," *Journal of the Electrochemical Society*, vol. 151, pp. B188-B194, 2004.
- [122] G. Sposito, *The Environmental Chemistry of Aluminum*, Boca Raton, Florida: CRC Press, 1996.
- [123] N. J. Simpson, *Solid-Phase Extraction: Principles, Techniques, and Applications*, New York: Marcel Dekker, Inc., 2000.
- [124] V. B. Carballo, J. Melai, C. Salm and J. Schmitz, "Moisture resistance of SU-8 and KMPR as structural material," *Microelectronic Engineering*, vol. 86, pp. 765-768, 2009.
- [125] H. Liu, S. Dharmatilleke, D. K. Maurya and A. A. Tay, "Dielectric materials for electrowetting-on-dielectric actuation," *Microsystem Technologies*, vol. 16, pp. 449-460, 2010.
- [126] Y. Li, W. Parkes, L. I. Haworth and A. Ross, "Room-temperature fabrication of anodic tantalum pentoxide for low-voltage electrowetting on dielectric (EWOD)," *Journal of Microelectromechanical Systems*, vol. 16, pp. 1481-1488, 2008.
- [127] M. Dhindsa, J. Heikenfeld, W. Weekamp and S. Kuiper, "Electrowetting without electrolysis on self-healing dielectrics," *Langmuir*, vol. 27, pp. 5665-5670, 2011.
- [128] M. Lohrengel, "Thin anodic oxide layers on aluminum and other valve metals: high field regime," *Materials Science and Engineering: R: Reports*, vol. 11, pp. 243-294, 1993.
- [129] L.-X. Huang, B. Koo and C.-J. Kim, "Sputtered-anodized Ta<sub>2</sub>O<sub>5</sub> as the dielectric layer for electrowetting-on-dielectric," *Journal of Microelectromechanical Systems*, vol. 22, pp. 253-355, 2013.
- [130] S. Chen and C.-J. Kim, "Mirrored anodized dielectric for reliable electrowetting," in *Proceedings of the International Conference of MEMS*, San Francisco, California, pp. 1011-1014, 2014.

- [131] A. Nishino, "Capacitors: operating principles, current market and technical trends," *Journal of Power Sources*, vol. 60, pp. 137-147, 1996.
- [132] R. W. Berry and D. J. Sloan, "Tantalum printed capacitors," *Proceedings of the IRE*, vol. 47, pp. 1070-1075, 1959.
- [133] N. B. Crane, P. M. Alex A. Volinsky, A. Rajgadkar and M. Khodayari, "Bidirectional electrowetting actuation with voltage polarity dependence," *Applied Physics Letters*, vol. 96, p. 104103, 2010.
- [134] C. W. Nelson, C. M. Lynch and N. B. Crane, "Continuous electrowetting via electrochemical diodes," *Lab on a Chip*, vol. 11, pp. 2149-2152, 2011.
- [135] J. D. Sloppy, D. D. Macdonald and E. C. Dickey, "Growth laws of bilayer anodized tantalum oxide films formed in phosphoric acid," *Journal of the Electrochemical Society*, vol. 157, pp. C157-C165, 2010.
- [136] L. Young, "Anodization constants for tantalum," *Journal of the Electrochemical Society*, vol. 124, pp. 528-529, 1977.
- [137] U.-C. Yi and C.-J. Kim, "Characterization of electrowetting actuation on addressable single-side coplanar electrodes," *Journal of Micromechanics and Microengineering*, vol. 16, pp. 2053-2059, 2006.
- [138] B. Raj, M. Dhindsa, N. Smith, R. Laughlin and J. Heikenfeld, "Ion and liquid dependent dielectric failure in electrowetting systems," *Langmuir*, vol. 25, pp. 12387-12392, 2009.
- [139] A. V. Fraioli, "Recent advances in the solid-state electrolytic capacitor," *IRE Transactions on Component Parts*, vol. 5, pp. 72-75, 1958.